Observation of $W \to \tau\nu_\tau$ Decays with the ATLAS Experiment

Inaugural-Dissertation
zur
Erlangung der Doktorwürde
der
Mathematisch-Naturwissenschaftlichen Fakultät
der
Rheinischen Friedrich-Wilhelms-Universität
zu Bonn

vorgelegt von
Guilherme Nunes Hanninger
aus
Curitiba - Brasilien

Bonn 2011

Universität Bonn
Physikalisches Institut

Observation of $W \to \tau\nu_\tau$ Decays with the ATLAS Experiment

Guilherme Nunes Hanninger

Dieser Forschungsbericht wurde als Dissertation von der Mathematisch-Naturwissenschaftlichen-Fakultät der Universität Bonn angenommen und ist auf der ULB Bonn `http://hss.ulb.uni-bonn.de/diss_online` elektronisch publiziert.

Referent:	Prof. Dr. Norbert Wermes
Koreferent:	Prof. Dr. Ian C. Brock
Angenommen am:	22.02.2011
Tag der Promotion:	29.04.2011

Abstract

Physics studies of processes with τ leptons in the final state, while challenging at hadron colliders, are of great importance at the LHC. The τ leptons provide important signatures in searches for the Higgs boson as well as for new physics in a wide range of theoretical models. Decays of Standard Model particles to τ leptons, in particular $Z \to \tau\tau$ and $W \to \tau\nu_\tau$, are important background processes in those searches and their cross sections need to be measured first. This thesis reports the first observation of $W \to \tau\nu_\tau$ decays and of hadronically decaying τ leptons with the ATLAS experiment at the LHC. The analysis is based on a data sample corresponding to an integrated luminosity of 546 nb^{-1}, which was recorded at a proton-proton centre-of-mass energy of 7 TeV. A total of 78 data events are selected, with an estimated background of $11.1 \pm 2.3_{\text{(stat.)}} \pm 3.2_{\text{(syst.)}}$ events from QCD processes, and of $11.8 \pm 0.4_{\text{(stat.)}} \pm 3.7_{\text{(syst.)}}$ events from other W and Z decays. The observed excess of data events over the total background is compatible with the SM expectation for $W \to \tau\nu_\tau$ decays, both in the number of events and in the shapes of distributions of characteristic variables.

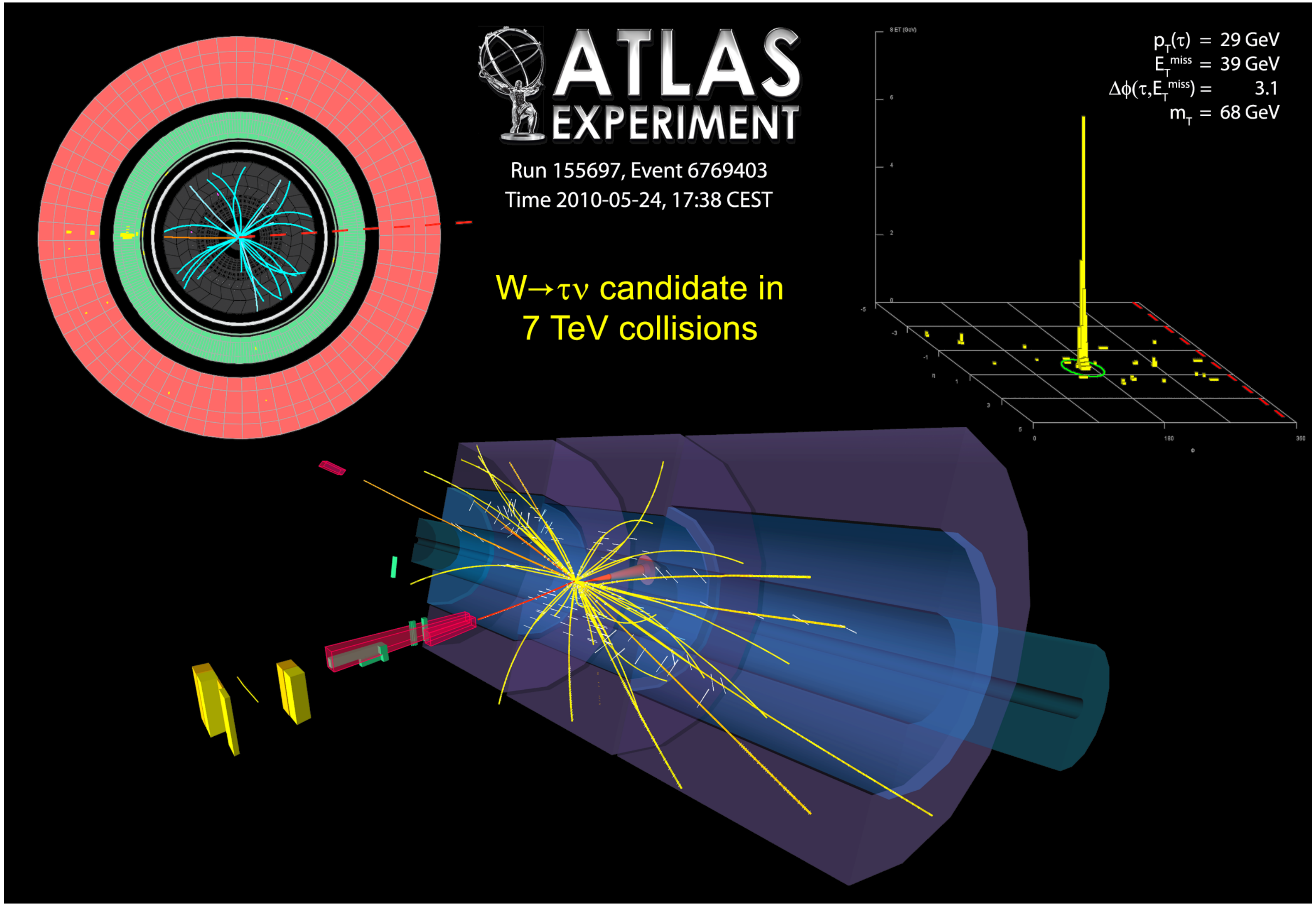

Display of the first $W \to \tau_h \nu_\tau$ event candidate observed in ATLAS (event collected on May 24th 2010). The hadronically decaying single-prong τ candidate is clearly visible. It has one well-identified track (red-orange) with a transverse momentum of 10 GeV and energy deposited in the electromagnetic and hadronic calorimeters (20 GeV and 10 GeV, respectively). The energy depositions in the cells of hadronic tile and electromagnetic calorimeter form a narrow shower typical of a hadronic τ decay. It is the only high-momentum object in the event, no other jets, muons, electrons or photons were found. E_T^{miss} is indicated by a red arrow or dashed line.

Contents

1. Introduction

The development of new accelerators and detectors in the last decades has contributed to great advances in particle physics. Moreover, several new ideas were proposed and developed in quantum field theories for describing strong, weak and electromagnetic interactions. In the late 1960's these ideas were concentrated into a simple and elegant theory known as the Standard Model (SM) which has been very successful at describing the fundamental particles that make up all matter and their interactions. It has, for example, correctly predicted the existence of the W and Z bosons, the gluon, the charm quark and the top quark before their discovery. The Higgs boson is the only particle predicted by the SM which has not yet been detected.

Despite being a very successful theory of particle physics to date, the SM is also believed to be incomplete and therefore not the ultimate theory. Gravity, for example, is not incorporated into the SM. In addition, this theory does not explain the presence of dark matter throughout the universe and has unsolved problems such as the large hierarchy in energy scales. Several new theories have been proposed to address these open issues. For instance, supersymmetry (SUSY) is an attractive way to go beyond the SM.

The ATLAS experiment at the Large Hadron Collider (LHC), the largest and most powerful particle accelerator ever built, hopes to probe these and many other open scientific questions at the frontier of particle physics.

The τ lepton plays a very important role in the ATLAS physics program since it provides a useful signature in searches for the SM Higgs boson and new phenomena, in a wide range of theoretical models, with τ leptons in the final state. For example, the SM $H \to \tau\tau$ decay mode has the cleanest signature in the low mass region ($115 < m_H < 140\,\mathrm{GeV}$) and, in SUSY models, the observation of the charged Higgs decaying into a τ lepton and a neutrino would be a clear sign of new physics beyond the SM [1–4]. The τ lepton is very similar to electrons or muons but it is the only lepton heavy enough to decay into hadrons as well as into leptons. The τ properties, such as mass, lifetime, decay modes and polarization, have been precisely measured in several experiments using e^+e^- collisions, namely the experiments at LEP [5, 6], Babar [7], Belle [8], BESII [9], CLEO [10] and KEDR [11].

Decays of SM particles to τ leptons, in particular $Z \to \tau\tau$ and $W \to \tau\nu_\tau$, are important background processes in those searches and their cross sections need to be measured first. Theoretical calculations of the W and Z boson production cross sections have been carried out in next-to-next-leading order (NNLO). The main contribution to the calculated cross section is from $q\bar{q}$ interactions followed by $q(\bar{q})g$ interactions. At NNLO, the $W \to \tau\nu_\tau$ signal is predicted to be produced at a proton-proton center-of-mass energy of 7 TeV with a cross section times branching ratio of [12, 13]:

$$\sigma_W \times BR(W \to \tau\nu_\tau) = 10.46\,\text{nb}, \tag{1.1}$$

which is about ten times higher than for $Z \to \tau\tau$ events. This prediction is in good agreement with the ATLAS measurement for $W \to \ell\nu$ ($\ell = e$ or μ) of [14]:

$$\sigma_W^{tot} \cdot BR(W \to \ell\nu) = 9.96 \pm 0.23_{(\text{stat.})} \pm 0.50_{(\text{syst.})} \pm 1.10_{(\text{lumi})}\text{nb}. \tag{1.2}$$

The measured ratio of the W to Z cross sections times branching ratios in ATLAS is [14]:

$$\frac{\sigma_W \cdot BR(W \to \ell\nu)}{\sigma_Z \cdot BR(Z \to \ell\ell)} = 11.7 \pm 0.9_{(\text{stat.})} \pm 0.4_{(\text{syst.})}. \tag{1.3}$$

Amid a strong physics motivation for exploring data with τ leptons in the final state, τ reconstruction and identification at hadron colliders are challenging from the experimental point of view. Since purely leptonic τ decays (referred to as τ_ℓ in this thesis) cannot be easily distinguished from electrons or muons from $W \to e\nu_e$ or $W \to \mu\nu_\mu$ decays, the τ identification algorithms are developed to select only hadronically decaying τ leptons (referred to as τ_h in this thesis). The hadronic τ decay modes have the largest decay branching fraction of about 65% but their signatures in the detector are very similar to jets from QCD processes. Therefore, an efficient and reliable identification of hadronically decaying τs is critical for the rejection of the huge QCD jet background. Moreover, the τ's energy cannot be measured directly as the neutrino in the hadronic τ decay carries off energy and gives rise to missing transverse energy ($E_\mathrm{T}^\mathrm{miss}$). It is thus crucial to have a good $E_\mathrm{T}^\mathrm{miss}$ resolution in the detector for channels requiring reconstruction of the invariant mass of the object decaying to τ leptons. Another related challenge is providing efficient triggering for events with τ_h while keeping trigger rates at levels sustainable by the trigger system.

In this thesis, the first observation of hadronically decaying τ leptons from $W \to \tau\nu_\tau$ decays with the ATLAS experiment at the LHC is reported. This observation, documented in [15], constitutes the first step in the ATLAS physics program with τ leptons in the final state. It is based on data that were recorded at a proton-proton center-of-mass energy of 7 TeV from March to mid-August and correspond to an integrated luminosity of 546 nb^{-1}.

This thesis is organized as follows. In Chapter 2, the Standard Model is briefly introduced and the elementary particles and their interactions are described. Also the Higgs mechanism and supersymmetry are shortly discussed. This is followed by the description of the ATLAS detector in Chapter 3. Chapter 4 presents the Monte Carlo event generators, detector simulation and the algorithms used for event reconstruction. The algorithms used for τ_{h} reconstruction and identification are presented in detail in Chapter 5. In Chapter 6, the W-boson production at the LHC, the kinematic properties of the $W \rightarrow \tau_{\mathrm{h}}\nu_{\tau}$ decays and the main background processes are discussed. The selection of $W \rightarrow \tau_{\mathrm{h}}\nu_{\tau}$ events is described in Chapter 7. The method used to estimate the QCD background contribution directly from data and several tests to validate it are detailed in Chapter 8. The systematic uncertainties are presented in Chapter 9 and Chapter 10 summarizes the results and gives an outlook on future directions. Finally, the conclusion of this work is presented in Chapter 11.

2. The Standard Model and Beyond

The Standard Model of particle physics is a theory that describes in detail three out of the four known fundamental interactions as well as the elementary particles that take part in these interactions and make up all visible matter in the universe. Despite the success of this theory, the SM is also believed to be incomplete and therefore not the ultimate theory. There are a number of experimental observations of Nature for which the SM does not give an adequate explanation, for example: dark matter and gravity. Supersymmetry is one of the most attractive ways to go beyond the SM and provide a solution to these problems.

This chapter briefly describes the elementary particles in the Standard Model and the characteristic properties of their interactions. The Higgs mechanism is also presented followed by a short introduction to supersymmetry. In addition, example of searches for the SM Higgs boson and supersymmetric particles at the LHC are discussed, with emphasis on the searches with τ leptons in the final state. The τ lepton properties will be described together with the τ identification algorithms in Chapter 5. The production of the $W \to \tau\nu_\tau$ process at the LHC, its kinematic properties and background processes will be presented in detail in a separate chapter, in Chapter 6. Discussions in this chapter is, in many respects, based upon the textbook on the physics of the SM and beyond by Morii, Lim and Mukherjee [16].

2.1 The Standard Model

The Standard Model contains both the fermionic and the bosonic fundamental particles. Fermions are particles with half-integer spin and obey the Pauli exclusion principle. On the other hand, bosons possess integer spin and do not obey the Pauli exclusion principle.

The fundamental fermions of spin $s = 1/2$ form the basic constituents of matter and can be divided into two types, leptons and quarks. Six different leptons are known (and six antileptons with opposite quantum numbers): the electron, e, the muon, μ, and the tau, τ, with electric charge[1] $Q = -1$, and the corresponding neutrinos ν_e, ν_μ and ν_τ with electric charge $Q = 0$. The neutrinos interact via the weak force only, while the e, μ and τ interact via both the weak and the electromagnetic forces.

[1] All electric charges are given in units of the elementary charge e.

Similarly, there are six *flavors* of quarks (and six antiquarks), u, d, c, s, t and b with fractional charge $Q = 2/3$, $-1/3$, $2/3$, $-1/3$, $2/3$ and $-1/3$, respectively. In addition to flavor, quarks have another degree of freedom called *color* that can be out of three types, *red*, *green* and *blue*. Quarks form hadrons, which are classified into baryons and mesons. Baryons are fermions made of three quarks, for instance the proton p (uud) and the neutron n (ddu). Mesons are bosons made of one quark and one antiquark, for example the pions ($\pi^+ \sim u\bar{d}$ and $\pi^- \sim d\bar{u}$). Since there exist no colored hadrons in Nature, it is assumed that all observed hadrons must be colorless, i.e. color singlet states.

The interactions among the fundamental particles are mediated by the exchange of bosons with spin $s = 1$. The electromagnetic, weak and strong interactions are mediated by photons γ, weak bosons $W^\pm$, Z^0 and eight gluons g_α, $\alpha = 1, \ldots 8$, respectively.

The Standard Model of electroweak and strong interactions is based on the gauge group

$$G = SU(3)_C \times SU(2)_L \times U(1)_Y. \tag{2.1}$$

The subscript L means that the fields participating in the interaction are left-handed and Y denotes the weak hypercharge. The left-handed and right-handed fields as well as the weak hypercharge are explained in the next section.

The $SU(3)_C$ represents the non-Abelian gauge symmetry group of the strong interaction where the gluonic gauge fields are coupled to the color charges as formalized in Quantum Chromodynamics (QCD). The $SU(2)_L \times U(1)_Y$ gauge symmetry represents the symmetry group of the electroweak interactions, which is also a non-Abelian gauge theory. The electromagnetic interaction $U(1)_{em}$ appears as a subgroup of $SU(2)_L \times U(1)_Y$ and is described by the Abelian gauge theory, Quantum Electrodynamics (QED). These Abelian and non-Abelian groups have an important feature that is gluons and weak bosons have self-couplings while the photon does not couple to itself. Photons are massless and hence their interaction ranges are infinite. Gluons are also massless, but their interaction ranges are finite because of the non-Abelian nature of color interaction. Another consequence of the non-Abelian nature is that the strong force between quarks increases with distance and quarks are thus confined inside hadrons. The weak bosons $W^\pm$ and Z^0 are massive (see Table 2.1) and therefore the weak interaction range is very short ($\sim 10^{-18}$ m).

Since the weak gauge bosons are massive particles, $SU(2)_L \times U(1)_Y$ is not a symmetry of the vacuum[2]. In contrast, the photon being massless reflects that $U(1)_{em}$ is a good symmetry of the vacuum. Therefore, the gauge group G is broken spontaneously to $SU(3)_C \times U(1)_{em}$ by means of the Higgs Mechanism.

[2] In quantum field theories, particle excitations of a field are defined as quantized fluctuations of the field about its lowest energy state, i.e. the vacuum state [16].

In the electroweak sector of the SM, the Higgs mechanism postulates that scalar fields interact with each other in such a way that the ground state acquires a non-zero field strength, breaking the electroweak symmetry of local gauge symmetries spontaneously [17]. The interaction energies of electroweak gauge bosons, leptons and quarks with this field manifest themselves as non-zero masses of these particles. This sector also predicts the existence of a single neutral Higgs boson with spin-0 which has not yet been observed. Understanding this mechanism that breaks electroweak symmetry and generates the masses of all known elementary particles is one of the most fundamental problems in particle physics.

2.2 The Standard Model of electroweak interactions

The symmetry group $SU(2)_L \times U(1)_Y$ of the electroweak interaction is the basis of the Glashow-Salam-Weinberg theory. Leptons and quarks are realized in three families of identical structure. The members of each doublet participate in the charged current weak interaction processes together. The only difference between the families is the difference of the masses of the quarks and leptons, depending on the family. The first family (e, ν_e, u, d and their anti-particles) is responsible for most of the macroscopic phenomena we observe. Moreover, the fermions are organized in left-handed isospin doublets and right-handed isospin singlets. The masses of the elementary fermions and bosons are listed in Table 2.1 and the quantum numbers of the elementary fermions are shown in Table 2.2.

Leptons		Quarks		Bosons	
e	511 eV	u	$1.7 - 3.3$ MeV		
ν_e	< 2 eV	d	$4.1 - 5.8$ MeV	γ	0
μ	105.7 MeV	c	$1.27^{+0.07}_{-0.09}$ GeV	$W^{\pm}$	80.399 ± 0.023 GeV
ν_μ	< 0.19 MeV	s	101^{+29}_{-21} MeV	Z	91.1876 ± 0.0021 GeV
τ	1777 MeV	b	$4.19^{+0.18}_{-0.06}$ GeV	g	0
ν_τ	< 18.2 MeV	t	$172.0 \pm 0.9 \pm 1.3$ GeV		

Table 2.1: Masses of the elementary fermions and bosons [18]. Only upper limits are given for the masses of the neutrinos, although there is strong experimental evidence that they are massive.

The left-handed and right-handed fields are defined by means of the chirality operator γ_5:

$$e_L^- = \frac{1}{2}(1 - \gamma_5)e^-; \qquad e_R^- = \frac{1}{2}(1 + \gamma_5)e^-, \tag{2.2}$$

where γ_5 is defined using I, the 4×4 unit matrix, as:

Families			Quantum Numbers				
1	2	3	T	T^3	Y	Q	C
	Leptons						
$\begin{pmatrix}\nu_e\\e^-\end{pmatrix}_L$	$\begin{pmatrix}\nu_\mu\\\mu^-\end{pmatrix}_L$	$\begin{pmatrix}\nu_\tau\\\tau^-\end{pmatrix}_L$	$\begin{pmatrix}1/2\\1/2\end{pmatrix}$	$\begin{pmatrix}1/2\\-1/2\end{pmatrix}$	$\begin{pmatrix}-1\\-1\end{pmatrix}$	$\begin{pmatrix}0\\-1\end{pmatrix}$	$\begin{pmatrix}0\\0\end{pmatrix}$
e_R	μ_R	τ_R	0	0	-2	-1	0
	Quarks						
$\begin{pmatrix}u\\d\end{pmatrix}_L$	$\begin{pmatrix}c\\s\end{pmatrix}_L$	$\begin{pmatrix}t\\b\end{pmatrix}_L$	$\begin{pmatrix}1/2\\1/2\end{pmatrix}$	$\begin{pmatrix}1/2\\-1/2\end{pmatrix}$	$\begin{pmatrix}1/3\\1/3\end{pmatrix}$	$\begin{pmatrix}2/3\\-1/3\end{pmatrix}$	$\begin{pmatrix}r,g,b\\r,g,b\end{pmatrix}$
u_R	c_R	t_R	0	0	$4/3$	$2/3$	r,g,b
d_R	s_R	b_R	0	0	$-2/3$	$-1/3$	r,g,b

Table 2.2: Elementary fermions and their quantum numbers. T: Weak isospin; T^3: 3^{rd} component of weak isospin; Y: Hypercharge; Q: electric charge and C: color charge. These quantum numbers change their sign for anti-fermions.

$$\gamma_5 = \begin{pmatrix} 0 & I \\ I & 0 \end{pmatrix}.$$

The different isospin assignment to left-handed and right-handed fields allows for maximal parity violation in the weak interaction [17]. The weak isospin group $SU(2)_L$ has three generators: $T_i = \frac{\sigma_i}{2}$, with $i = 1,2,3$ and σ_i the Pauli matrices[3]. T^i corresponds to the conserved weak charges defined according to the Noether's Theorem by:

$$T^i = \int J^i d^3x. \tag{2.3}$$

where J^i is the weak charged current. $U(1)_Y$ has one generator, $\frac{Y}{2}$, where the weak hypercharge Y is connected with the electric charge Q and the weak isospin by the relation:

$$Y = 2(Q - T^3). \tag{2.4}$$

Defining the left-handed doublet as L and the right-handed singlet as R, the gauge invariant Lagrangian with $SU(2)_L \times U(1)_Y$ symmetry is constructed as

$$\mathscr{L}_F = \overline{L} i\gamma^\mu (\partial_\mu - ig\frac{\overrightarrow{\sigma}}{2} \cdot \overrightarrow{A}_\mu + \frac{i}{2} g' B_\mu) L + \overline{R} i\gamma^\mu (\partial_\mu + ig' B_\mu) R, \tag{2.5}$$

where $A^i_\mu (i = 1,2,3)$ and B_μ are gauge boson fields associated with $SU(2)_L$ and $U(1)_Y$, re-

[3]
$$\sigma_1 = \begin{pmatrix} 0 & 1 \\ 1 & 0 \end{pmatrix} \qquad \sigma_2 = \begin{pmatrix} 0 & -i \\ i & 0 \end{pmatrix} \qquad \sigma_3 = \begin{pmatrix} 1 & 0 \\ 0 & -1 \end{pmatrix}.$$

spectively, and g and g' are the corresponding gauge coupling constants.

The kinetic term of the gauge fields which should be added to $\mathscr{L}_F$ is given by

$$\mathscr{L}_G = -\frac{1}{4}F^i_{\mu\nu}F^{i\mu\nu} - \frac{1}{4}B_{\mu\nu}B^{\mu\nu} \tag{2.6}$$

with

$$F^i_{\mu\nu} = \partial_\mu A^i_\nu - \partial_\nu A^i_\mu + g\varepsilon_{ijk}A^j_\mu A^k_\nu, \tag{2.7}$$

$$B_{\mu\nu} = \partial_\mu B_\nu - \partial_\nu B_\mu, \tag{2.8}$$

where $F^i_{\mu\nu}(i = 1,2,3)$ and $B_{\mu\nu}$ are field-strength tensors of gauge fields corresponding to $SU(2)_L$ and $U(1)_Y$, respectively; ε^{ijk} is the totally antisymmetric Levi-Cività tensor with $\varepsilon^{123} = 1$. The mass term of the fermions and bosons appears neither in $\mathscr{L}_F$ nor in $\mathscr{L}_G$. They are all massless at this stage and they will become massive when the Higgs mechanism is introduced, as described in the following section.

2.2.1 Spontaneous breaking of $\mathbf{SU(2)_L \times U(1)_Y}$ symmetry

Spontaneous symmetry breaking corresponds to the breaking of the symmetry of the original Lagrangian by breaking the symmetry of the vacuum. If the Lagrangian has a global symmetry, the Goldstone Theorem [19, 20] implies that there must exist one massless boson (Goldstone boson), scalar or pseudoscalar, associated to each generator which does not annihilate the vacuum and has its same quantum numbers [21].

$SU(2)_L \times U(1)_Y$ has four gauge bosons and since the photon is massless, the symmetry must be broken according to:

$$SU(2)_L \times U(1)_Y \longrightarrow U(1)_{em}. \tag{2.9}$$

The electroweak symmetry breaking (EWSB) can be realized using the Higgs mechanism. Starting with an $SU(2)$ doublet of two complex scalar fields whose weak hypercharge is $Y_\phi = +1$,

$$\phi = \begin{pmatrix} \varphi^+ \\ \varphi^0 \end{pmatrix}, \tag{2.10}$$

where φ^+ and φ^0 are positively charged and neutral complex scalar fields, respectively, the Lagrangian is given by:

$$\mathscr{L}_C = (D_\mu\phi)^\dagger(D^\mu\phi) - V(\phi^\dagger\phi) \tag{2.11}$$

with

$$D_\mu\phi = (\partial_\mu - ig\frac{\overrightarrow{\sigma}}{2}\overrightarrow{A_\mu} - \frac{i}{2}g'B_\mu)\phi. \tag{2.12}$$

The potential term is gauge invariant and given by:

$$V(\phi^*\phi) = m\phi^*\phi + \lambda(\phi^*\phi)^2. \tag{2.13}$$

For $\lambda > 0$ and $m^2 = -\mu^2$ ($\mu^2 > 0$), the potential V is illustrated in Figure 2.1.

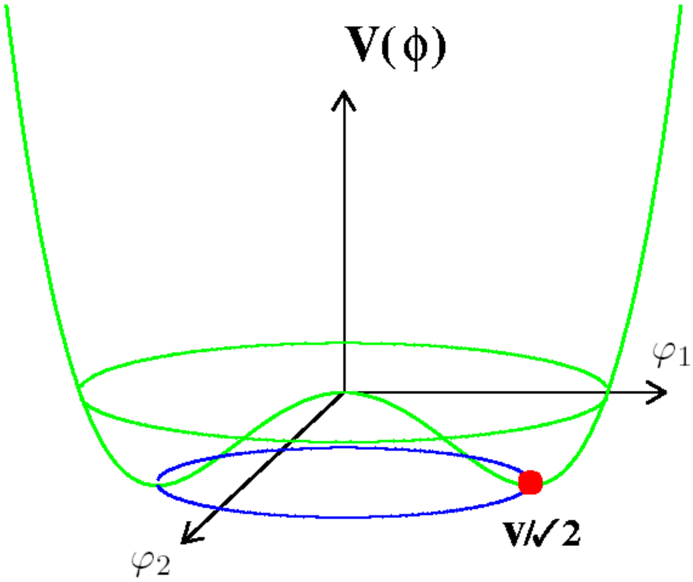

Figure 2.1: Illustration of the potential V for $\lambda > 0$ and $m^2 = -\mu^2$ ($\mu^2 > 0$).

The minimum of the potential V can be obtained by $(\frac{\partial V}{\partial \varphi^+})_0 = (\frac{\partial V}{\partial \varphi^0})_0 = 0$ and is given by $\phi^\dagger\phi = \mid \phi \mid^2 = \frac{v^2}{2}$, with $v = \sqrt{\frac{\mu^2}{\lambda}}$. Therefore, all points on the circle with radius v corresponds to the minimum of the potential V. Then, spontaneous symmetry breaking occurs when the scalar doublet ϕ develops a vacuum expectation value $\phi_0 = \begin{pmatrix} 0 \\ v/\sqrt{2} \end{pmatrix}$. As a remark, T^3 and Y have non-vanishing vacuum expectation values:

$$T^3\phi_0 = \frac{-1}{2}\phi_0; \qquad Y\phi_0 = \phi_0,$$

while the electric charge does:

$$Q\phi_0 = 0.$$

Therefore, Goldstone bosons must exist associated with T^3 and Y. Parameterizing now the scalar doublet with four degrees of freedom in terms of the fields denoting the shifts from the vacuum state ϕ_0,

$$\phi = \begin{pmatrix} \varphi^+ \\ \varphi^0 \end{pmatrix} = e^{i\vec{\sigma}\cdot\vec{\xi}/2v} \begin{pmatrix} 0 \\ (v+H)/\sqrt{2} \end{pmatrix} \tag{2.14}$$

where $\xi_i (i = 1,2,3)$ and H are real fields. Using the Higgs mechanism, the three massless Goldstone bosons ξ_i are generated, which are absorbed to give masses to the gauge bosons $W^\pm$ and Z^0. The remaining component of the complex doublet becomes the Higgs boson, a new fundamental scalar particle. The $W^\pm$ boson is defined by:

$$W^\pm_\mu = \frac{A'^1_\mu \mp i A'^2_\mu}{\sqrt{2}} \tag{2.15}$$

with mass $m_W = \frac{1}{2} g v$. The Z boson can be obtained from:

$$\begin{pmatrix} Z_\mu \\ A_\mu \end{pmatrix} = \begin{pmatrix} \cos\theta_W & -\sin\theta_W \\ \sin\theta_W & \cos\theta_W \end{pmatrix} \begin{pmatrix} A'^3_\mu \\ B'_\mu \end{pmatrix} \tag{2.16}$$

where θ_W is the weak mixing angle or Weinberg angle, with $\tan\theta_W = \frac{g'}{g}$ and $\sin^2\theta_W = 0.23116(13)$ [18] and A_μ is associated to the photon field with mass $m_\gamma = 0$. The fact that the experimental value of $\sin^2\theta_W$ is far away from 0 and 1 indicates a large mixing effect. It supports thus the interpretation that the electromagnetic and the weak interactions are indeed manifestations of a unified electroweak interaction. The neutral Z boson becomes massive with:

$$m_Z = \frac{1}{2} v \sqrt{g^2 + g'^2} = \frac{m_W}{\cos\theta_W}. \tag{2.17}$$

The Higgs-boson mass is given by:

$$m_H = \sqrt{2\mu^2} \tag{2.18}$$

and cannot be predicted since μ is an unknown parameter. To obtain the fermion mass, one has to consider the interaction between fermion fields and the Higgs field of Yukawa type $\mathscr{L}_Y = G_f f \bar{f} \phi$. Replacing the Higgs field by its ground state, $\phi \to v/\sqrt{2}$, the fermion mass can be obtained as $m_f = G_f v/\sqrt{2}$ [21]. $v = (\sqrt{2} G_F)^{-1/2} \simeq 246\,\text{GeV}$ is fixed by the Fermi coupling constant G_F, which is determined precisely from μ-decay measurements [18], and sets the scale of EWSB.

Finally, the Higgs couplings to fundamental fermions is proportional to the fermion masses. Therefore, for a high-mass fermion like the top quark, the coupling to the Higgs boson is very large. The interaction of the Higgs boson with gauge bosons is proportional to the square of the boson masses. The Higgs couplings to gauge bosons and fermions are given by:

$$g_{HVV} = \frac{m_V^2}{v}, \qquad g_{Hf\bar{f}} = \frac{m_f}{v},$$

with $V = W^\pm$ or Z.

2.2.2 Bounds on the Higgs-boson mass

Theoretical Bounds

The theoretical upper bound can be determined from unitarity as well as from triviality. Considering the scattering of longitudinally polarized W bosons ($W_L^+ W_L^- \to W_L^+ W_L^-$), including W and Higgs exchanges, and requiring the unitary condition to be satisfied, the following upper bound on the Higgs mass is obtained [22]:

$$m_H < 860\,\mathrm{GeV}.$$

Upper bounds on the value of the Standard Model Higgs mass can also be obtained from what is called the triviality bound, i.e. from assumptions on the energy scale Λ up to which the SM can be extended. The parameter λ of the Higgs potential becomes energy dependent when quantum fluctuations are considered and they modify the self-interactions of the Higgs boson. Figure 2.2 shows the Feynman diagrams representing these quantum fluctuations. By requiring $\lambda(\Lambda)$ to be finite, an upper bound on the Higgs mass is estimated as:

$$m_H^2 \leq \frac{8\pi^2 v^2}{3 ln \Lambda^2/v^2}.$$

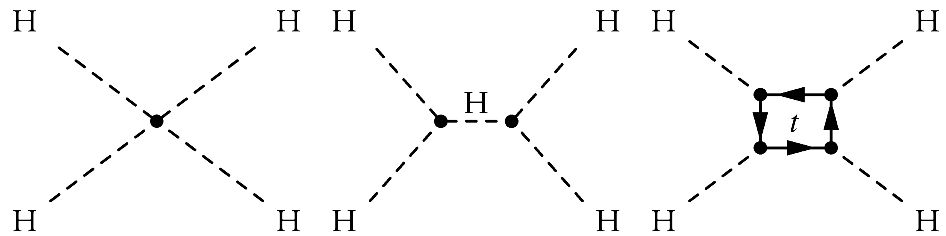

Figure 2.2: Diagrams generating the evolution of the Higgs self-interaction λ.

The top-loop correction in Figure 2.2 drives λ to smaller values, which can be even negative and, in this case, the ground state would not be stable anymore. To avoid it, the Higgs mass must be higher than a minimum value in order to balance this negative contribution. Therefore, a lower bound on the Higgs mass can be estimated by requiring vacuum stability. This lower bound depends indeed on the cut-off value, Λ. Figure 2.3 illustrates the bounds on the Higgs mass as a function of the cut-off value, Λ. If the SM is valid up the the grand unification scale ($\sim 10^{19}\,\mathrm{GeV}$), the Higgs mass should be between 130 and 180 GeV [18]. The lower bound on m_H can be reduced to about 115 GeV [23], if one allows for the electroweak vacuum to be metastable, with a lifetime greater than the age of the universe.

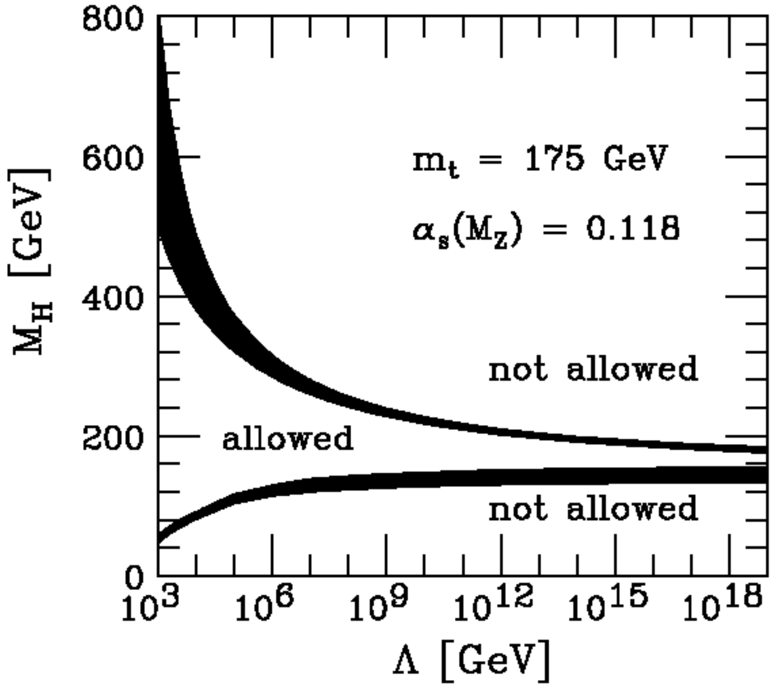

Figure 2.3: Bounds on the mass of the Higgs boson in the Standard Model as a function of Λ [24].

Experimental bounds on the Higgs mass

Direct searches for the Standard Model Higgs boson produced in the Higgs-strahlung process $e^-e^+ \to HZ$ at the LEP e^-e^+ collider, at center-of-mass energy up to 206 GeV, did not observe a significant excess of events over the Standard Model expectations. The combined results of the four LEP experiments set a lower bound on the SM Higgs-boson mass of 114.4 GeV, at 95% confidence level [25].

The combined results from the CDF and D0 experiments on direct searches for the Standard Model Higgs boson in $p\bar{p}$ collisions at the Fermilab Tevatron at $\sqrt{s} = 1.96$ TeV excluded, at 95% C.L., a new and larger region at high mass between $158 < m_H < 175$ GeV.

Constraints on the Higgs boson mass can be inferred from precise electroweak measurements performed at LEP and by CDF and D0. The accuracy of the measurements make them sensitive to the Higgs mass, which depends logarithmically on m_H through loop corrections. Figure 2.4 shows the $\Delta\chi^2$ curve derived from these measurements as a function of the Higgs mass. Currently, these measurements predict that the SM Higgs boson mass is $m_H = 89^{+35}_{-26}$ GeV [26]. The 95% confidence level upper limit is 158 GeV. It increases to 185 GeV when the lower limit on m_H of 114.4 GeV shown in yellow in Figure 2.4 is included.

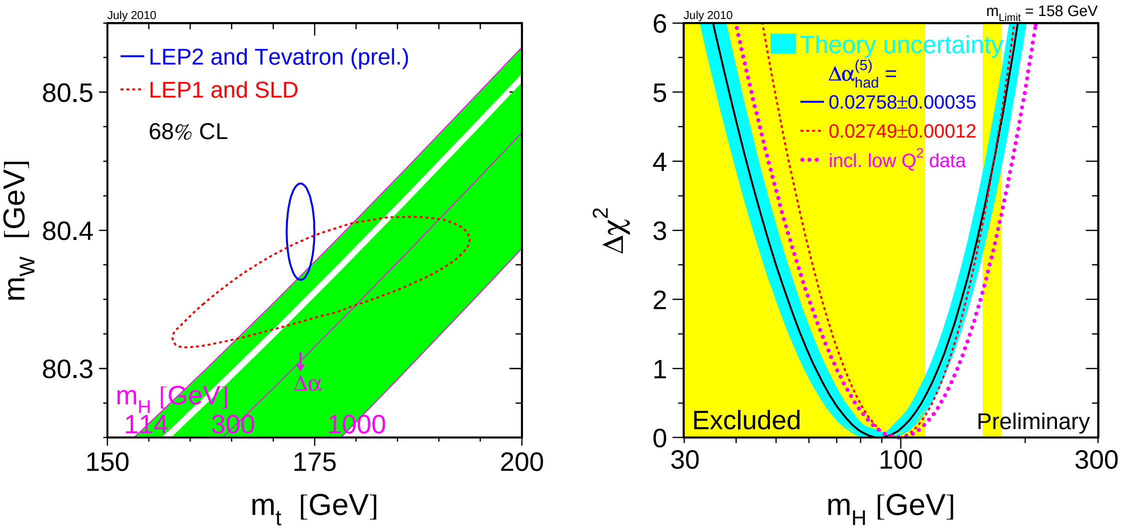

(a) (b)

Figure 2.4: (a) The comparison of the indirect constraints on m_W and m_t based on LEP-I/SLD data (dashed contour) and the direct measurements from the LEP-II/Tevatron experiments (solid contour). In both cases the 68% C.L. contours are plotted. Also shown is the SM relationship for the masses as a function of the Higgs mass in the region favored by theory (< 1000 GeV) and allowed by direct searches (114 GeV to 170 GeV and > 180 GeV) [26]. (b) $\Delta\chi^2 = \chi^2 - \chi^2_{min}$ as a function of the Higgs mass m_H. The solid line is the result of the fit using the precise measurements and the band represents an estimate on the theoretical error due to the missing higher order corrections. The yellow band shows the 95% confidence level exclusion limit on m_H from the direct search. The dashed curve is the result obtained using the evaluation of $\Delta\alpha_{had}(m_Z^2)$ [26].

2.2.3 Higgs searches at the ATLAS experiment

The search strategies for the Standard Model Higgs boson depend on its mass, which dictates both the production and the available decay modes. Figure 2.5(a) shows the decay branching ratios (BR) of the Standard Model Higgs boson as a function of its mass and Figure 2.5(b) the expected discovery significance in ATLAS for the various channels as a function of the Higgs boson mass. In the low mass region ($115 < m_H < 140$ GeV), favored by the precision electroweak measurements, the $H \to bb$ decay mode dominates but the $H \to \tau\tau$ contribution is still sizable and offers much cleaner signatures. Figure 2.5(b) illustrates the significant contribution of the $H \to \tau\tau$ decay mode for the low-mass SM Higgs discovery.

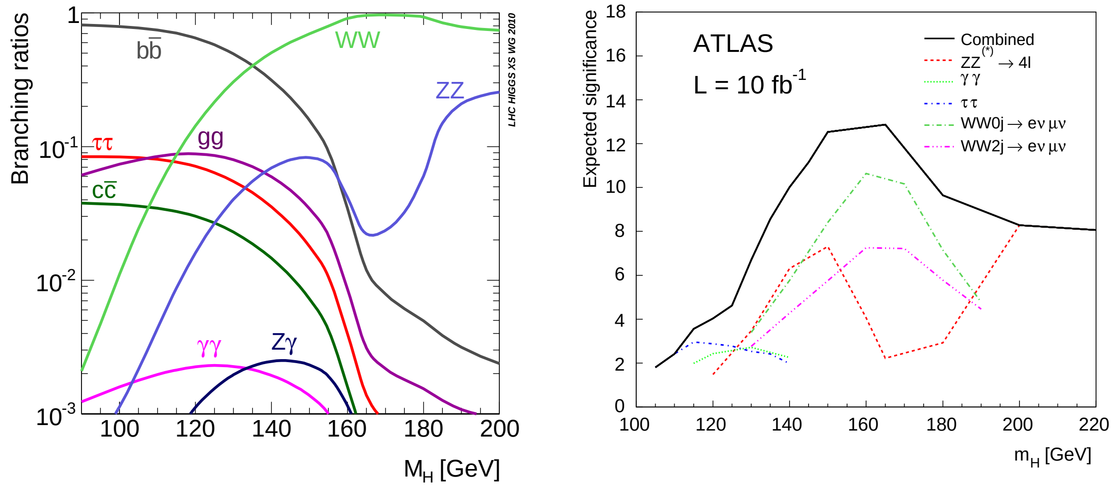

(a) (b)

Figure 2.5: (a) Branching ratios for the relevant decay modes of the Standard Model Higgs boson as a function of its mass [27]. (b) The median discovery significance for the various channels and their combination with an integrated luminosity of $10\,\mathrm{fb}^{-1}$ as a function of the Higgs boson mass [28].

2.3 Supersymmetry

The Standard Model is not considered to be a complete theory but rather an effective field theory and has to be extended by some new physics at some higher energy scale Λ. One problem originates from extrapolating the coupling strength of the fundamental forces measured at mass scales of a few 100 GeV to energies of about 10^{15} to 10^{19} GeV. Within the SM it does not lead to unification of forces at very high scales. Also, the SM does not include, for instance, the neutrino oscillations and the gravitational interaction.

Moreover, the SM has a serious problem known as the hierarchy problem. The cut-off Λ is m_{GUT} if the new physics is described by Grand Unified Theories (GUT), with e.g. $\sim 10^{15}$ GeV for $SU(5)$ GUT, and $m_{pl} \approx 10^{19}$ GeV (Planck mass) if the new physics is a unified theory with gravity. The hierarchy problem is the problem of how to maintain the hierarchy of the mass scales, i.e. $m_W \ll m_{\mathrm{GUT}}, m_{pl}$. This problem is more serious in the sector of scalar particles such as the Higgs particle, as the Higgs mass-squared gets a huge quantum correction proportional to m^2_{GUT} or m^2_{pl}. In fact, it is possible to adjust the bare mass of the Higgs, so that the renormalized Higgs mass remains at the weak scale. However, this requires an unnatural tuning of the bare parameter at the precision of $(m_W/m_{GUT})^2 \approx 10^{-26}$ [16]. SUSY is one of the most attractive ways to go beyond the SM and provides a cure for the hierarchy problem of the scalar sector.

The theory of supersymmetry hypothesizes a symmetry under the exchange of bosons and fermions. It is not only a possible symmetry but also a unique symmetry consistent with relativistic quantum field theory, besides internal symmetries such as gauge symmetry [16].

With the exception of spin these SUSY particles ('sparticles') possess the same quantum numbers as their SM counterparts. The fact that such states have not been observed in Nature implies that SUSY is broken by a mechanism which causes sparticles to acquire masses greater than SM states. Candidates of such a mechanism include gravity-mediation (mSUGRA models) as well as gauge-mediation (GMSB models) and anomaly-mediation (AMSB models). A further feature of many SUSY models is the conservation of a multiplicative quantum number known as R parity at each SUSY vertex, which causes SUSY states to be pair-produced and forces the lightest supersymmetric particle (LSP) to be neutral and stable [29]. If R is conserved, the Higgs boson can decay with a large branching ratio into lightest neutralinos or gravitinos leading to an invisible final state [30].

In the supersymmetric theory, coupling constants of a particle and its superpartners are identical, and the Feynman rule provides an additional negative sign for the diagram with a fermion loop. The hierarchy problem of the quadratic divergence can thus be solved since the quadratic divergences from the two diagrams in Figure 2.6 cancel with each other as long as the supersymmetry is exact [16].

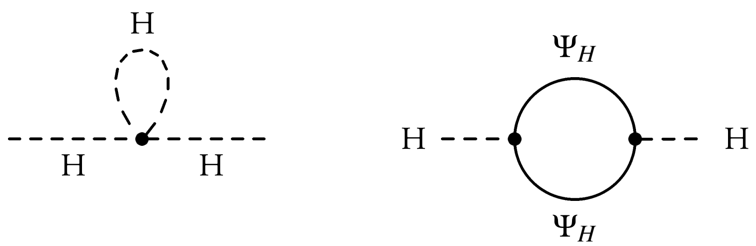

Figure 2.6: The diagram with a fermion loop provides a negative sign and the quadratic divergences from the two diagrams cancel with each other as long as the supersymmetry is exact.

In addition, introducing SUSY, the unification of the electromagnetic, weak and strong forces at the GUT scale is predicted and consistent with a SUSY mass scale of $\mathcal{O}(TeV)$. Finally, SUSY can accommodate gravity and, if R parity is conserved, the lightest of the new supersymmetric particles can provide a cosmologically interesting contribution to the dark matter.

2.3.1 SUSY searches at the ATLAS experiment

The Minimal Supersymmetric Standard Model (MSSM) is the minimal extension to the Standard Model that realizes supersymmetry. In the MSSM, two Higgs doublets are required, resulting in 5 physical states: $H^{\pm}$, h (neutral lighter scalar), H (neutral heavier scalar) and A (neutral pseudoscalar). At tree level their masses can be computed in terms of only two parameters, typically m_A and $\tan\beta$ (the ratio of the vacuum expectation values of the two doublets). In addition, $H \to \tau\tau$ and $A \to \tau\tau$ rates are strongly enhanced compared to the SM $H \to \tau\tau$

case over a large region of the parameter space. However, the observation of a charged Higgs boson would be a clear sign of new physics beyond the SM.

Figure 2.7 shows the charged Higgs boson BRs as a function of its mass for two MSSM scenarios [28]. Below the top quark mass, the charged Higgs boson predominantly decays into a τ lepton and a neutrino, and for values of $\tan\beta > 5$ this branching ratio is close to 100%, as shown in Figures 2.7(a) and 2.7(b). Once above the top quark mass threshold, the $H \to t\bar{b}$ decay mode shows a rapid growth and soon becomes an important decay mode as shown in Figure 2.7(a). However, the $H^+ \to \tau^+\nu$ decay mode is still important and provides a cleaner signature. Figures 2.7(c) and 2.7(d) show the calculated BRs for two different charged Higgs boson masses, one light (130 GeV) and one heavy (600 GeV), as a function of $\tan\beta$.

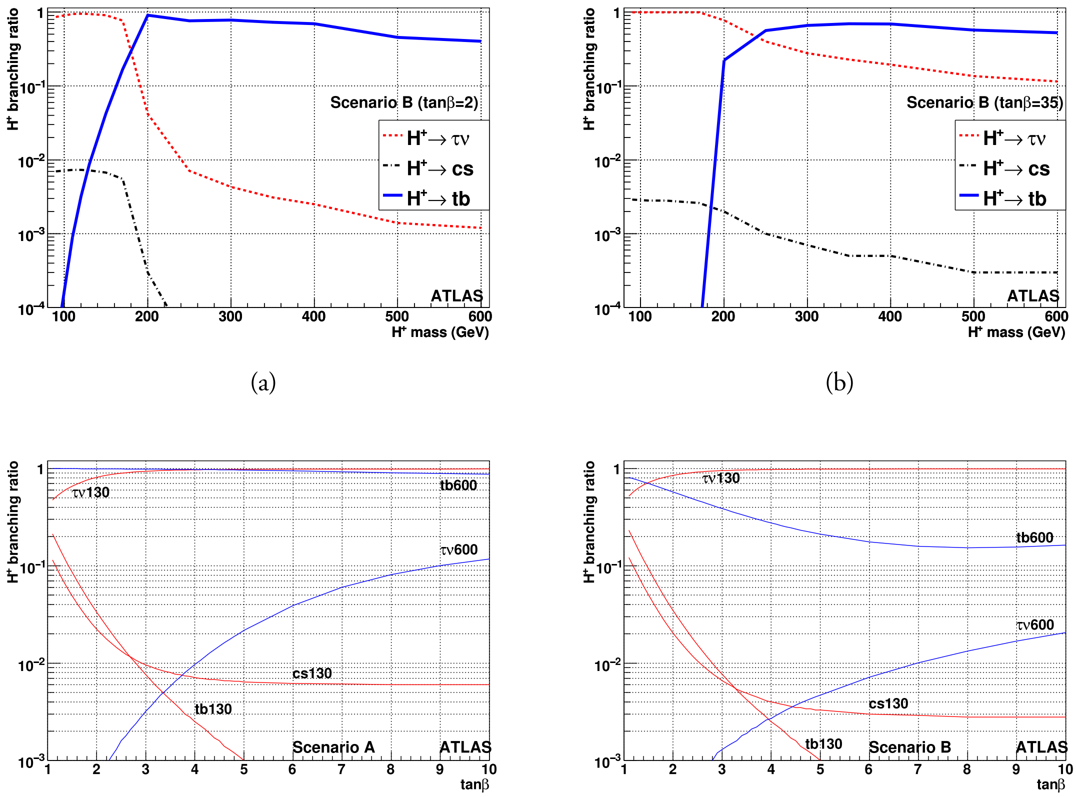

(a) (b) (c) (d)

Figure 2.7: Charged Higgs boson BRs as a function of its mass for the m_h-max scenario, i.e. the mass of the lightest Higgs boson h^0 is maximized, for (a) $\tan\beta = 2$ and (b) $\tan\beta = 35$ and three selected decay modes [28]. Expected charged Higgs boson BRs in the MSSM for scenarios (c) A (the decay of H^+ into SUSY particles is suppressed) and (d) B (m_h-max scenario) for a light ($m_{H^+} = 130$ GeV) and a heavy ($m_{H^+} = 130$ GeV) charged Higgs boson [28].

3. The LHC and the ATLAS Detector

3.1 The Large Hadron Collider

The LHC is a particle accelerator and collider designed to accelerate very intense proton beams to energies of up to 7 TeV. It is located at CERN, in the 27 km circular tunnel formerly used to house the LEP, an electron-positron collider. At the design luminosity of $10^{34}\,\mathrm{cm^{-2}s^{-1}}$, beam bunches will cross each other every 25 ns and provide, on average, 23 collisions per bunch crossing. The entire accelerating chain is illustrated in Figure 3.1. The two proton beams traveling in opposite directions require separate magnet dipole fields and vacuum chambers. The LHC uses twin bore superconducting magnets, which consist of two sets of coils and beam channels within the same mechanical structure and cryostat.

Six detectors have been constructed at the LHC. ATLAS and CMS are general-purpose experiments intended to operate at the peak luminosity. In addition, two other experiments are intended to run at lower luminosities. LHCb studies b-physics at a peak luminosity of $10^{32}\,\mathrm{cm^{-2}s^{-1}}$; TOTEM is designed for the detection of protons from elastic scattering at small angles, at a peak luminosity of $2 \times 10^{27}\,\mathrm{cm^{-2}s^{-1}}$. Furthermore, the LHC machine is also designed to accelerate heavy-ion beams, such as lead, which will collide at energies of up to 5.5 TeV per nucleon pair. ALICE is a dedicated ion experiment operating at a peak luminosity of $10^{27}\,\mathrm{cm^{-2}s^{-1}}$. LHCf, the smallest experiment, uses forward particles created inside the LHC as a source to simulate cosmic rays in laboratory conditions.

The proton beams were successfully circulated at the LHC for the first time in September 2008. Due to a serious electrical fault between two magnets resulting in a large helium leak into the tunnel, the operations were interrupted shortly after its opening and restarted in November 2009 at the injection energy of 450 GeV per beam. The first collision at a center-of-mass energy of $\sqrt{s} = 7\,\mathrm{TeV}$ took place on March 30$^{\mathrm{th}}$ 2010 with $\mathscr{L} = 2 \times 10^{27}\,\mathrm{cm^{-2}s^{-1}}$ and in October 2010 the luminosity reached $10^{32}\,\mathrm{cm^{-2}s^{-1}}$. At the end of the 7 TeV experimental period, by the end of 2012, the LHC will shut down for maintenance for up to two years and then it will attempt to reach the design energy of 14 TeV. The LHC has also started to collide heavy ion beams on November 7$^{\mathrm{th}}$ 2010. The lead-ion beams could be accelerated to the full energy of 287 TeV per beam.

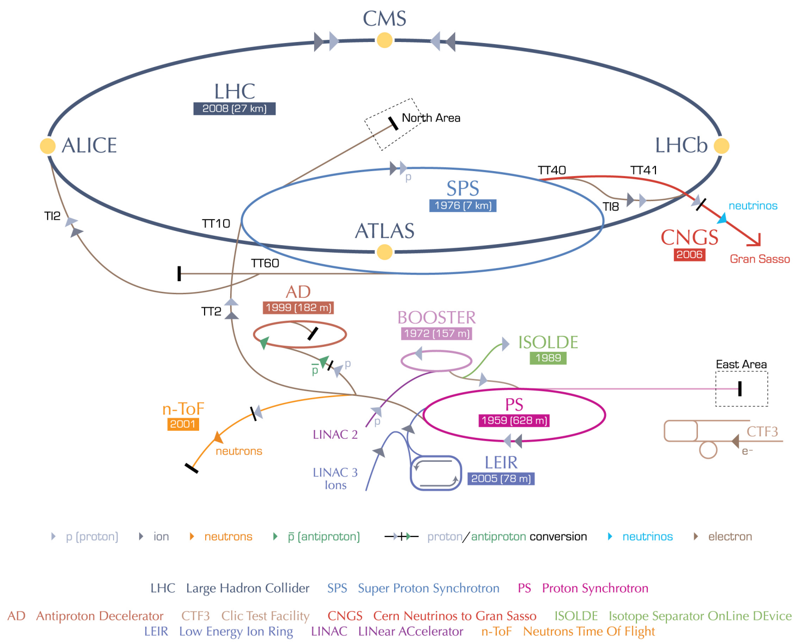

Figure 3.1: The CERN accelerator complex [31]. Prior to being injected into the LHC, the particles are pre-accelerated through a series of systems that successively increase the particle energy. Initially, protons are pre-accelerated to 50 MeV at the Proton Synchrotron and then accelerated to 1.4 GeV in the Proton Synchrotron Booster; subsequently, the Proton Synchrotron Ring raises the proton beam energy up to 26 GeV. Finally, the Super Proton Synchrotron increases the energy of protons up to 450 GeV and injects them into the LHC.

3.2 The ATLAS detector

ATLAS (**A** **T**oroidal **L**HC **A**pparatu**S**) is designed as a general-purpose detector. It has an approximate cylindrical shape and it consists of a tracking system in a 2 T solenoidal magnetic field, sampling electromagnetic and hadronic calorimeters and muon chambers in a toroidal magnetic field.

The nominal interaction point is defined as the origin of the coordinate system, see Figure 3.2. The anti-clockwise beam direction defines the z-axis and the $x-y$ plane perpendicular to it defines the transverse variables such as the transverse momentum, p_T, the transverse energy, E_T, and the missing transverse energy, E_T^{miss}. The positive x-axis direction points to the center of the LHC ring and the positive y-axis points upward. The azimuthal angle, ϕ, is measured around the beam axis and the polar angle, θ, is the angle from the beam axis. The pseudorapidity is defined as $\eta = -\ln\tan(\theta/2)$. The distance ΔR in $\eta - \phi$ space is defined as $\Delta R = \sqrt{\Delta\eta^2 + \Delta\phi^2}$.

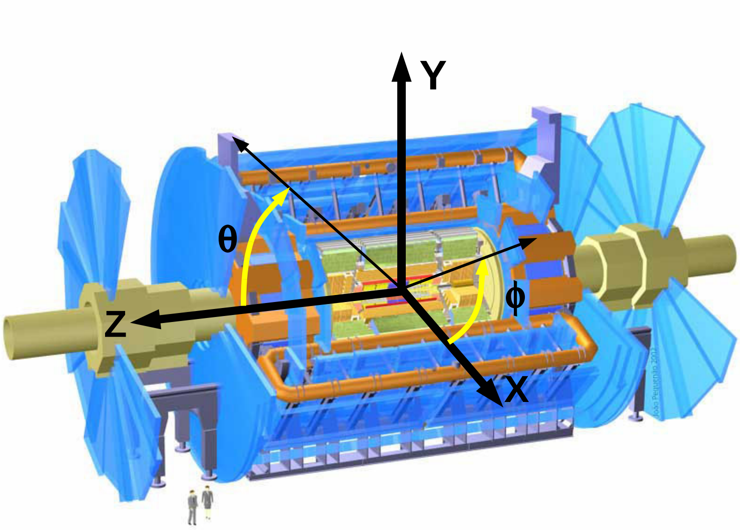

Figure 3.2: Illustration of the ATLAS coordinate system.

The ATLAS experiment is designed to provide excellent particle identification and precise measurements of its position, transverse momentum and transverse energy. In addition, efficient tracking at high luminosity for high-p_T physics objects is necessary in order to allow full event reconstruction capability and thus the interpretation of the events with reference to the different theoretical models. The presence of neutrinos (and other possible new weakly interacting and/or neutral particles) is indirectly inferred from the missing transverse energy. Therefore, the detector needs to completely surround the interaction point so that particles cannot be lost. Naturally, the beam-pipe imposes some limitation and the interaction products moving within this region will not be detected. The overall detector concept is illustrated in Figure 3.3 and will be briefly described in the following sections based on references [32–37].

3.3 Inner detector

The inner detector (ID) provides precise information in order to allow the reconstruction of tracks and vertices in the event. This information consists of very efficient and accurate position measurements of the particles along their tracks thus allowing the momentum and charge sign determination and consequently contributing to their identification.

Given the very large track density in the harsh environment of the LHC, the high-precision measurements performed by the inner detector are made with fine-granularity detectors. These requirements are achieved by using discrete high-resolution semiconductor pixel and strip detectors at the innermost radii and continuous straw-tube tracking detectors with transition-radiation capability in a pseudo-rapidity range matched by the precision measurements of the

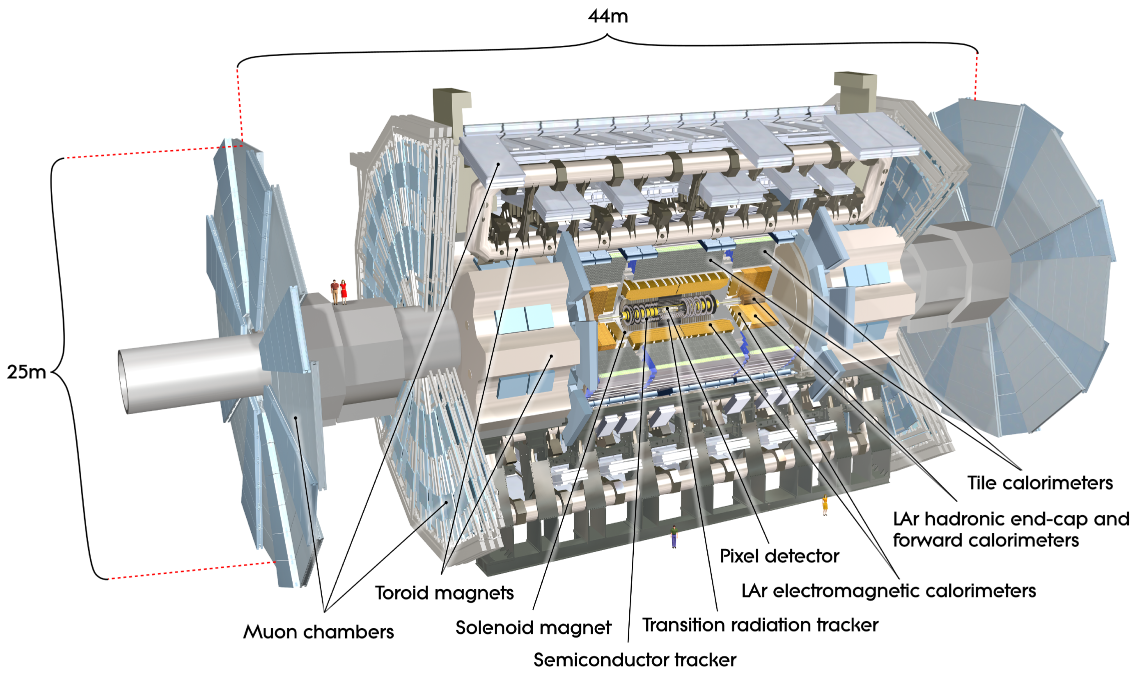

Figure 3.3: Cut-away view of the ATLAS detector [32].

electromagnetic calorimeter, see Figure 3.4. A magnetic field of 2 T directed along the beam axis is produced by a thin superconducting solenoid surrounding the inner detector cavity. The magnetic field then deflects the charged particle paths according to their transverse momentum permitting thus their p_T determination.

The whole ID system begins a few centimeters from the proton beam axis, extends to a radius of 1.15 m and is 7 m in length, limited respectively by the EM calorimeter and the end-cap calorimeters. It provides full tracking coverage over $|\eta| < 2.5$ and impact parameter measurements. The track efficiency as a function of transverse momentum, averaged over all pseudorapidities, raises from about 10% at 100 MeV to about 86% at high momentum [38]. For a central track with $p_T = 5\,\text{GeV}$, the relative transverse momentum resolution is around 1.5% and the transverse impact parameter resolution is about 35 μm [32].

3.3.1 Pixel detector

The task of the pixel detector is to provide high-granularity and high-precision measurements of charged-particle tracks as near as possible to the interaction point. By measuring the impact parameter, particles that were produced at a secondary vertex can be identified as daughters of particles such as b-quarks. It is thus essential for heavy-flavor tagging, lifetime measurements and associating tracks to the correct primary vertex at high luminosity.

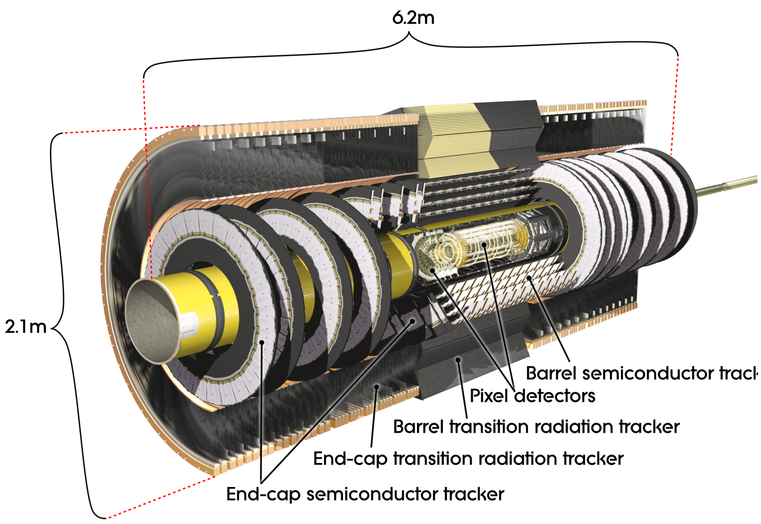

Figure 3.4: Cut-away view of the ATLAS inner detector [32].

The system consists of three barrel layers parallel to the beam axis and five disks on each side covering the η acceptance of $|\eta| < 2.5$. The barrel layers have radii of 5.05 cm, 8.85 cm and 12.25 cm and contain 1456 barrel modules while the disks, which lie between radii of 11 cm and 20 cm, contain 288 disk modules.

Both barrel modules and disk modules are designed to be identical. Each module is 60.8 mm long and 16.4 mm wide, with 46080 pixel elements, $50 \times 400\,\mu$m each, read out by 16 chips. Each readout chip is bump-bonded to the detector substrate with individual circuits for each pixel element.

3.3.2 Semiconductor tracker

The semiconductor tracker detector consists of four barrel layers in the central region while the forward modules are mounted in up to three rings on nine wheels. Each module is composed of four single-sided p-on-n silicon detectors with long, narrow strips rather than small pixels. The module is arranged with two detector pairs glued back-to-back. As a result, the system provides eight precision measurements per track in the barrel region. The $R-\phi$ coordinate is precisely measured from the hit strip(s) while the z-coordinate is measured using a 40 mrad stereo angle between the front and back planes.

The system contributes to the momentum, impact parameter and vertex-position measurements, as well as providing good pattern recognition by the use of high granularity.

The spatial resolution is $17\,\mu$m in $R-\phi$ and $580\,\mu$m in z and tracks can be distinguished if separated by more than $\sim 200\,\mu$m.

3.3.3 Transition radiation tracker

The transition radiation tracker (TRT) is formed by several straw detectors, each of which is a cylindrical tube, with 4 mm in diameter and up to 144 cm long, filled with a gas mixture of Xe, CO_2 and CF_4. The xenon gas allows the detection of transition-radiation photons created in the radiator (polypropylene foils or fibers) between the straws. These are soft X-rays produced when ultra-relativistic charged particles cross the boundary between two materials with different dielectric constants. The detection of transition radiation provides information for electron identification.

There are two independent thresholds to distinguish between tracking hits and transition-radiation (TR) hits. The tracking hits pass the lower threshold while the TR hits pass the higher one. The TRT provides good pattern recognition performance by using the continuous tracking (typically 36 hits per track) and assists in the particle identification by using the TR (e.g. discriminate between electron and pion tracks).

3.4 Calorimetry

The calorimeter is required to provide a very good capability to measure energy and position of electrons and photons, energy and direction of τ leptons and jets as well as the ability to differentiate the various physics objects. Furthermore, the calorimeter needs to have good hermeticity to better determine the missing transverse energy. Therefore, it covers the pseudo-rapidity region $|\eta| < 4.9$ (equivalent to $0.85^\circ \lesssim \theta \lesssim 179.15^\circ$). Any cracks in the detector and material (cables and cooling system) should be avoided. The calorimeter must be thick enough to provide good containment for hadronic showers and reduce shower-leakage into the muon system.

The electron and photon measurement is based on the showers produced by these highly energetic particles when incident upon matter. They initiate particle cascades from pair production ($\gamma \to e^+e^-$) and bremsstrahlung ($e \to e\gamma$) in the presence of the nuclear electric field. Their shower can be characterized longitudinally by the radiation length (X_0) and by the narrow transverse profiles.

High-energy hadrons also produce cascades when interacting with dense material, where multiplication occurs through a succession of inelastic hadron-nuclear interactions. Such showers are laterally more spread than the EM ones.

To achieve these previous requirements, the ATLAS calorimeter is divided into an inner electromagnetic and an outer hadronic part which are shown in Figure 3.5. It is composed of the electromagnetic (EM) calorimeter covering $|\eta| < 3.2$, the hadronic barrel calorimeter in $|\eta| < 1.7$, the hadronic endcap calorimeters in the range $1.5 < |\eta| < 3.2$, and finally the forward calorimeters covering $3.1 < |\eta| < 4.9$.

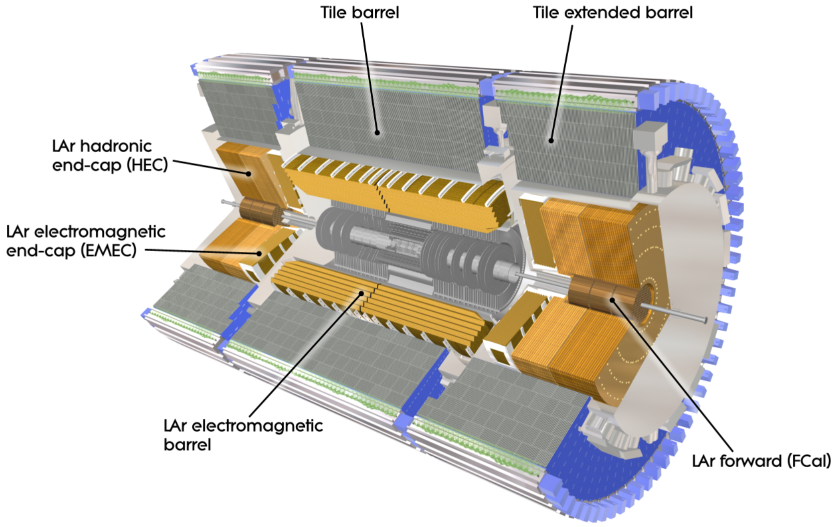

Figure 3.5: A cut-away drawing of the ATLAS inner detector and calorimeters. The tile hadronic calorimeter consists of one barrel and two extended barrel sections and surrounds the liquid argon barrel electromagnetic and endcap hadronic calorimeters. The inner detector is shown in gray in the innermost radii of ATLAS [32].

3.4.1 Liquid argon electromagnetic calorimeter

The EM calorimeter is a high granularity lead-liquid-argon (LAr) sampling calorimeter formed by interspaced layers of LAr, accordion-shaped Kapton electrodes and lead absorber plates over its full coverage. The accordion geometry provides a complete ϕ symmetry and fast signal which is important for bunch-crossing identification. The total thickness of the EM calorimeter is $> 22\ X_0$ in the barrel and $> 24\ X_0$ in the end-caps.

Over the region devoted to precision physics ($|\eta| < 2.5$), the EM calorimeter (barrel and end-cap) is segmented into three longitudinal samplings (two in the end-cap η region), see Figure 3.6. The first sampling has a constant thickness of $\sim 6\ X_0$ and is equipped with narrow η strips ($\Delta\eta \times \Delta\phi = 0.003 \times 0.1$) which provide high resolution in η. These strips act as preshower detector and the time segmentation enhances γ/π^0, e/π separation.

The second sampling is segmented into square towers of size $\Delta\eta \times \Delta\phi = 0.025 \times 0.025$ for precise position measurement. Electrons with high energy can reach the last sampling which has a granularity of 0.05 in η. In addition, presamplers consisting of one layer of LAr in front of the EM calorimeter are used to correct for the energy loss in the solenoid and cryostat wall.

In the forward region, the hadronic calorimeter is also of liquid argon technology to withstand the high radiation levels. The very forward hadronic calorimeter (down to $|\eta| < 4.9$) is made of copper and tungsten to limit the width and depth of the showers from high energy jets close

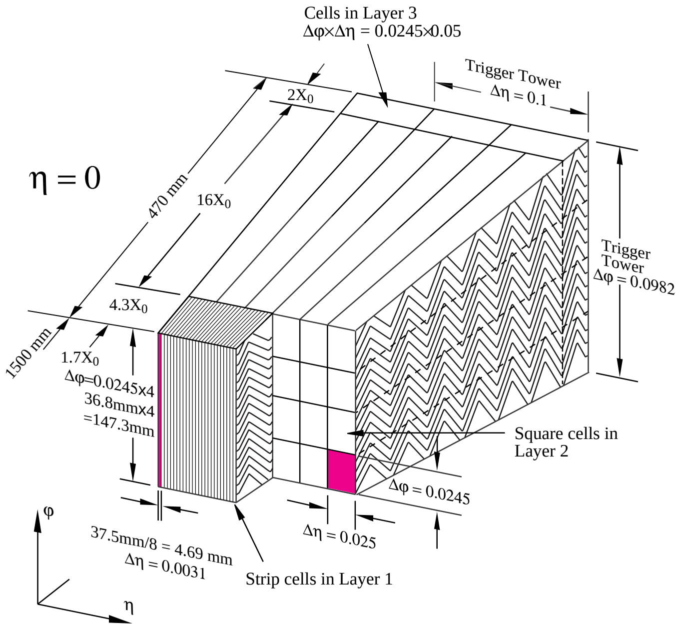

Figure 3.6: Sketch of a barrel module [32].

to the beam pipe and to keep the background level low in the surrounding calorimeters from particles spraying out from this forward region.

The EM calorimeter performance is designed to reach an energy resolution for electrons and photons of $\sigma/p_T = 0.05\% p_T \oplus 1\%$ [32], with p_T in GeV.

3.4.2 Hadronic calorimeter

The tile calorimeter is a large hadronic sampling calorimeter using iron as absorber medium and scintillating tiles as the active material. The calorimeter has a central η range out to 1.7 and longitudinally extends to an outer radius of 4.25 m with a bore radius of 2.28 m. The light created in the scintillators is read out by wavelength-shifting (WLS) fibers into photomultipliers placed on the outside of the calorimeter. The fibers absorb the blue light from the scintillators and reemit it at longer wavelengths where it reaches the photomultipliers through total reflection inside the fibers.

The hadronic end-cap calorimeter consists of two independent wheels per end-cap, located behind the end-cap electromagnetic calorimeter and sharing the same LAr cryostats. The wheels are built from parallel copper plates interleaved with LAr gaps, providing the active medium for this sampling calorimeter. The forward calorimeter (FCal) is approximately 10 interaction lengths deep, and consists of three modules in each end-cap: the first, made of copper, is optimized for electromagnetic measurements, while the other two, made of tungsten, measure predominantly the energy of hadronic interactions.

The performance goal of the ATLAS detector is to reach energy resolution for jets in the barrel and end-cap of $\sigma_E/E = 50\%/\sqrt{E} \oplus 3\%$ and $\sigma_E/E = 100\%/\sqrt{E} \oplus 10\%$ in the forward hadronic calorimeters [32], with E in GeV.

3.5 Muon spectrometer

Muons, with no strong interaction and relatively large mass, lose their energy primarily by ionization. They can thus pass through the calorimeter into dedicated detectors which can identify them and measure their momenta. Due to the relatively small volume of the inner detector the accuracy of the muon transverse momentum measurements becomes limited at higher energies and a muon spectrometer plays therefore an important role. As a result of the combined information of both independent measurements the momentum resolution is improved. Moreover, it allows background rejection and correct identification of muons in heavy-flavored jets.

The muon spectrometer forms the outer shell of the ATLAS detector. It lies on the outside of the calorimeter modules, covers a radius between 4.5 and 11 m and extends approximately 23 m along the beam axis on both sides of the interaction point. The arrangement of the muon chambers is shown in Figure 3.7.

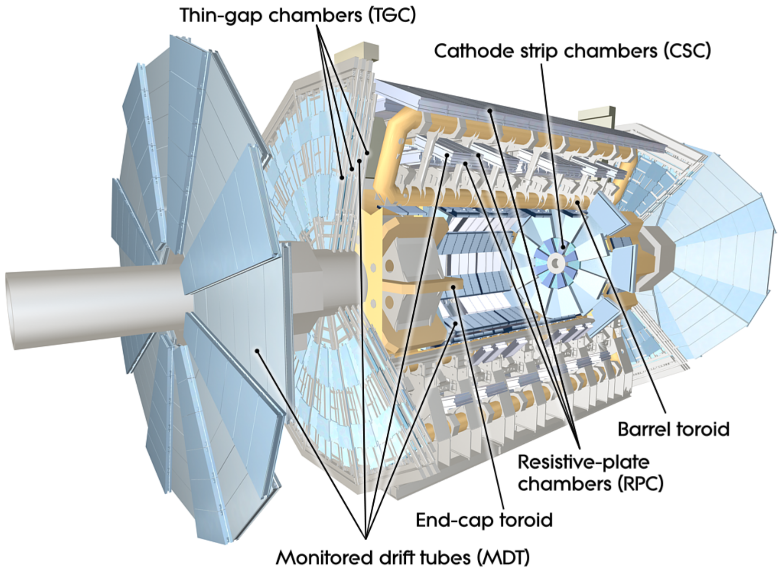

Figure 3.7: Cut-away view of the ATLAS muon system [32].

An average magnetic field strength of 0.6 T in the muon system is produced by superconducting air-core toroids. Over $0 < |\eta| < 1.0$, the large barrel toroid provides the magnetic bending. In the forward region ($1.4 < |\eta| < 2.7$), muon tracks are bent by two smaller end-cap magnets while in the transition region, $1.0 < |\eta| < 1.4$, magnetic deflection is provided by a combination of barrel and end-cap fields. In particular, this magnetic configuration provides a field that is mostly perpendicular to the muon trajectories.

The chambers are placed such that particles which originate at the interaction point traverse three chamber stations around the beam axis. Wherever possible, the chambers measure the sagitta of the curved tracks in three positions. In the end-caps, where the toroid cryostat prevents chambers from being placed inside the magnetic field, the muon momentum is measured from the difference in entry and exit angle of the magnet.

The precision measurement in the bending direction is made by the Monitored Drift Tube (MDT) chambers. Particles are measured in 2×4 sensitive layers in the inner station and in 2×3 layers in the middle and outer stations in order to improve resolution and redundancy for pattern recognition.

At large pseudo-rapidities, cathode strip chambers (CSC's) with higher granularity are used in the innermost plane in the region $2.0 < |\eta| < 2.7$, to withstand the demanding rate and background conditions expected with the LHC operation at the nominal luminosity and center-of-mass energy. The muon trigger system, which covers the pseudo-rapidity range $|\eta| < 2.4$, consists of resistive plate chambers (RPC's) in the barrel ($|\eta| < 1.05$) and thin gap chambers (TGC's) in the end-cap regions ($1.05 < |\eta| < 2.4$), with a small overlap in the $|\eta| = 1.05$ region.

Finally, the momentum resolution of the spectrometer requires an accuracy of $30\,\mu$m for the positioning of chambers within a projective tower and in the millimeter range for the relative positioning of different towers. The stringent requirements on the relative alignment of the muon chamber layers are met by a combination of precision mechanical-assembly techniques and optical alignment systems, both within and between muon chambers, that constantly monitor chamber deformations and positions for a later correction during the offline analysis. A transverse momentum resolution of about 3% over most of the momentum range is expected. A resolution of 10% is expected for a p_T of 1 TeV.

3.6 Magnet system

The ATLAS superconducting magnet system is an arrangement of the central solenoid (CS) providing the inner detector with a central magnetic field of 2 T, surrounded by a system of three large air-cored toroids generating the magnetic field for the muon spectrometer, Figure 3.8. The latter comprises the two end-cap toroids (ECT) inserted in the barrel toroid (BT) at each end and lined up with the CS. The peak magnetic fields on the superconductors in the BT and ECT are 3.9 and 4.1 T, respectively. The overall dimensions of the magnetic system are 26 m in length and 20 m in diameter.

The CS coil is designed to be as thin as possible and it shares one common vacuum vessel with the LAr calorimeter, thereby eliminating two vacuum walls and minimizing the material in front of the EM calorimeter. This is very important in order to achieve the desired calorimeter performance. Each of the three toroids consists of eight coils assembled radially and symmetrically around the beam axis.

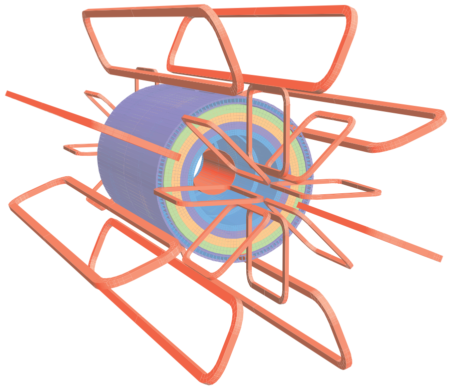

(a)

(b)

Figure 3.8: (a) Geometry of magnet windings and tile calorimeter steel. The eight barrel toroid coils, with the end-cap coils interleaved are visible. The solenoid winding lies inside the calorimeter volume. The tile calorimeter is modeled by four layers with different magnetic properties, plus an outside return yoke. (b) Bare central solenoid [32].

3.7 Trigger

The trigger system of the ATLAS detector has to reduce the initial bunch-crossing rate of 40 MHz (interaction rate of about ~ 1 GHz at the design luminosity) to approximately 200 Hz. To reach this goal, it is organized in three levels in which the trigger decision is taken by custom electronics at the first level (level-1), whereas the following levels, collectively called "high-level trigger" (HLT), operate in a software environment that processes the events, similarly to the offline reconstruction. Each level refines the decision made at the previous one and, where necessary, applies additional selection criteria to reduce the trigger output rate stored on disks.

The level-1 trigger system is implemented in custom hardware processors and uses simple algorithms to make fast decisions. It identifies muons in the muon spectrometer using only the resistive-plate chambers in the barrel and the thin-gap chambers in the endcaps. Electromagnetic clusters (electron/photon), τ leptons decaying into hadrons or single hadrons, jets, as well as large missing and total transverse energy are also identified by the level-1 trigger based on the reduced-granularity information from all the ATLAS calorimeters. In the case of the electron/photon and τ/hadron triggers, isolation can be applied. The maximum acceptance rate of the level-1 trigger is limited to 75 kHz and is determined by the capabilities of the sub-detector readout systems. Operation at up to about 100 kHz is possible with somewhat increased dead-time.

The level-2 trigger algorithms are largely based on the use of the Regions of Interest (RoIs) information provided by the level-1 trigger. The RoIs consist of regions in η-ϕ space in the detector identified by the level-1 trigger as containing interesting information as well as the p_T of candidate objects, $E_{\mathrm{T}}^{\mathrm{miss}}$ and $\sum E_T$. In principle, the level-2 trigger has access to the entire event data with the full precision and granularity, but only a small fraction of it ($\sim 2\%$), corresponding to the RoIs, is needed. The rate is reduced by the level-2 trigger to ~ 1 kHz with an average event treatment time to take the decision of approximately 10 ms.

Finally, the EF works at the level-2 acceptance rate and uses fully-built events for analysis. In particular, complete event reconstruction using more sophisticated trigger algorithms, based on offline code and more complete and detailed calibration information, is feasible at this third-level trigger in order to make a final decision. This final event selection has an average processing time of one second. With massive parallel processing, it reduces the initial rate to about 200 Hz for full events of size ~ 1.5 Mbyte. These accepted events are subsequently written on mass-storage media for offline analysis.

The τ trigger is designed to select hadronic decays of the τ lepton, which are characterized by the presence of one or three charged pions accompanied by a neutrino and possibly neutral pions (the signatures of hadronic τ decays will be described in detail in Section 5.1). At the level-1 trigger, the τ trigger uses the electromagnetic and hadronic calorimeter trigger towers to calculate the energy in a core and an isolation region. A trigger tower is a set of cells belonging to different calorimeter samplings (comprising both electromagnetic and hadronic calorimeters), which occupy the same area in the projective space (η, ϕ). At the level-2 trigger, selection criteria are applied using tracking and calorimeter-based information. This takes advantage of narrowness and low track multiplicity to discriminate τ leptons from the multi-jet background. Exploiting the same characteristics, the EF uses different selection criteria for 1-prong and multi-prong decays in more refined algorithms which are similar to the offline reconstruction algorithms [39].

At each trigger level, the scalar sum of the transverse energy, $\sum E_T$, deposited in the full calorimeter is computed together with $E_{\mathrm{T}}^{\mathrm{miss}}$. For the $E_{\mathrm{T}}^{\mathrm{miss}}$ and $\sum E_T$ triggers, at level-1, trigger-towers are used to compute both the scalar and vector sums over the full ATLAS acceptance ($|\eta| < 4.9$). At level-2, the level-1 energy measurement is corrected with the measured momenta of detected muons in the event (muons do not deposit much energy in the calorimeters and level-1 uses only the calorimeter-measured energy). At the EF, contributions from both calorimeters and muon spectrometers are recomputed using the full granularity of the detectors [40, 41].

3.8 Luminosity measurement

The LHC luminosity is determined in real time approximately once per second using a number of detectors and algorithms, each having different acceptances, systematic uncertainties and sensitivity to background. LUCID is a Cherenkov detector dedicated to measuring the luminosity in ATLAS, consisting of sixteen aluminum tubes filled with C_4F_{10} gas surrounding the beampipe on each side of the interaction point at a distance of 17 m. During offline analysis, additional luminosity algorithms are studied and are compared to online results to further constrain systematic uncertainties on the measurement. Smaller uncertainties of 11% are obtained using an absolute calibration of the luminosity via beam separation scans and are dominated by the systematic uncertainty on the measurement of the LHC beam current [42].

4. Monte Carlo Event Generator, Detector Simulation and Event Reconstruction

To be able to compare theoretical predictions at parton level with the experimental observation of the final-state particles, the detector response to these particles needs to be simulated. This chapter presents the corresponding software tools used throughout this thesis. The ATLAS simulation chain is divided into the Monte Carlo (MC) event generation, detector simulation and digitization and full event reconstruction. The event generators are introduced in the next section. The software for detector simulation and the event reconstruction chain is described in Section 4.2. Finally, the algorithms used for the reconstruction of the physics objects in the event are presented in Section 4.3 and the MC samples used in this thesis are listed in Section 4.4.

4.1 Event generators

Event generators are indispensable tools used for modeling the complex physics processes that occur during the beam collisions at high-energy physics experiments. The production of Monte Carlo events for proton-proton collisions can be divided into few general steps [43]. First, a pair of partons (quark or gluon) from each incoming proton interacts, as illustrated in Figure 4.1. This parton-parton interaction is called the *hard process* and the interaction between these two partons is described by a *matrix element*. The phenomenology of these partons is encoded in the parton distribution function, i.e. the distribution of the momentum fraction, x, of the parton in the hadron in the relevant kinematic range.

Higher-order QCD effects are added to the leading-order hard process by allowing the partons to split into pairs of other partons ((anti)quark into $\overset{(-)}{q}g$ pairs and gluon into $q\overline{q}$ or gg pairs). The resulting pairs may also branch, producing a shower of partons[1] (*parton shower*). Showering of the initial partons is also included in the process. The colored partons are then

[1]Though the discussion of parton shower presented here is restricted to QCD showers, an identical prescription can be applied to electromagnetic showers to incorporate higher-order QED corrections.

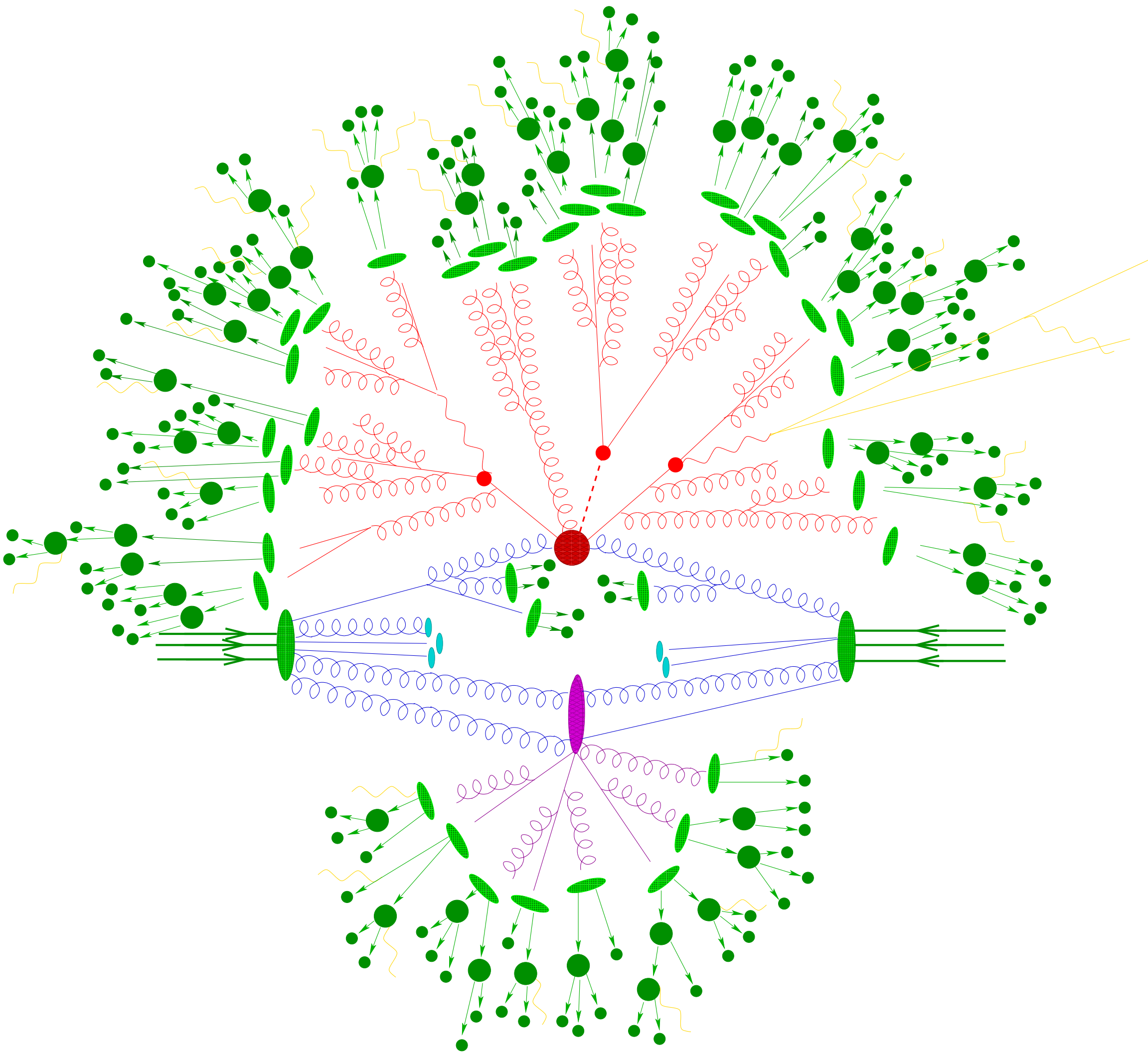

Figure 4.1: Sketch of a proton-proton collision at high-energies [44]. A pair of partons (dark blue) from each incoming proton (large green blob) interacts. The hard interaction is represented by the large red blob, producing jets. The final state parton shower is pictured in red, the fragmentation in light green and the hadron decays in dark green. The beam remnants are represented by the light blue blobs and the underlying event by the purple blob. Photon radiation occurs at any stage (yellow).

grouped into color-singlet hadrons using a phenomenological model referred to as *hadronization*. After hadronization, many short-lived resonances will be present and decay into stable[2] final-state particles. Finally, the underlying structure of the event is added, i.e. the colored remains of the proton which are left behind after the hard partonic scattering (beam remnants) and additional interactions from other partons in the hadrons. The partonic scatter not originating from the primary hard process or its products is referred to as the *underlying event*.

[2] Stable in the sense that it does not decay within the detector range.

For the present work, Pythia [45] is used as the generator for the signal and background events. It runs from inside the Athena framework, which is the ATLAS common analysis framework using the Gaudi architecture [46, 47]. This framework is the basis for all ATLAS applications and it consists of a set of specific packages developed to perform all tasks, from the primary proton-proton collision to the reconstruction of the energies and momenta of the particles coming out of these evens including, for instance, the detailed detector geometry, misalignments, simulation of the electronic signals and noise.

4.1.1 Pythia

Pythia is a general-purpose generator for events in pp, e^+e^- and ep colliders. It contains a subprocess library and generation machinery, initial- and final-state parton showers, underlying event, hadronization and decays. Pythia starts with the hard scattering process calculated to lowest order in QCD and add additional QCD and QED radiation in a shower approximation which is most accurate when the radiation is emitted at small angle. It also uses a model for hard and soft scattering processes in a single event in order to simulate underlying activity. This model is used in the simulation of minimum-bias events [48].

The MC samples are created using a tuned set of parameters denoted as ATLAS MC09 [49] with the MRST2007LO [13, 50] modified leading-order parton density functions. Another tune, the DW tune [51], uses virtuality-ordered showers and was derived to describe the CDF II underlying event and Drell-Yan data. The DW tune seems to model the forward activity of the underlying event better than the MC09 tune, and describes the jet shapes and profiles in data more accurately. The studies presented in this thesis used the MC09 tune, unless stated otherwise. The DW tune was used to estimate systematic uncertainties associated with the Monte Carlo modeling.

4.1.2 Tauola and Photos

The incorporation of spin effects in τ lepton decays is often of high importance. The τ leptons from the decay of gauge bosons carry information on the polarization of the decaying resonance and, in the case of pair production, also some information about the spin correlations. The simulation of those effects has been implemented into the interface of the Tauola package and Monte Carlo generators [52, 53], both provided by the Athena framework. The τ leptons from $W \to \tau\nu_\tau$ decays are 100% longitudinally polarized, with $P_{\tau^+}, P_{\tau^-} = +1.0$. For $Z \to \tau\tau$, there is a correlation between the polarization of the τ leptons [48]. It is a more complicated function of the center-of-mass energy of the system and the angle of the decay products [54].

Photos handles electromagnetic radiation [55] and it is used by Tauola. Photos is also used to improve the description of electromagnetic radiation in, for example, the decay $W \to e\nu_e$, where radiation distorts the electron energy distribution. In these cases the final state electromagnetic radiation is switched off in the general purpose generator to avoid double counting.

4.2 Detector simulation

The information produced by the event generators is then processed in the simulation step. First, hits, which are a record of the interactions of particles in the detector, are produced [48]. These hits carry information like position, energy deposit, identifier of the active element, etc. They are subsequently digitized and transformed into Raw Data Objects (RDOs).

The detector simulation is based on the GEANT4 toolkit [56] which provides optimized solutions for geometry description and navigation through the geometry, propagation of particles through detectors, description of materials, modeling of physics processes and detector response to particles. The detector description also includes misalignments in the inner detector and calorimeter. The active detector elements then produce the hits. Agreement between the simulation and test beam measurements is very good, typically at the level of 1% [57]. In addition, the simulation reproduces the full trigger chain. However, the detector-simulation part is the most time-consuming and requires much CPU power and memory.

During the digitization process, the hits produced are translated into the output form similar to what is expected from the readout electronics in the actual experiment. In addition, the propagation of charges into the active media, as in the tracking detectors and in the liquid argon calorimeter, of light, as in the case of the tile calorimeter, as well as the response of the readout electronics have to be considered during the digitization. Noise injection is also performed at this level. The final outputs are RDOs that resemble the real detector data.

4.2.1 Simulation of pile-up effects

Pile-up can be simulated with the Athena-based pile-up application during the digitization step. The pile-up effects considered are [48]:

- **Minimum bias:** the mean number of minimum-bias interactions per bunch crossing depends linearly on luminosity and bunch spacing. This value in a single bunch follows a Poisson distribution, with a long tail beyond the most probable value. The hits of the minimum-bias events are then overlaid onto the hits from the hard scattering event.

- **Cavern background:** neutrons (and a smaller contribution from long-lived neutral kaons and low-energy photons escaping the calorimeter) may propagate through the ATLAS cavern for a few seconds before they are thermalized, thus producing a neutron-photon gas. This gas produces a constant background, called *cavern background*, of low energy electrons and protons from spallation.

- **Beam gas:** includes residual hydrogen, oxygen and carbon gases in the ATLAS beam pipe that may interact with the beam at any place along the beam pipe.
- **Beam halo:** is the background resulting from interactions between the beam and upstream accelerator elements (in the tunnel and collimators).

In addition, the ATLAS subdetectors are sensitive to hits several bunch crossings before and after the BC that contains the hard scattering event. All of these detector and electronic effects are taken into account during the pile-up event merging [48].

4.3 Object reconstruction

The identification of $W \to \tau\nu$ decays relies on the measurement of $E_{\mathrm{T}}^{\mathrm{miss}}$, on the τ_{h} identification and on the rejection of jets, electrons and muons. The reconstruction of $E_{\mathrm{T}}^{\mathrm{miss}}$, jets, electrons and muons is discussed in the following section. Given the importance of the τ reconstruction and identification for the $W \to \tau\nu$ observation, it will be discussed separately in Chapter 5.

4.3.1 Missing transverse energy

The reconstruction of missing transverse energy is based on calorimeter information. This relies on a cell-based algorithm which sums the energy deposits of calorimeter cells inside three-dimensional topological clusters (topoclusters) [58]. These clusters are seeded by calorimeter cells with energy $|E_{\mathrm{cell}}| > 4\sigma$ above the noise, where σ is the RMS of the noise. All direct neighbors are iteratively added for all cells with signals above a secondary threshold $|E_{\mathrm{cell}}| > 2\sigma$. Finally, the energy in all further immediate neighbors is added. Clusters are split or merged based on the position of the local minima and maxima. The cell energies are summed to give the cluster energy. The baseline calibration for these clusters corrects their energy to the electromagnetic scale, which was established using test-beam measurements for electrons and muons in the electromagnetic and hadronic calorimeters [59–61]. The topoclusters are then corrected to take into account the different responses to hadrons and to electrons or photons, dead material losses and out-of-cluster energy losses [62]. The x- and y-components of the calorimeter $E_{\mathrm{T}}^{\mathrm{miss}}$ term are calculated by summing over the transverse energies measured in these topological cluster cells i, calibrated according to the local hadron calibration scheme [63]:

$$E_{x,y}^{\mathrm{miss}} = -\sum_i E_{i,x,y}^{\mathrm{Calo}} . \tag{4.1}$$

The variable $E_{\mathrm{T}}^{\mathrm{miss}}$ is defined as:

$$E_{\mathrm{T}}^{\mathrm{miss}} = \sqrt{(E_x^{\mathrm{miss}})^2 + (E_y^{\mathrm{miss}})^2}. \tag{4.2}$$

The resolution of $E_{\mathrm{T}}^{\mathrm{miss}}$ has been measured in minimum-bias events and depends on the scalar sum of the transverse cell energies:

$$\sum E_T = \sum_i \sqrt{(E_{i,x}^{\mathrm{Calo}})^2 + (E_{i,y}^{\mathrm{Calo}})^2}. \tag{4.3}$$

If $E_{\mathrm{T}}^{\mathrm{miss}}$ and $\sum E_T$ are expressed in GeV, the $E_{\mathrm{T}}^{\mathrm{miss}}$ resolution is $\sigma(E_{x,y}^{\mathrm{miss}}) = 0.49\sqrt{\sum E_T}$ [64].

The significance of the missing transverse energy is defined as

$$S_{E_{\mathrm{T}}^{\mathrm{miss}}} = \frac{E_{\mathrm{T}}^{\mathrm{miss}}}{0.5 \cdot \sqrt{\sum E_T}}, \tag{4.4}$$

where $E_{\mathrm{T}}^{\mathrm{miss}}$ and $\sum E_T$ are expressed in GeV and the factor 0.5 was chosen to be similar to the actual measurement of the $E_{\mathrm{T}}^{\mathrm{miss}}$ resolution.

4.3.2 Jet reconstruction

Jets reconstructed with the anti-k_{t} jet algorithm [65] are used in this thesis. Here, some of the general properties of this algorithm are reviewed. The anti-k_{t} jet algorithm is well-motivated since it can be implemented in next-to-leading-order perturbative QCD calculations, is infrared safe[3] to all orders and produces geometrically well-defined ("cone-like") jets [67]. The algorithm is based upon pair-wise clustering of the initial constituents. It defines a distance measured between objects, and also some condition upon which clustering should be determined. This algorithm constructs, for each input object (e.g. a parton, particle or energy) i, the quantities d_{ij} (distance between two objects) and d_{iB} (distance between the object and the beam) as follows:

$$d_{ij} = \min(k_{Ti}^{-2}, k_{Tj}^{-2}) \frac{(\Delta R)_{ij}^2}{R^2}, \tag{4.5}$$

$$d_{iB} = k_{Ti}^{-2}, \tag{4.6}$$

where k_{Ti}^{-2} is the transverse momentum of object i. A list containing all the d_{ij} and d_{iB} values is compiled. If the smallest entry is d_{ij}, objects i and j are combined (their massless four-vectors are added to form the final four-momentum of the jet) and the list is updated. If the smallest entry is d_{iB}, this object is considered a complete "jet" and is removed from the list. The variable R is a resolution parameter which sets the relative distance at which jets are resolved from each other as compared to the beam. In ATLAS, the two most common choices of values for the R parameter are: $R = 0.4$ and $R = 0.6$. For the studies presented in this thesis, the value $R = 0.4$

[3]The presence of additional soft particles between two particles belonging to the same jet should not affect the recombination of these two particles into a jet. In the same sense, the absence of additional particles between these two should not disturb the correct reconstruction of the jet. Generally, the number of jets produced should not be affected by any soft particles not coming from the fragmentation of a hard scattered parton [66].

is used.

The input objects to the jet algorithm are topological energy clusters in the calorimeter [58]. The present calibration scheme calibrates the reconstructed jets using p_T and η dependent correction factors derived from simulated events. To derive these jet energy scale correction factors, "particle" jets reconstructed using the Monte Carlo event record are matched with jets reconstructed in the calorimeter within a cone of $\Delta R = 0.3$, and the correction is calculated by dividing the true particle jet energy by the EM-scale energy of the matching calorimeter jet. This correction is derived for jets with $p_T > 10\,\text{GeV}$ at the EM-scale and is parameterized as a function of jet p_T and $|\eta|$ [68].

The Monte Carlo simulation describes the jet energy resolution measured from data within 14% for jets with p_T values between 20 and 80 GeV in the rapidity range $|y| < 2.8$ [69]. An uncertainty of 3-4% on the response to single isolated hadrons in the calorimeter is measured for jets in the central region of the detector $0 < |\eta| < 0.8$ with a transverse momentum range between 20 GeV and 1 TeV. This was measured with an integrated luminosity of approximately $300\,\mu\text{b}^{-1}$ of proton-proton collisions at a center-of-mass energy of $\sqrt{s} = 7\,\text{TeV}$ collected in April 2010 by the ATLAS experiment [70].

4.3.3 Electron reconstruction

An electron is identified as a cluster in the electromagnetic calorimeter with an associated track. The electron reconstruction and identification algorithm [71] is designed to provide various levels of background rejection optimized for high identification efficiencies, over the full acceptance of the inner-detector system. The *loose* electron identification uses EM shower shape information from the second layer of the EM calorimeter (lateral shower containment and shower width) and energy leakage into the hadronic calorimeters as discriminant variables. This set of requirements providing high and uniform identification efficiency is used to veto events containing electrons.

4.3.4 Muon reconstruction

The ATLAS muon identification and reconstruction algorithms take advantage of the multiple sub-detector technologies which provide complementary approaches and cover pseudorapidities up to 2.7 over a wide p_T range [72]. They rely on the muon spectrometer for standalone muon reconstruction and on the inner detector and calorimeters for combined muon reconstruction. Tracks and track segments found in the muon spectrometer are associated with the corresponding inner-detector track to identify muons at their production vertex, imposing requirements on track quality and muon-system hit multiplicity.

4.4 Simulated data samples

The signal and background Monte Carlo samples used for this analysis were generated for proton-proton collisions at a center-of-mass energy of $\sqrt{s} = 7$ TeV with Pythia 6.421 and passed through the full GEANT4 simulation of the ATLAS detector. Table 4.1 summarizes the Monte Carlo datasets used in this thesis. The background contribution expected from jet production via QCD process (referred to as "QCD background" in this thesis) were also produced with Pythia 6.421 using leading-order perturbative QCD matrix elements for $2 \to 2'$ processes. The allowed range of transverse momentum of outgoing partons, $\hat{p}_T$, defined in the rest frame of the hard interaction, is restricted to $\hat{p}_T$ intervals as presented in Table 4.1. The motivation to split the production of simulated jets in $\hat{p}_T$ intervals is to increase the number of simulated events in the kinematic region more relevant for physics analysis.

Physics process	$\mathscr{L}_{\text{int}}[\text{nb}^{-1}]$	Cross section × BR [nb]	Note
$W \to \tau\nu_\tau$	1.43×10^4	10.46	pile-up $< \text{n}_{\text{vertex}} >= 2$
$W \to e\nu_e$	6.31×10^4	10.46	pile-up $< \text{n}_{\text{vertex}} >= 2$
$W \to \mu\nu_\mu$	9.56×10^4	10.46	pile-up $< \text{n}_{\text{vertex}} >= 2$
$Z \to ee$	1.01×10^6	0.99	pile-up $< \text{n}_{\text{vertex}} >= 2$
$Z \to \mu\mu$	1.01×10^6	0.99	pile-up $< \text{n}_{\text{vertex}} >= 2$
$Z \to \tau\tau$	1.01×10^5	0.99	pile-up $< \text{n}_{\text{vertex}} >= 2$
$W \to \tau_{\text{h}}\nu_\tau$	1.49×10^4	10.46×0.6479	no pile-up
J0 ($8 < \hat{p}_T < 17$ GeV)	0.14	9.86×10^6	no pile-up
J1 ($17 < \hat{p}_T < 35$ GeV)	2.06	6.78×10^5	no pile-up
J2 ($35 < \hat{p}_T < 70$ GeV)	34.1	4.10×10^4	no pile-up
J3 ($70 < \hat{p}_T < 140$ GeV)	6.35×10^2	2.20×10^3	no pile-up
J4 ($140 < \hat{p}_T < 280$ GeV)	1.59×10^4	0.88×10^2	no pile-up
J5 ($280 < \hat{p}_T < 560$ GeV)	5.92×10^5	2.35×10^0	no pile-up
J6 ($560 < \hat{p}_T < 1120$ GeV)	4.01×10^7	3.36×10^{-2}	no pile-up
J0 ($8 < \hat{p}_T < 17$ GeV)	3.67×10^{-2}	9.86×10^6	DW tune + no pile up
J1 ($17 < \hat{p}_T < 35$ GeV)	4.91×10^{-1}	6.78×10^5	DW tune + no pile up
J2 ($35 < \hat{p}_T < 70$ GeV)	9.05	4.10×10^4	DW tune + no pile up
J3 ($70 < \hat{p}_T < 140$ GeV)	1.79×10^2	2.20×10^3	DW tune + no pile up
J4 ($140 < \hat{p}_T < 280$ GeV)	4.52×10^3	0.88×10^2	DW tune + no pile up

Table 4.1: Monte Carlo datasets used in the analysis. For the MC samples including pile-up effects, $< \text{n}_{\text{vertex}} >$ corresponds to the average number of vertices per event. The variable $\hat{p}_T$ is the transverse momentum of the partons involved in the hard scatter. W and Z cross sections are given at NNLO and the QCD background cross sections are given at leading order (LO).

5. Reconstruction and Identification of Hadronic τ Decays

As discussed in the introduction, τ leptons play an important role in the physics program at the LHC. In particular, they provide an important signature in searches for a low-mass Higgs boson and in many new physics searches where they are present in the final states. For these searches, τ decays need to be identified in a wide momentum range, from about 10 GeV to at least 500 GeV [32]. The low energy range is optimized for analyses related to W and Z gauge boson observations with τ decays as well as to Higgs boson searches and SUSY cascade decays. The higher energy range is mostly of interest, for example, in searches for heavy Higgs bosons in MSSM models.

The reconstruction and identification algorithms are developed to efficiently reconstruct and identify the hadronic decays, while providing a large rejection of QCD background. This is a difficult task at hadron colliders due to the enormous multi-jet production cross section. This chapter present the reconstruction and identification algorithms used in ATLAS to efficiently select τ_{h} decays.

The characteristic properties of τ lepton decays are presented in the next section. These decay properties are used to build a set of reconstruction and identification variables. Section 5.2 describes the two algorithms used in ATLAS to reconstruct τ_{h} candidates. Particular emphasis is given to the procedure to select tracks associated with the charged τ_{h} decay products and its optimization for the first collisions at the LHC. In the early stages of data-taking, the identification criteria are based on a small number of well-understood discriminating variables, as described in Section 5.3. A set of identification variables are also combined in multivariate discriminants, namely boosted decision trees and projective likelihood methods [32, 73], which are going to be used for the measurement of the $W \to \tau\nu_\tau$ production cross section at the LHC.

In Section 5.4, the reconstruction and identification algorithms for hadronic τ decays are investigated by measuring properties of QCD jets with the first LHC collisions and comparing them with predictions from Monte Carlo simulations. This commissioning is very important at this early data-taking phase to give confidence in the performance of the ATLAS algorithms that are later used for the observation of real τ leptons from W decays.

5.1 The τ lepton

The τ lepton together with the τ neutrino form the third generation of leptons. The world average value for the τ lifetime [18] is $(290.6 \pm 1.0) \times 10^{-15}$ s and its precision of 0.3% is dominated by the LEP measurements [74]. Due to its short lifetime, the proper decay length of τ leptons is 87.11 μm, thus decaying inside the beam pipe. Therefore, the identification of τ leptons is done through their decay products inside the detector.

The τ lepton, with a mass of 1776.82 ± 0.16 MeV, is the only lepton heavy enough to decay both leptonically and hadronically. Table 5.1 shows the τ decay branching ratios.

τ decay modes	Γ_i/Γ
$\tau \to e\nu_e\nu_\tau$	17.85%
$\tau \to \mu\nu_\mu\nu_\tau$	17.36%
$\tau \to \nu_\tau\ h^\pm\ \geq 0$ neutral (single-prong)	49.51%
$\tau \to \nu_\tau\ h^\pm h^\pm h^\mp\ \geq 0$ neutral (three-prong)	15.19%
$\tau \to \nu_\tau\ h^\pm h^\pm h^\pm h^\mp h^\mp\ \geq 0$ neutral (five-prong)	1.02×10^{-3}%
others	8.9×10^{-2}%

Table 5.1: The τ decay branching ratios [18]. "$h^\pm$" stands for $\pi^\pm$ or $K^\pm$ and "neutrals" for γ's and/or π^0's.

The τ lepton decays approximately 65% of the time to one or more hadrons and the remaining fraction to electrons or muons, in both cases with accompanying neutrinos. The following decay signatures, illustrated in Figure 5.1, are used to identify hadronic τ decays:

- The fraction of hadronically decaying τ leptons to one or three charged tracks are approximately 77% and 23%, respectively, with a track multiplicity lower than those of QCD jets.

- Their decay products tend to be well collimated and to form a narrow hadronic shower in the calorimeter.

- The invariant mass of the visible decay products is usually smaller than those of QCD jets.

- High leading-track momentum fraction.

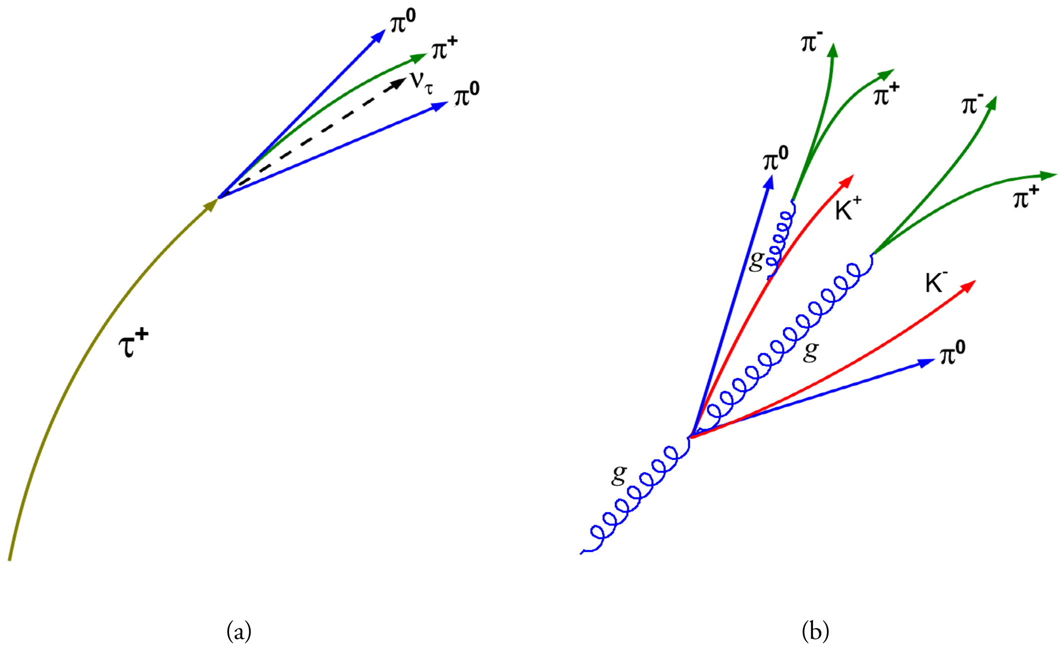

Figure 5.1: Illustration of (a) a hadronic τ decay and (b) a gluon-initiated QCD jet.

5.2 Reconstruction of hadronic τ decays

The τ reconstruction algorithm relies on the inner detector and calorimeter information. The inner detector provides information on the charged hadronic single or collimated track system reconstructed in isolation from the rest of the event. The charge of the decaying τ lepton can be directly determined from the charge(s) of its decay product(s). The τ candidate is said to be reconstructed as n-prong if there are n tracks associated to it. Particular attention has been given to minimize the amount of charge misidentification and of migration between the single- and three-prong categories in the reconstruction (Section 5.2.1). Calorimetry provides information on the energy deposit from the visible decay products. Hadronically decaying τ leptons are well collimated resulting in a relatively narrow shower in the electromagnetic calorimeter with, for single-prong decays with one or few π^0's, a significant electromagnetic component. The calorimeter and tracking information should match, with narrow calorimeter clusters being found close to the track(s) impact point in the calorimeter.

ATLAS employs two complementary hadronic τ reconstruction algorithms starting from either calorimeter or track seeds in the pseudorapidity range $|\eta| < 2.5$ [73]:

- **Track-seeded:** these τ_h candidates have a seeding track with $p_T > 6\,\text{GeV}$ satisfying further quality criteria (Section 5.2.1). This algorithm is optimized for τ_h with transverse momenta between 20 and 70 GeV [75], which corresponds to hadronic τ decays from $W \to \tau\nu_\tau$ and $Z \to \tau\tau$ processes. An energy flow calculation [73] is used to determine the τ_h energy, where energy deposits in cells matched to charged tracks in a narrow cone of $\Delta R = 0.0375$ are subtracted and replaced by the momentum of such tracks. This energy flow determination is also corrected for energy leakage coming from charged particles outside the narrow cone.

- **Calorimeter-seeded:** these τ_h candidates are seeded by calorimeter jets reconstructed with the anti-k_t algorithm [76] (using a distance parameter $D = 0.4$) starting from topological clusters (topoclusters) [58]. The τ_h candidate is required to have $p_T > 10\,\text{GeV}$ calibrated using the global cell weighting (GCW) calibration scheme [62, 77]. The p_T of the τ_h candidate is further adjusted by applying multiplicative factors derived from Monte Carlo studies, in order to reconstruct the p_T of signal τ_h accurately. This algorithm has been optimized for visible transverse energies above 30 GeV, which corresponds to hadronic τ decays from Higgs-boson decay.

Candidates are labeled *double-seeded* when a track-seeded candidate and a calorimeter-seeded candidate are within a distance $\Delta R < 0.2$ of each other. Double-seeded candidates are identified with higher purity [78]. The global cell weighting calculation is considered the default energy. For reconstructed τ leptons in $Z \to \tau\tau$ events, 70% of τ candidates have two valid seeds, 25% have only a calorimeter-seed and 5% have only a track seed [79].

The reconstruction of τ candidates provides very little rejection against QCD jet backgrounds. Rejection comes from a separate identification step which is discussed in Section 5.3. It should be stressed, however, that the reconstruction algorithms also calculate the information used for τ_h identification.

5.2.1 Track selection criteria for τ_h reconstruction

The track selection should ensure a high efficiency and quality of the reconstructed tracks over a broad dynamic momentum range, from 1 GeV to a few hundred GeV. Both the calorimeter-based and the track-based algorithms determine the charge of the τ candidates by summing up the charge of the tracks reconstructed in the *core* region. The core region for track-seeded (calorimeter-seeded) algorithm is $\Delta R < 0.2(0.3)$ cone around reconstructed direction of the visible decay products. Therefore, the selection criteria for tracks from charged pions arising in τ decays is an important ingredient for an efficient τ identification.

The charge misidentification for the hadronically decaying τ lepton is dominated by combinatorial effects: single-prong decays may migrate to three-prong category due to photon conversions or the presence of additional tracks from the underlying event. A three-prong decay might be reconstructed as a single-prong decay due to inefficiencies in track reconstruction and selection. In the low-p_T range, the inefficiency is due to hadronic interactions in the inner-detector material. For hadronic τ-decays with high energy, the performance is degraded due to the strong collimation of the multiple tracks from three-prong decay. Also the contribution from the charge misidentification of the individual tracks should not be neglected.

In 2008 there were some improvements to the track algorithms and the simulations included a more realistic description of the detector geometry (where more material was introduced). Therefore, the track selection criteria for τ_{h} candidates were revisited in order to look for possible improvement on the track selection efficiency, the τ_{h} charge identification efficiency and the migration between *n*-prong categories. It was also investigated if the track selection procedure for track-seeded candidates could be simplified by reducing the number of track quality criteria from three to two. In addition, track selection definitions developed for [32] in the context of *b*-tagging were tried out. The advantage of using the same selection as the ATLAS Tracking Working Group is that these track selection criteria would be widely studied in terms of efficiency and systematics with the first data, avoiding a separate study for the specific track selection criteria used for the τ_{h} reconstruction.

Track-seeded candidates

Former track selection criteria for the reconstruction of track-seeded candidates used a seed track with $p_T > 6\,\mathrm{GeV}$ passing quality criteria. The p_T requirement reduces the physics efficiency for observing τ_{h} in the low p_T range but the advantage of this approach is the strong rejection power against QCD background already at the reconstruction step. The quality criteria require a minimal number of hits in the silicon detector, a threshold on the value of the impact parameter with respect to the interaction vertex as well as a threshold on the value of the χ^2 of the fit for the trajectory reconstruction. In addition, the number of low-threshold TRT hits has to be larger than 10 in a pseudorapidity η range up to 1.9, while for the stricter second quality track (2^{nd} trk) the presence of a b-layer[1] hit and ratio of the high-to-low threshold hits ($\mathrm{N}_{\mathrm{TRT}}^{\mathrm{HT}}/\mathrm{N}_{\mathrm{TRT}}^{\mathrm{LT}}$) of smaller than 0.2 is required. Both requirements were added to minimize the number of accepted tracks from photon conversions. The exact selection criteria are specified in Table 5.2. The algorithm associates second quality tracks (2^{nd} trk) to the seed track (1^{st} trk) within a cone of 0.2 around it. If the τ_{h} candidate has a total of two qualified tracks, then the track criteria on the value of the χ^2, on the presence of a b-layer hit and on the ratio $\mathrm{N}_{\mathrm{TRT}}^{\mathrm{HT}}/\mathrm{N}_{\mathrm{TRT}}^{\mathrm{LT}}$ are dropped to search for additional tracks (3^{rd} trk), enhancing the efficiency for 3-prong τ_{h} reconstruction. Candidates with more than 8 tracks are not considered as a valid track-seeded candidate. A dedicated veto against electron tracks being used as leading tracks

[1] The innermost pixel layer.

is not applied at the reconstruction level. This will be taken care of separately as part of the identification procedure.

Using a sample of $Z \to \tau\tau$ Monte Carlo events, each track quality requirement were varied and the τ selection efficiency, charge identification efficiency and migration between n-prong categories were determined. The former track quality criteria was still tuned at best performance and no significant improvement was obtained.

As discussed above, two different quality levels were developed for b-tagging [32]. For the *standard* quality level, the reconstructed tracks are required to have at least seven precision hits (pixels and SCT). In addition, the transverse and longitudinal impact parameters must fulfill following conditions $|d_0| < 2\,\mathrm{mm}$ and $|z_0| \cdot \sin(\theta) < 10\,\mathrm{mm}$, respectively. For a stricter selection requirement, called *b-tagging*, the extra requirements are: at least two hits in the pixels, one of which should be in the vertexing layer (b-layer), as well as $|d_0| < 1\,\mathrm{mm}$ and $|z_0| \cdot \sin(\theta) < 1.5\,\mathrm{mm}$. These criteria are listed in Table 5.2.

Track criteria	**Standard**	***b*-tagging**	**Calo-seeded**	**Track-seeded**		
				1^{st} **trk**	2^{nd} **trk**	3^{rd} **trk**
p_T [GeV] $>$	1	1	1	6	1	1
$\|d_0\|$ [mm] $<$	2	1	1.5	1	1	1
$\|z_0\| \cdot \sin(\theta)$ [mm] $<$	10	1.5	-	-	-	-
$\chi^2/ndf <$	-	-	3.5	1.7	1.7	-
TRT hits ($N_{TRT} \geq$)	-	-	-	10	-	-
Silicon hits ($N_{Si} >$)	7	7	6	8	8	8
Pixel hits ($N_{pixel} \geq$)	-	2	2	-	-	-
b-layer hits ($N_{b-layer} \geq$)	-	1	1	-	1	-
$N^{HT}_{TRT}/N^{LT}_{TRT} <$	-	-	-	-	0.2	-

Table 5.2: Definition of several track quality criteria for standard tracks, b-tagging tracks, and former track selection requirements used for track-seeded and calorimeter-seeded candidates.

Several combinations of track quality criteria using the former track quality criteria, the standard criterion and the b-tagging criterion were tried out. The best combination, in terms of track selection efficiency, charge identification efficiency and migration between n-prong categories, was obtained using the standard requirement as the seed track, but with a higher p_T threshold of $6\,\mathrm{GeV}$, and the b-tagging criterion as the looser track. No third quality track was required. Table 5.3 shows a comparison between performances using the former track quality criteria and this new recommendation. Hadronic τ candidates from simulated $Z \to \tau\tau$ events were used for this study.

The results presented in Table 5.3 show that the recommended new definition of track quality criteria significantly improves the track selection efficiency, charge identification and migration

	1-prong τ_h			**3-prong τ_h**		
	ε(%)	1P→3P (%)	Charge (%)	ε(%)	3P→1P (%)	Charge (%)
Former criteria	83.1 ± 0.1	1.41 ± 0.04	99.50 ± 0.03	63.4 ± 0.3	6.28 ± 0.14	94.78 ± 0.16
Recommended	87.2 ± 0.1	1.00 ± 0.04	99.24 ± 0.03	65.8 ± 0.3	3.72 ± 0.11	98.61 ± 0.08

Table 5.3: Track selection performance using the default track-seeded quality tracks and the new recommended one: standard tracks as the seed track, but $p_T > 6$ GeV, and the *b*-tagging selection for additional tracks around the seeding track. No third quality tracks are required. The track selection efficiency, migration between *n*-prong categories and electric charge efficiencies are shown for 1-prong and 3-prong τ_h decays from $Z \to \tau\tau$ simulated events. The *n*-prong category is classified at the event generator level.

between *n*-prong categories. It is also simpler than the former track selection criteria because it does not use a third quality track. Therefore, it has been implemented in the ATLAS τ_h reconstruction algorithm for track-seeded candidates.

Calorimeter-seeded candidates

Tracks are associated with the calorimeter-seeded τ candidate if they lie within a cone radius of $\Delta R < 0.3$ around the direction of the τ_h candidate. The quality requirements for these tracks are shown in Tables 5.2 as *calo-seeded*. Similar to the track-seeded τ_h reconstruction, the track quality criteria used for the calorimeter-seeded τ_h algorithm were investigated by varying each track quality requirement. No significant improvement was obtained. However, using the *b*-tagging instead of the default quality cuts, very similar performance compared to the former criteria was obtained, as can be observed in Table 5.4. Since the *b*-tagging selection is better understood and more reliable with first data than the default selection, it has been implemented in the ATLAS τ_h reconstruction algorithm for calorimeter-seeded candidates as well.

	1-prong τ_h			**3-prong τ_h**		
	ε(%)	1P→3P (%)	Charge (%)	ε(%)	3P→1P (%)	Charge (%)
Former criteria	84.5 ± 0.1	1.27 ± 0.04	99.15 ± 0.03	66.8 ± 0.3	4.51 ± 0.14	98.10 ± 0.09
Recommended	84.1 ± 0.1	1.12 ± 0.03	99.27 ± 0.03	65.6 ± 0.3	4.96 ± 0.11	98.61 ± 0.08

Table 5.4: Track selection performances using the former calorimeter-seeded quality track and the *b*-tagging selection as recommended criterion. The track selection efficiency, migration between *n*-prong categories and electric charge efficiencies are shown for 1-prong and 3-prong τ_h decays from $Z \to \tau\tau$ simulated events. The *n*-prong category is classified at the event generator level.

5.3 Hadronic τ identification

After the reconstruction of τ candidates, an identification step must be performed to distinguish candidates originating from hadronically decaying τ leptons and those originating from QCD jets. The variables that are used in the identification of hadronic τ decays (τ_h-ID) with early data are the following [73, 80]:

- **Track radius:** p_T-weighted ΔR of tracks associated with the τ_h candidate,

$$R_\mathrm{track} = \frac{\sum_i^{\Delta R_i < 0.2} p_\mathrm{T,i} \Delta R_i}{\sum_i^{\Delta R_i < 0.2} p_\mathrm{T,i}}, \tag{5.1}$$

  where i runs over all tracks associated with the τ_h candidate, R_i are defined relative to the calorimeter jet axis and $p_\mathrm{T,i}$ are the track transverse momenta.

- **Electromagnetic radius:** transverse-energy-weighted shower width in the electromagnetic calorimeter,

$$R_\mathrm{EM} = \frac{\sum_i^{\Delta R_i < 0.4} E_\mathrm{T,i}^\mathrm{EM} \Delta R_i}{\sum_i^{\Delta R_i < 0.4} E_\mathrm{T,i}^\mathrm{EM}}, \tag{5.2}$$

  where i runs over all cells in the first three layers of the EM calorimeter associated with the τ_h candidate, R_i are defined relative to the calorimeter jet axis, and $E_\mathrm{T,i}^\mathrm{EM}$ are the cell transverse energies ($E_T = E/\cosh(\eta)$).

- **Leading track momentum fraction:**

$$f_\mathrm{trk,l} = \frac{p_\mathrm{T,l}^\mathrm{track}}{p_\mathrm{T}^\tau}, \tag{5.3}$$

  where $p_\mathrm{T,l}^\mathrm{track}$ is the transverse momentum of the leading track of the τ_h candidate and p_T^τ is the visible transverse momentum of the τ_h candidate.

Selection criteria on these variables, presented in Table 5.5, are defined to provide a *loose*, *medium* and *tight* identification with average efficiencies for τ_h from simulated $Z \to \tau\tau$ decays of 60%, 50%, and 30%, respectively. The efficiencies are calculated with respect to the number of true hadronically decaying τ leptons with $p_T^{vis} > 10\,\mathrm{GeV}$ and $|\eta| < 2.5$. The measured efficiencies for background jets with a loose, medium and tight identification are of about 30%, 10% and 2%, respectively [80].

In addition, identification methods are also used to distinguish hadronically decaying τ leptons from electrons and muons:

n-prong	level	$R_{\text{track}} <$	$R_{\text{EM}} <$	$f_{\text{trk,1}} >$
1-prong	loose	0.09	0.08	0.06
	medium	0.08	0.07	0.12
	tight	0.08	0.05	0.12
multi-prong	loose	0.12	0.15	0.12
	medium	0.08	0.12	0.24
	tight	0.05	0.09	0.32

Table 5.5: The τ_h-ID requirements with average efficiencies for τ_h from simulated Z decays of 60%, 50%, and 30% for *loose*, *medium* and *tight* identification, respectively.

- **Electron veto:** The baseline electron veto method relies on requirements that provide good separation between electrons and hadronic τ candidates [73]:
  - $E^{\text{had}}/p^{\text{track}}$**:** the ratio between the energy deposited in the first layer of the hadronic calorimeter and the leading track momentum,
  - $E^{\text{EM}}/p^{\text{track}}$**:** the ratio between the energy deposited in the electromagnetic calorimeter and the momentum of the leading track,
  - $E^{\text{max}}_{\text{strip}}$**:** the maximum (uncalibrated) energy deposited in the second layer of the electromagnetic calorimeter not associated with the leading track and
  - $N_{\text{HT}}/N_{\text{LT}}$**:** the ratio of high-threshold to low-threshold hits in the Transition Radiation Tracker.

  Based on these variables two flags are provided: medium and tight, corresponding to different levels of electron suppression. The medium flag provides a factor of 50 rejection at the expense of losing about 5% of the reconstructed hadronic τ candidates while the tight criterion enables a suppression of electrons down to the per mille level with 15% loss of signal [73].

- **Muon veto:** One of the main characteristics of muons is the small amount of energy deposited in the calorimeters. The baseline muon veto algorithm rejects events with total energy deposition in the electromagnetic and hadronic calorimeters (at the electromagnetic scale) below 5 GeV [79]. Since the energy threshold for the calorimeter-seeded reconstruction of a τ_h candidate is 10 GeV (at the jet energy scale), this veto is fully efficient for these candidates.

5.4 Hadronic τ reconstruction performance in τ_h+E_T^{miss} events

The first LHC collisions at a center-of-mass energy of $\sqrt{s} = 7\,\text{TeV}$ recorded with the ATLAS detector were used to study the reconstruction and identification algorithms for hadronic τ decays. Although almost no real τ leptons were expected in this dataset, the commissioning of the reconstruction and identification of hadronic τ decays could be studied by measuring properties of selected quark- or gluon-initiated jets and comparing them with predictions from Monte Carlo simulations. This study, documented in [78], was carried out in preparation for the observation of the $W \to \tau_h \nu_\tau$ signal.

5.4.1 Data samples

The studies presented in this section are based on data collected from the first collision run until 24 May 2010, corresponding to an integrated luminosity of $\mathscr{L} = 15.6\,\text{nb}^{-1}$ [42].

Simulated samples

Data are compared with QCD background MC event samples, where the allowed range of the transverse momentum of the outgoing partons in the rest frame of the hard interaction is restricted to be between 8 and 280 GeV. The MC samples are generated with Pythia and passed through the GEANT simulation of the ATLAS detector. In addition to the ATLAS MC09 tune, presented in Chapter 4, the study was repeated using MC samples simulated with the DW tune. The complete list of simulated data sets is shown in Table 4.1.

5.4.2 Event selection

Data quality cuts

Data quality information is assigned to each run at the luminosity block level (small periods of data taking, roughly two minutes long), depending on the LHC machine status, the different sub-detectors' conditions and the quality of the collected data based on basic distributions. All used luminosity blocks are required to have good-quality data for all tracking and calorimeter sub-detectors [81, 82].

Event selection

In addition to the data quality requirement, all events must satisfy the following criteria:

- Trigger: the level-1 trigger requiring a trigger tower jet [83] passing a 5 GeV threshold.
- Event cleaning requirements:

  - There are no misreconstructed jets in the event [82] caused by out-of-time cosmic events or known noise effects in the calorimeters.
  - At least one vertex reconstructed with more than four tracks is present.

- Missing transverse energy of at least 15 GeV is required.
- Events with a τ_{h} candidate with $p_T > 25\,\mathrm{GeV}$. Only the highest-p_T candidate is considered in the analysis. This study was repeated using τ_{h} with $p_T > 20\,\mathrm{GeV}$ in order to be consistent with the τ selection criteria used for $W \to \tau\nu_\tau$ observation (Chapter 7).
- The event is rejected if the selected τ candidate is reconstructed in the pseudorapidity range $1.3 < |\eta| < 1.7$ in order to suppress fake $E_{\mathrm{T}}^{\mathrm{miss}}$ due to τ_{h} energy mismeasurement in the transition region in the ATLAS calorimeter acceptance.

After the complete event selection described above, the number of τ_{h} candidates in MC samples are normalized to the number of τ_{h} candidates selected in data. The shapes of the τ_{h}-ID variables from τ_{h} candidates, reconstructed in a signal $W \to \tau_{\mathrm{h}}\nu_\tau$ MC sample, are also overlaid to show the expectated distributions for true τ leptons.

5.4.3 Distribution of kinematic and identification variables

In order to study the quality of the MC model, a wide variety of data features have been compared with simulation. It includes both discriminating variables used in τ_{h} identification and $W \to \tau_{\mathrm{h}}\nu_\tau$ kinematics. Since the instantaneous luminosities for these datasets are quite low ($< 0.16 \times 10^{30}\,\mathrm{cm}^{-2}\mathrm{s}^{-1}$), the pile-up effects discussed in Section 4.2 are expected to be negligible for the distributions shown here. With higher luminosity, however, pile-up will affect the distributions of these variables for both fake and true τ_{h} candidates, reducing their separation power.

Discriminating variables

Figure 5.2 compares the resulting data and MC-simulated distributions of the three variables used for τ_{h} identification, as discussed in Section 5.3, for τ_{h} candidates with $p_T > 20\,\mathrm{GeV}$ and $p_T > 25\,\mathrm{GeV}$.

There are some small differences between data and QCD background simulation, in particular for the R_{EM} distribution. Nevertheless, the agreement is reasonable at this stage of the ATLAS data-taking phase, and the impact on the separation power of these variables is small. No difference in the distributions due to different p_T thresholds applied to the τ_{h} candidates is observed. Figure 5.3 compares the same variables as in Figure 5.2 but using the DW tune for the QCD background sample. The DW tune models the R_{EM} and the R_{track} variables more accurately than the ATLAS MC09 tune.

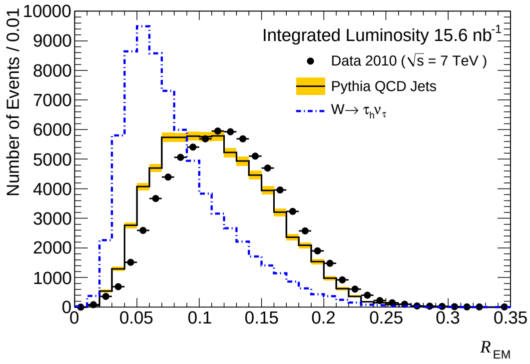

(a) $p_T^{\tau_h} > 20$ GeV.

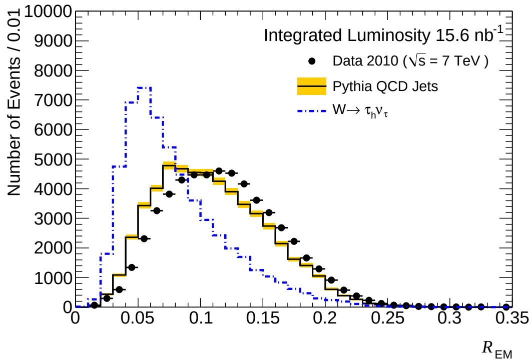

(b) $p_T^{\tau_h} > 25$ GeV.

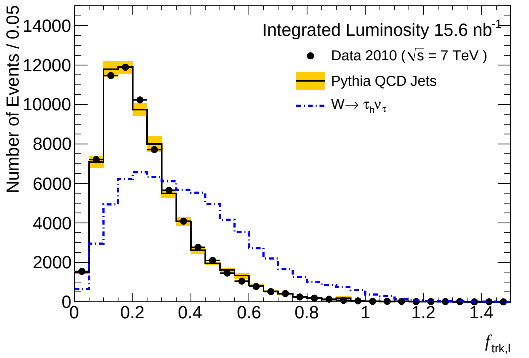

(c) $p_T^{\tau_h} > 20$ GeV.

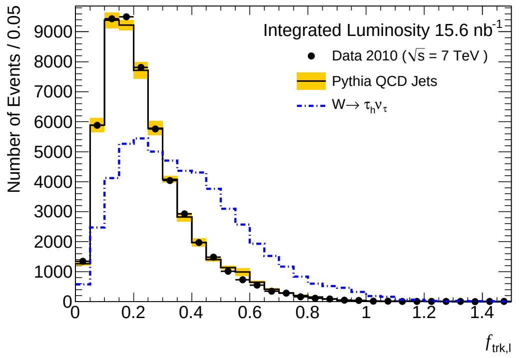

(d) $p_T^{\tau_h} > 25$ GeV.

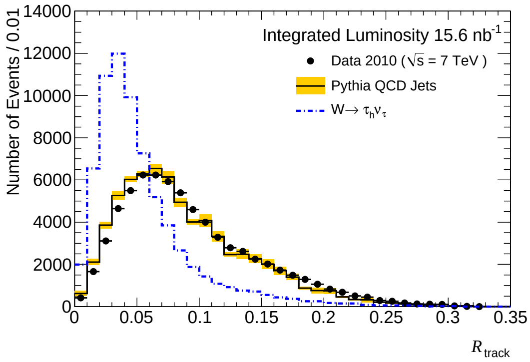

(e) $p_T^{\tau_h} > 20$ GeV.

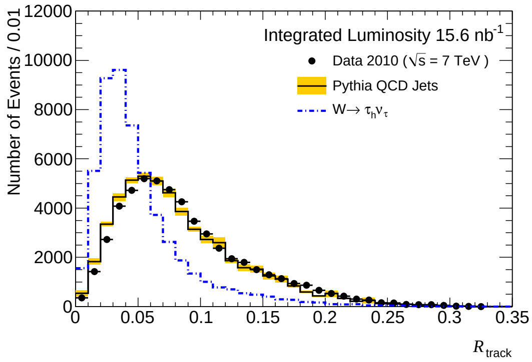

(f) $p_T^{\tau_h} > 25$ GeV.

Figure 5.2: Distributions of (a-b) R_{EM}, (c-d) $f_{trk,l}$ and (e-f) R_{track} for τ_h candidates with $p_T > 20\,\text{GeV}$ and $p_T > 25\,\text{GeV}$. The number of τ_h candidates in MC samples are normalized to the number of τ_h candidates selected in data.

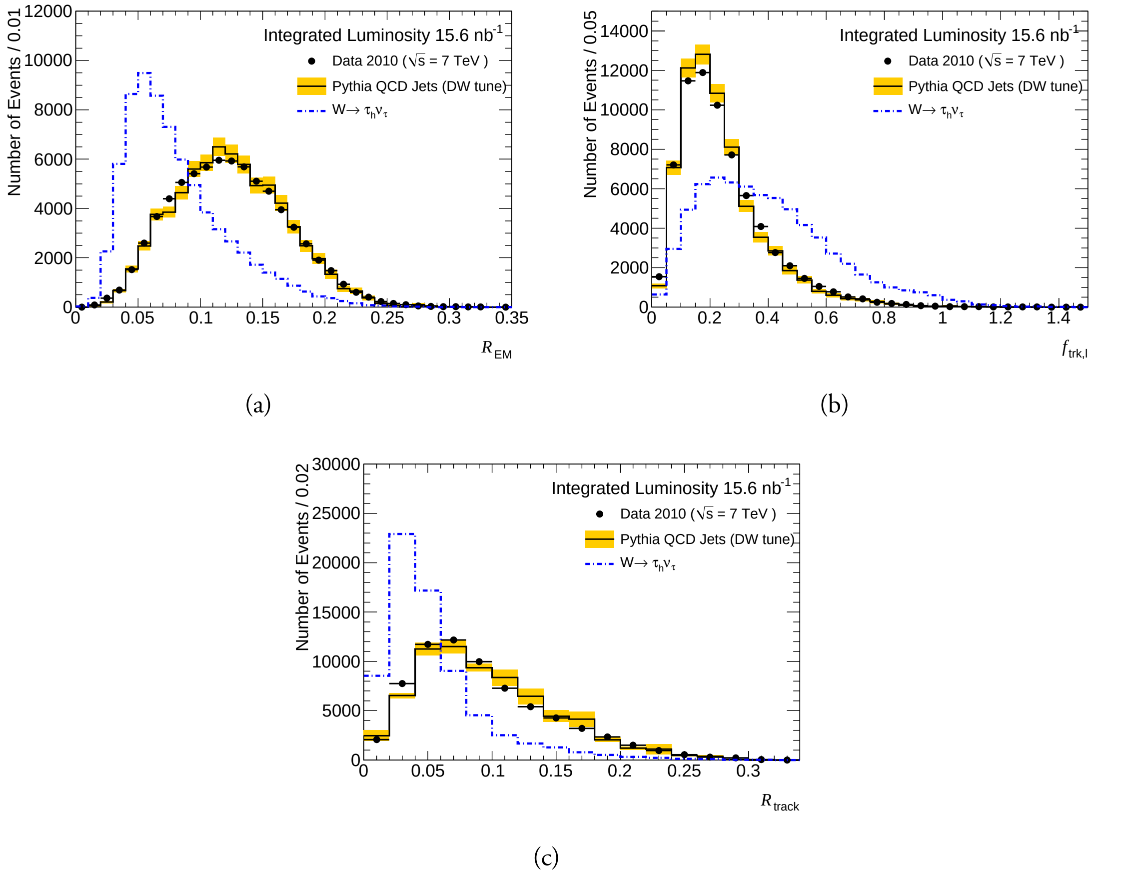

Figure 5.3: Distributions of (a) R_{EM}, (b) $f_{\mathrm{trk,l}}$ and (c) R_{track} for τ_{h} candidates with $p_T > 20\,\mathrm{GeV}$. The QCD background MC samples used the DW tune. The number of τ_{h} candidates in the MC samples are normalized to the number of τ_{h} candidates selected in data.

$W \to \tau_{\mathrm{h}}\nu$ kinematics

The kinematic correlation of the $E_{\mathrm{T}}^{\mathrm{miss}}$ and the τ_{h} object is of particular interest, as these properties will play an important role in selecting a $W \to \tau_{\mathrm{h}}\nu_\tau$ signal. Data-MC comparisons for the differences in azimuthal angle ($\Delta\phi$ between $E_{\mathrm{T}}^{\mathrm{miss}}$ and the τ_{h} candidate) and the transverse mass[2], m_{T}, of the τ_{h} and $E_{\mathrm{T}}^{\mathrm{miss}}$ system are shown in Figure 5.4, for τ_{h} candidates with $p_T > 20\,\mathrm{GeV}$ and $p_T > 25\,\mathrm{GeV}$.

The kinematics of these QCD events are characterized by the presence of fake $E_{\mathrm{T}}^{\mathrm{miss}}$ due to misreconstructed jet energy. In fact, Figure 5.4 shows that $E_{\mathrm{T}}^{\mathrm{miss}}$ points along or opposite to the τ_{h} candidate direction. This information will be used to suppress QCD background in the $W \to \tau_{\mathrm{h}}\nu_\tau$ analysis in Chapter 7. The rate of events with $E_{\mathrm{T}}^{\mathrm{miss}}$ along the τ_{h} candidate

[2]The transverse mass in a $W \to \tau_{\mathrm{h}}\nu_\tau$ decay is defined as $m_{\mathrm{T}} = \sqrt{2 \cdot p_T^{\tau_{\mathrm{h}}} \cdot E_{\mathrm{T}}^{\mathrm{miss}} \cdot \left(1 - \cos\Delta\phi\left(\tau_{\mathrm{h}}, E_{\mathrm{T}}^{\mathrm{miss}}\right)\right)}$.

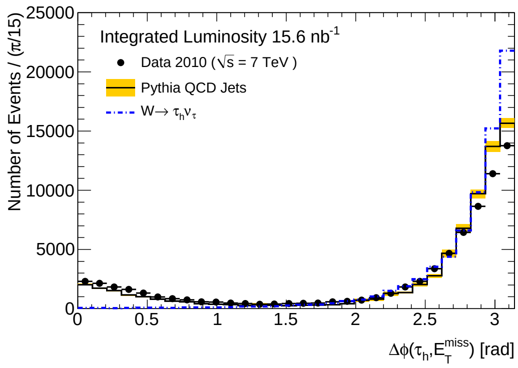

(a) $p_T^{\tau_h} > 20$ GeV.

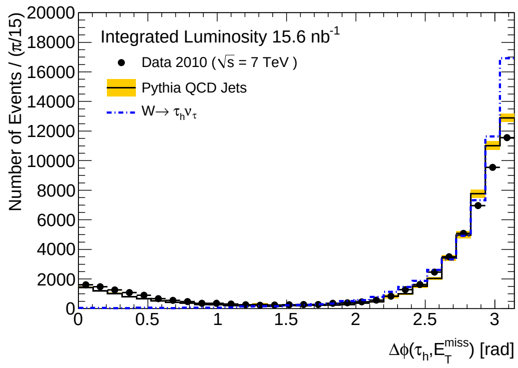

(b) $p_T^{\tau_h} > 25$ GeV.

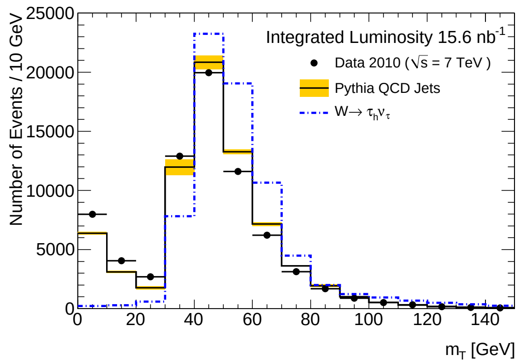

(c) $p_T^{\tau_h} > 20$ GeV.

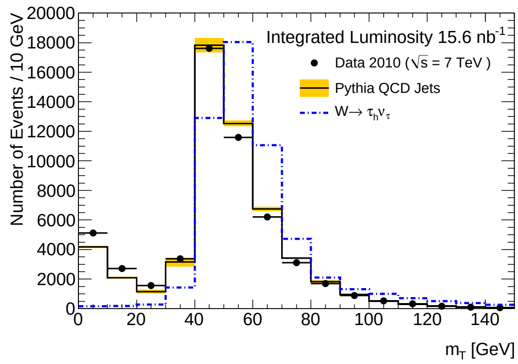

(d) $p_T^{\tau_h} > 25$ GeV.

Figure 5.4: Spatial correlations between τ candidates and $E_{\mathrm{T}}^{\mathrm{miss}}$: (a) and (b) $\Delta\phi$ between $E_{\mathrm{T}}^{\mathrm{miss}}$ and the τ_{h} candidate with $p_T > 20\,\mathrm{GeV}$ and $p_T^{\tau_h} > 25\,\mathrm{GeV}$, respectively; (c) and (d) transverse mass for $p_T^{\tau_h} > 20\,\mathrm{GeV}$ and $p_T^{\tau_h} > 25\,\mathrm{GeV}$, respectively. The number of τ_{h} candidates in MC samples are normalized to the number of τ_{h} candidates selected in data.

direction is higher in data than in MC. While the data-MC agreement is reasonable, small shifts of the simulated distributions with respect to those obtained from the ATLAS data can be seen in Figure 5.4. Also a small effect due to different p_T requirements is observed, with a better agreement for τ_{h} candidates satisfying the $p_T > 25\,\mathrm{GeV}$ requirement. This is due to the small number of simulated QCD background events with low p_T τ_{h} candidates (J0 and J1 samples, corresponding to the transverse momentum of the outgoing partons in the rest frame of the hard interaction to be between 8 and 35 GeV).

Figure 5.5 shows the same distributions as Figure 5.4 for $p_T^{\tau_h} > 20\,\mathrm{GeV}$ but using QCD background MC samples simulated with DW tune. A similar level of agreement is observed but now the rate of events with $E_{\mathrm{T}}^{\mathrm{miss}}$ along the τ_{h} candidate direction is lower in data than in MC.

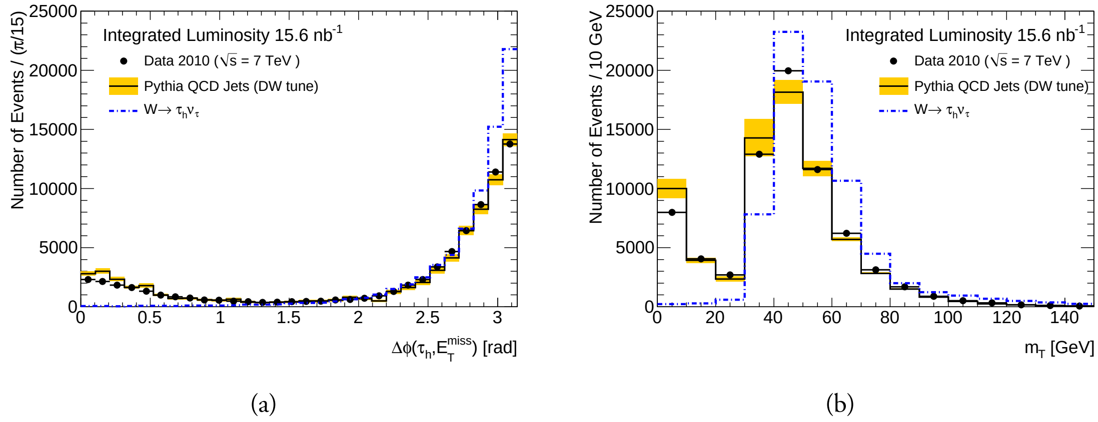

Figure 5.5: Spatial correlations between τ candidates with $p_T > 20\,\text{GeV}$ and $E_{\mathrm{T}}^{\mathrm{miss}}$ using QCD background MC samples with the DW tune: (a) $\Delta\phi$ between $E_{\mathrm{T}}^{\mathrm{miss}}$ and the τ_{h} candidate (b) transverse mass.

In general, a reasonable agreement is observed between data and MC simulated QCD background events, giving confidence in the performance of the algorithms on real τ leptons observed in the $W \to \tau\nu_\tau$ decay process, as will be discussed in the next chapter. The analysis for the $W \to \tau\nu_\tau$ observation will use MC samples with the ATLAS MC09 tune because there were no DW samples including pile-up effects available and also because of missing DW validation by ATLAS for other aspects. The DW tune will then be used in Chapter 9 to estimate the systematic uncertainty due to MC modeling (by comparing the event acceptance for simulated events without pile-up effects).

6. The W $\rightarrow \tau\nu_\tau$ Signal and the Background Processes

The W-boson production processes in proton-proton collisions are discussed in the next section. Section 6.2 describes the characteristic kinematic properties of the $W \rightarrow \tau_\mathrm{h}\nu_\tau$ events and Section 6.3 presents the main background processes for this channel. This information is used in Chapter 7 to efficiently select the $W \rightarrow \tau_\mathrm{h}\nu_\tau$ signal events.

6.1 W boson production at the LHC

The W and Z bosons were discovered in 1983 using the UA1 and UA2 detectors [84–87] which were designed and built for this very purpose. At the LHC proton-proton collider, the cross section for W production is dominated by the leading-order $u\bar{d} \rightarrow W^+$ and $d\bar{u} \rightarrow W^-$ processes. Figure 6.1 illustrates the Feynman diagrams for W production at leading and next-to-leading order.

For the production of the leading-order $u\bar{d} \rightarrow W^+$ ($d\bar{u} \rightarrow W^-$) process, the u (d) quark comes from one proton (valence or sea) and the $\bar{d}$ ($\bar{u}$) quark from gluon splitting in the other proton. Assuming isospin symmetry for sea quark distributions, $\bar{u}$ equal $\bar{d}$, the naive expectation is that $\sigma^{LO}_{W^+}/\sigma^{LO}_{W^-} \approx 2$ in proton-proton collisions, i.e. twice as many W^+ bosons are produced compared with W^- bosons. This asymmetric production in proton-proton collisions is in contrast to proton-antiproton collisions, because the antiproton contains valence anti-quarks. The W production cross section has, however, also some sensitivity to c and s sea quarks. Beyond the leading order Born processes, a W boson can also be produced by $q(\bar{q})g$ interactions, so the parton distribution functions (PDFs) of the proton play an important role at higher orders. Calculations of the total production cross sections for W and Z bosons incorporate parton cross sections, parton distribution functions, higher-order QCD effects and factors for the couplings of the different quarks and anti-quarks to the W and Z bosons. The cross-section values calculated at NNLO are:

$$\sigma^{NNLO}_{W\rightarrow\tau\nu_\tau} = 10.46\,\mathrm{nb} \quad (\sigma^{NNLO}_{W^+\rightarrow\tau^+\nu_\tau} = 6.16\,\mathrm{nb} \quad \text{and} \quad \sigma^{NNLO}_{W^-\rightarrow\tau^-\nu_\tau} = 4.30\,\mathrm{nb}). \tag{6.1}$$

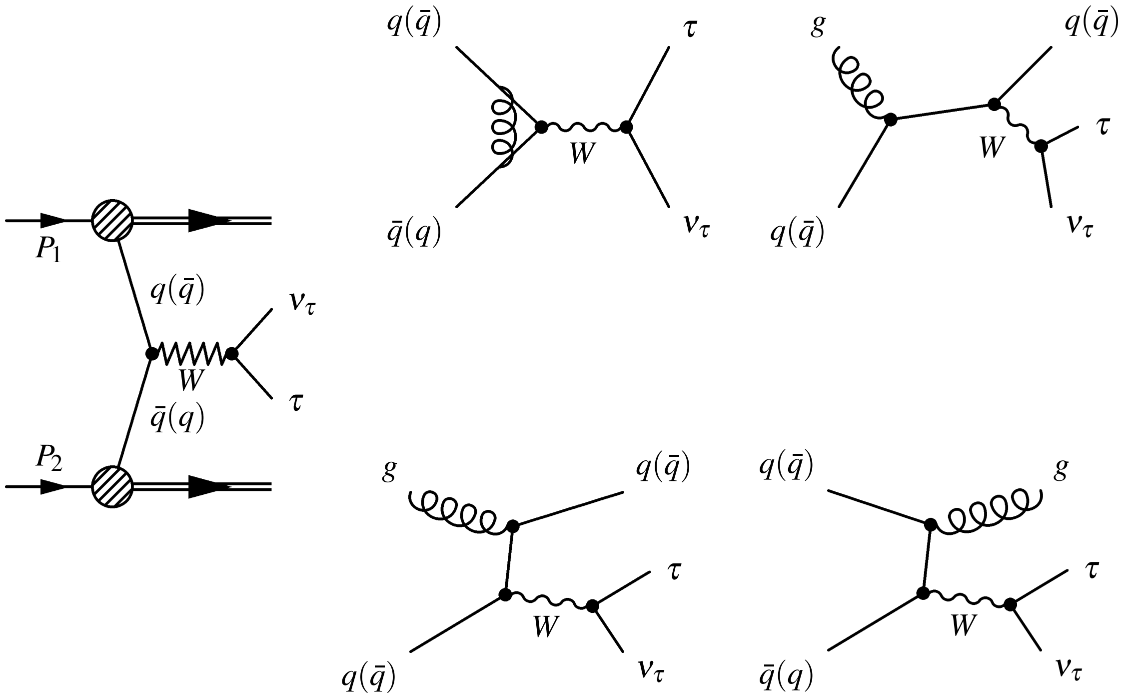

Figure 6.1: Diagrams for production and decay of a W boson at leading (left) and next-to-leading order (others) at a proton-proton collision.

Figure 6.2 shows the total W, Z production cross sections times leptonic branching ratios in $p\bar{p}$ and pp collisions as a function of the collider energy and how the relative contributions of the various $q\bar{q}$ processes to the W production change with collider energy. The collider energy range are split at $\sqrt{s} = 4\,\mathrm{TeV}$, and proton–antiproton collisions are assumed below and proton–proton collisions above this value. For $W^{\pm}$ production (Figure 6.2(b)) the $u\bar{d} \to W^+$ and $d\bar{u} \to W^-$ contributions dominate at all collider energies. These are mostly valence–valence and valence–sea scattering at $p\bar{p}$ and pp colliders, respectively. The next largest contributions come from $c\bar{s} \to W^+$ and $s\bar{c} \to W^-$. Although these are sea–sea processes, they dominate the Cabibbo suppressed $u\bar{s} \to W^+$ valence–sea contributions. The remaining scattering processes contribute between 1% and 3% at the LHC.

Figure 6.3 shows the pp collider energy dependence of the cross section ratio ($R_{\mp} \approx \frac{d\bar{u}}{u\bar{d}}$) and the rapidity distributions of the W^- and W^+ bosons at the LHC. The W^+ bosons tend to be boosted forward compared with W^- bosons because the u quarks carry on average a higher fraction of the proton momentum than d quarks [93].

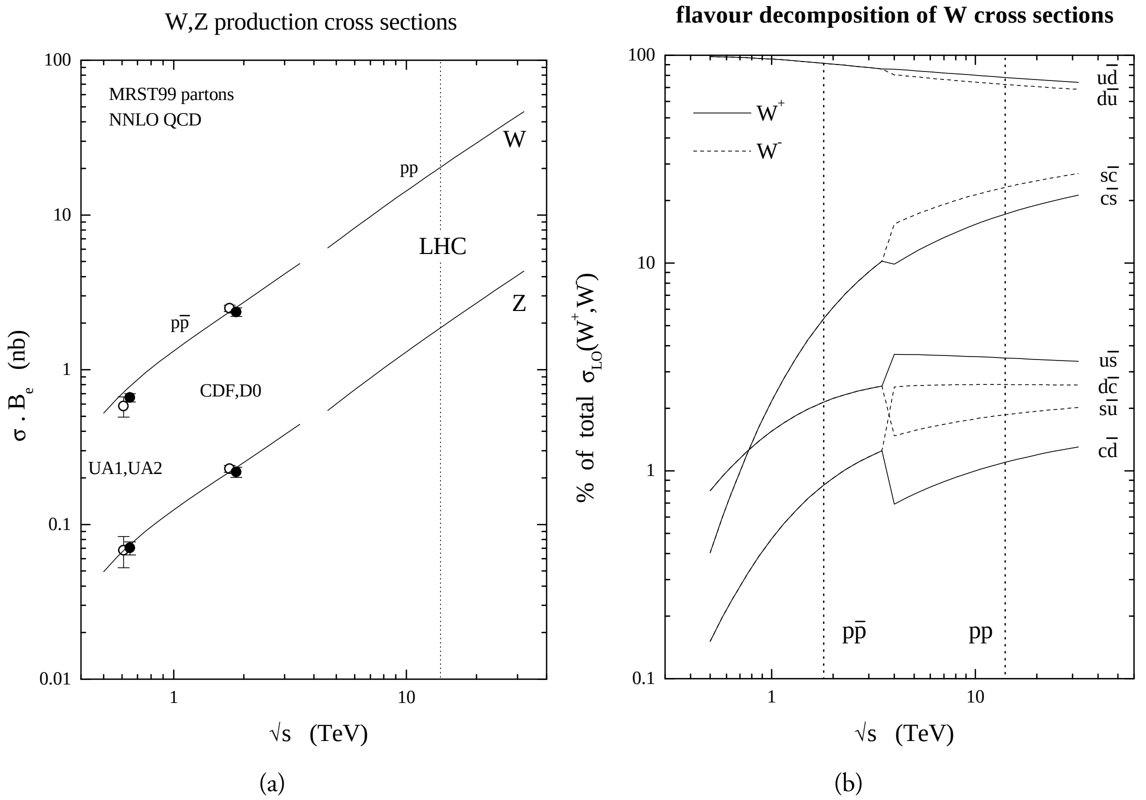

Figure 6.2: (a) Predictions for the total W, Z production cross sections times leptonic branching ratios in $p\bar{p}$ and pp collisions, as a function of the collider energy $\sqrt{s}$ [88]. Experimental measurements from UA1 [89], UA2 [90], CDF [91] and D0 [92] are also shown. (b) Parton decomposition of the W^+ (solid line) and W^- (dashed line) total cross sections in $p\bar{p}$ and pp collisions. Individual contributions are shown as a percentage of the total cross section in each case. In $p\bar{p}$ collisions the cross sections are the same for W^+ and W^- [88].

6.2 Kinematics of W $\to \tau\nu_\tau$ events

Figure 6.4 shows the missing transverse energy and the visible transverse momentum[1] distributions of hadronically decaying τ leptons obtained from generated $q\bar{q} \to W \to \tau_\mathrm{h}\nu_\tau$ events without considering detector-reconstruction effects. Events from $W \to \tau_\mathrm{h}\nu_\tau$ production have predominantly low-p_T W bosons decaying into τ leptons with typical visible transverse momenta between 10 and 40 GeV. In addition, the distribution of the missing transverse energy, associated with the neutrinos from the W and τ_h decays, has a maximum around 20 GeV and a significant tail up to about 80 GeV. Such soft-p_T τ_h and relatively low $E_\mathrm{T}^\mathrm{miss}$ values require

[1]The visible transverse momentum is defined as the vectorial sum of the transverse momenta of the τ decay products except for the neutrinos.

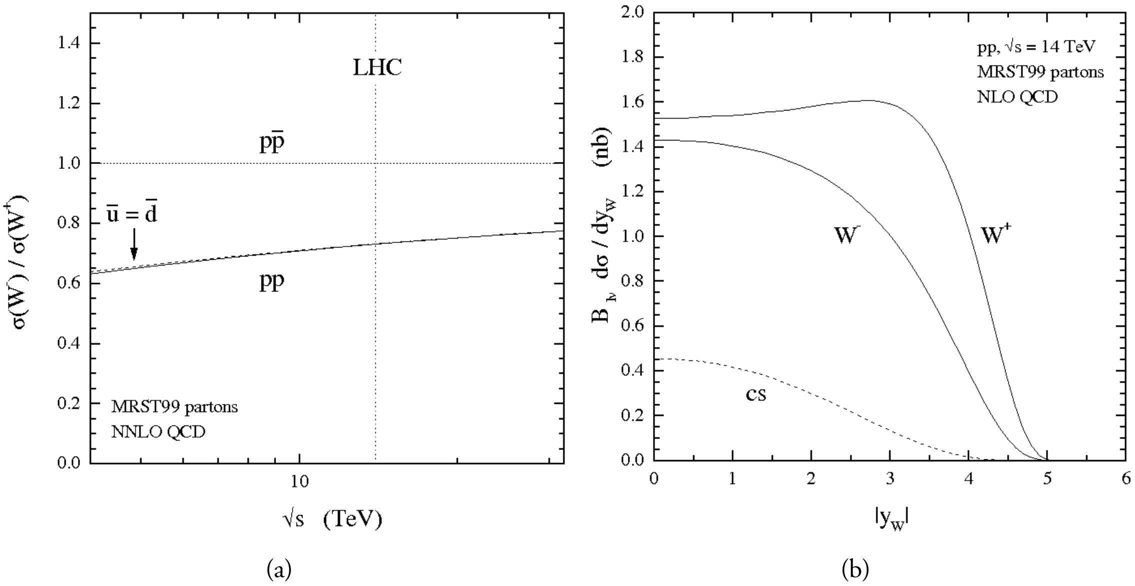

Figure 6.3: (a) Prediction for the ratio $R_{\mp}$ of W^- and W^+ total cross sections in pp collisions, as a function of the collider energy $\sqrt{s}$ [88]. For $p\bar{p}$ collisions the ratio is 1. Also shown (dashed line) is the prediction obtained by setting $\bar{u} = \bar{d}$ in the quark sea. (b) Rapidity distributions of the W^- and W^+ bosons at the LHC. Also shown (dashed line) is the (common) charm–strange scattering contribution [88].

low-threshold triggers, which can only be afforded at the initial data-taking period. When the instantaneous luminosity increases to values above $10^{32}\,\text{cm}^{-2}\text{s}^{-1}$, the trigger thresholds may be too high to efficiently collect $W \to \tau\nu_\tau$ events while keeping the trigger rate within the acceptable bandwidth.

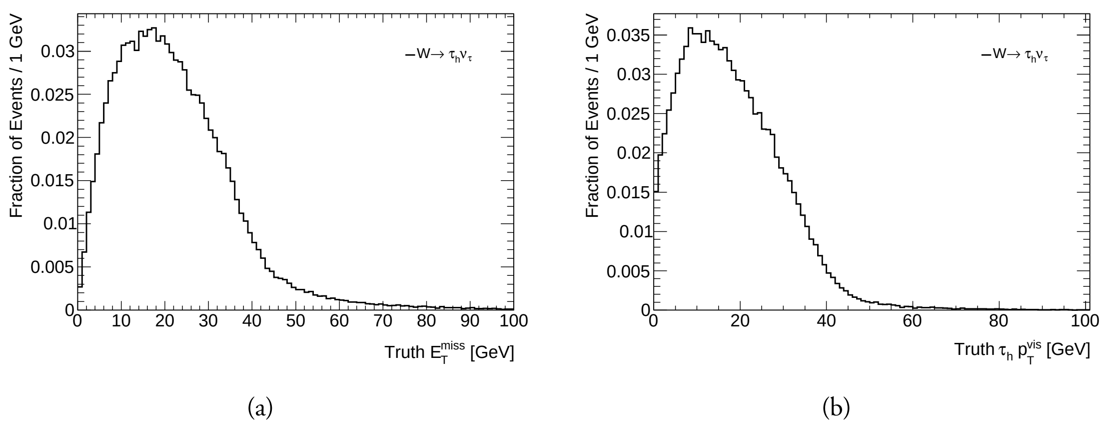

Figure 6.4: (a) Generator-level missing transverse energy and (b) visible transverse momentum of hadronically decaying τ leptons (right) for $W \to \tau_h\nu_\tau$ events.

6.3 Background processes

The following background processes are considered in the $W \to \tau_h\nu_\tau$ analysis (Figure 6.5 illustrates these backgrounds):

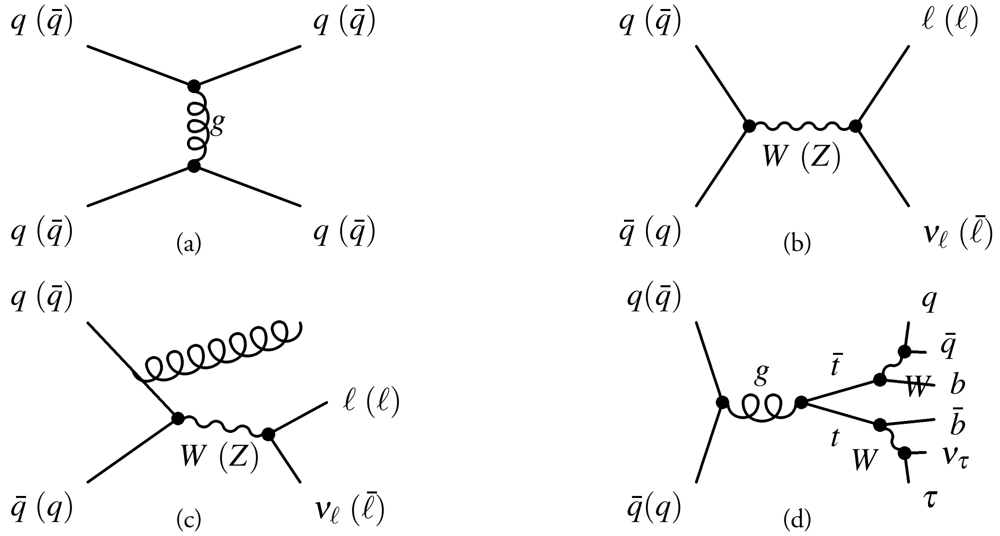

Figure 6.5: Example of Feynman diagrams for the background processes considered in the $W \to \tau_h\nu_\tau$ analysis. (a) QCD di-jet. (b) $W \to \ell\nu$ and $Z \to \ell\ell$. (c) $W \to \ell\nu$ and $Z \to \ell\ell$ with initial-state QCD radiation. (d) $t\bar{t}$.

- QCD multi-jet events
  Misreconstructed QCD events with one jet incorrectly identified as a hadronically decaying τ lepton and a significant amount of missing transverse energy due to jet misreconstruction constitute the dominant background source. The cross section of this process is several orders of magnitude larger than the signal cross section. Thus, a good understanding of this background process and its effective suppression is critical for this analysis.

- $W \to e\nu/\mu\nu$
  These processes contribute to the background if the lepton from the W-boson decay is misidentified as a hadronically decaying τ lepton or if a fake τ_h candidate is reconstructed from initial-state QCD radiation. The first case is strongly suppressed by vetoing events with identified electron or muon. The remaining small fraction of events for which the electron/muon is lost contributes with fake τ_h candidates from initial-state radiation.

- $W \to \tau\nu \to e\nu/\mu\nu$
  Leptonic decay modes of τ leptons are difficult to distinguish from primary electrons and muons. Therefore, similarly to $W \to e\nu$ and $W \to \mu\nu$, this process contributes to the background if the lepton is reconstructed as a hadronically decaying τ lepton. These events can be suppressed by vetoing electrons and muons in the event.

- $Z \to e^+e^-/\mu^+\mu^-$
  Leptonic Z-boson decays contribute if one of the decay electrons/muons is incorrectly reconstructed as a hadronically decaying τ lepton and the other one is lost. As already discussed for the $W \to e\nu/\mu\nu$ processes, this background is strongly suppressed by explicitly vetoing events with identified electrons and muons.

- $Z \to \tau^+\tau^-$
  The rate for this process is about ten times smaller than for the $W \to \tau_\mathrm{h}\nu$ process. It contributes to the background if one of the τ leptons is identified as a hadronically decaying τ lepton while the second one is lost, i.e. neither reconstructed as a second hadronically decaying τ lepton nor as an electron or a muon.

- $t\bar{t}$
  This process contributes to the background if one of the Ws produces a τ lepton in its decay and the other one decays into a pair of quarks, an electron, or a muon which are not reconstructed. Fully hadronic decays can also contribute to the fake τ_h identification. However, this background has a much smaller cross section than the signal process and its contribution was found to be negligible.

The backgrounds from $W \to \tau_\ell\nu$, $W \to e\nu_e$, $W \to \mu\nu_\mu$, $Z \to ee$, $Z \to \mu\mu$ and $Z \to \tau\tau$ are referred to as electroweak (EW) background in this thesis.

7. W $\to \tau\nu_\tau$ Event Selection

The $W \to \tau\nu_\tau$ event selection used in this thesis is based on previous studies [94, 95]. Those studies were performed using simulated data during the preparation of the analysis for the first collisions at the LHC. An improved separation of $W \to \tau_h\nu_\tau$ signal from backgrounds is achieved in the current analysis through an event selection based on the significance of the missing transverse energy, $S_{E_T^{miss}}$, on the new τ_h identification algorithm presented in Chapter 5 and on the development of a method to estimate the QCD background contribution directly from the ATLAS data. In addition, the optimization of the event selection criteria attempts to keep the requirements on the τ_h candidates as loose as possible to allow future τ_h performance studies with the $W \to \tau_h\nu_\tau$ events. This chapter presents the event selection requirements used in this work. The method to estimate the QCD background contribution and its validation is described separately in Chapter 8 and the systematic uncertainties in Chapter 9.

7.1 Data samples

This analysis has been performed on data collected between March and mid-August 2010 by the ATLAS experiment in proton-proton collisions at a center-of-mass energy of 7 TeV. Similarly to the study discussed in Section 5.4, only data taken during periods with stable beams and with a good-quality for all the tracking and calorimeter sub-detectors were used. With these basic data quality criteria, the data set corresponds to an integrated luminosity of 546 nb^{-1}.

7.1.1 Monte Carlo samples

The $W \to \tau_h\nu_\tau$ signal and background MC samples used for this analysis were generated with Pythia for proton-proton collisions at a center-of-mass energy of $\sqrt{s} = 7$ TeV. These MC samples were passed through the GEANT4 simulation of the ATLAS detector and reconstructed as discussed in Chapter 4. The complete MC data sets are shown in Section 4.4. Finally, the simulated events are selected using the same analysis chain as for data, i.e. with the same trigger and event selection criteria described in the following sections.

Simulation of pile-up effects

This analysis is sensitive to multiple interaction effects (pile-up), in particular the $E_{\mathrm{T}}^{\mathrm{miss}}$ and $S_{E_{\mathrm{T}}^{\mathrm{miss}}}$ variables. Figure 7.1 shows the $E_{\mathrm{T}}^{\mathrm{miss}}$ and $\sum E_T$ distributions for data events with 1, 3 and ≥ 5 vertices reconstructed with more than three tracks. The pile-up effect is clearly visible. The $E_{\mathrm{T}}^{\mathrm{miss}}$ distribution is shifted towards higher values for events with additional interactions while the $S_{E_{\mathrm{T}}^{\mathrm{miss}}}$ distribution is shifted towards lower values, due to $\sum E_T$ which is more sensitive to the additional activities in the calorimeters than $E_{\mathrm{T}}^{\mathrm{miss}}$. Therefore, effects of pile-up are included in the simulation of the MC processes used in this study. The simulated events are reweighted so that the distribution of the number of reconstructed primary vertex candidates per event matches the one measured in the ATLAS data. This correction was applied after the trigger and the event cleaning requirements described in Sections 7.2 and 7.3. The average number of vertices per event is 1.7 and the peak instantaneous luminosity amounts to $2.7 \times 10^{30}\,\mathrm{cm}^{-2}\mathrm{s}^{-1}$ in this data set.

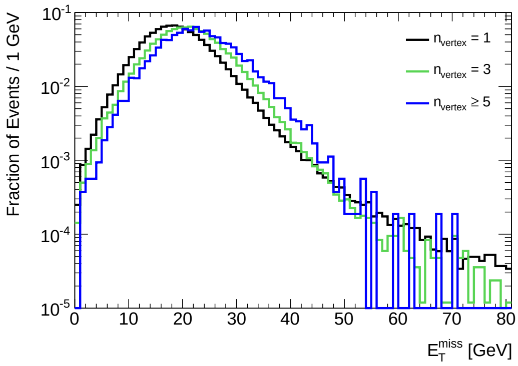

(a)

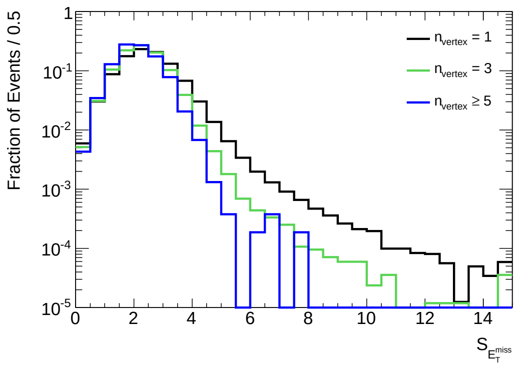

(b)

Figure 7.1: (a) $E_{\mathrm{T}}^{\mathrm{miss}}$ and (b) $S_{E_{\mathrm{T}}^{\mathrm{miss}}}$ distributions for data events with 1, 3 or ≥ 5 reconstructed vertices with at least four tracks.

7.2 Trigger requirements

The trigger requirements [96] are based on the presence of a τ_{h} ($|\eta| < 2.5$) and $E_{\mathrm{T}}^{\mathrm{miss}}$ as main signatures of the $W \to \tau_{\mathrm{h}}\nu_\tau$ decay. These requirements were optimized for different instantaneous luminosity scenarios to provide an efficient trigger for $W \to \tau_{\mathrm{h}}\nu_\tau$ events while keeping the trigger rate within the levels sustainable by the trigger system. Among some trigger configurations available during this early LHC runs, the analysis uses the trigger requirements with the lowest thresholds. The level-1 trigger selects narrow clusters of trigger towers with a p_T threshold of 5 GeV [97]. With the level-2 trigger, tracks are reconstructed around the level-1 τ_{h} candidate. The event is accepted if there is at least one track with $p_T > 6\,\text{GeV}$ and $E_{\mathrm{T}}^{\mathrm{miss}} > 5\,\text{GeV}$. A full event reconstruction is performed at the Event Filter level and the events are required to have $E_{\mathrm{T}}^{\mathrm{miss}} > 15$ GeV. Because the muon trigger is not yet fully validated at both level-2 and EF triggers, the $E_{\mathrm{T}}^{\mathrm{miss}}$ trigger is calculated without applying muon correction [40, 98]. This, however, should not affect the $W \to \tau_{\mathrm{h}}\nu_\tau$ selection since muons are not expected. This trigger requirement has an efficiency of $(99.7 \pm 0.2)\%$, computed from MC simulation, to select $W \to \tau_{\mathrm{h}}\nu_\tau$ events passing the full selection described in this chapter.

Figure 7.2(a) shows the fraction of events passing the level-1 trigger as a function of the momentum of the tight τ_{h} candidate (see Section 5.3 for the definition). This requirement is fully efficient for tight τ_{h} candidates with $p_T > 20\,\text{GeV}$. Figure 7.2(b) shows the acceptance of the full trigger chain as a function of $E_{\mathrm{T}}^{\mathrm{miss}}$. The trigger efficiency reaches its plateau near the threshold of $E_{\mathrm{T}}^{\mathrm{miss}} = 30\,\text{GeV}$ used for the offline event selection (Section 7.4).

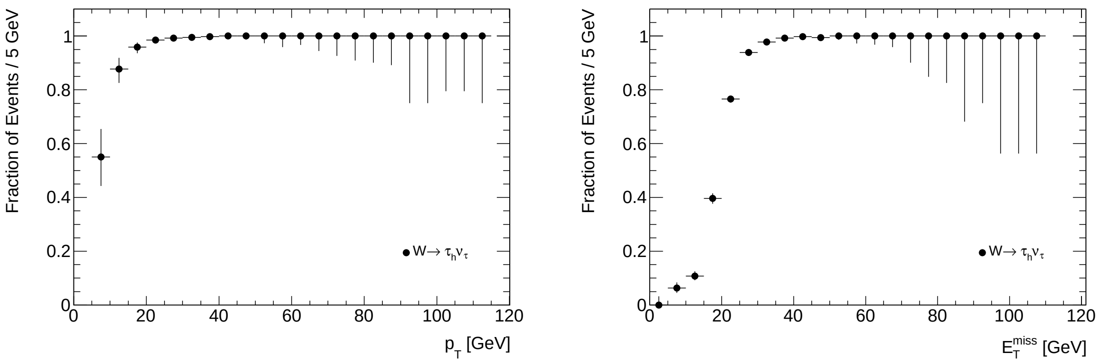

(a) Level-1 trigger ($\tau_{\mathrm{h}} > 5$ GeV).

(b) $\tau_{\mathrm{h}} + E_{\mathrm{T}}^{\mathrm{miss}}$ triggers.

Figure 7.2: (a) Fraction of events passing the level-1 τ_{h} trigger as a function of p_T of the tight τ_{h} candidates (only $W \to \tau_{\mathrm{h}}\nu_\tau$ MC events satisfying all requirements described in this chapter except the $20 < p_T^{\tau_{\mathrm{h}}} < 60\,\text{GeV}$ criterion were considered). (b) Fraction of events passing the full trigger requirements as a function of $E_{\mathrm{T}}^{\mathrm{miss}}$ (only $W \to \tau_{\mathrm{h}}\nu_\tau$ MC events satisfying the offline selection described in this chapter, except for the $E_{\mathrm{T}}^{\mathrm{miss}} > 30\,\text{GeV}$ criterion).

7.3 Event cleaning requirements

In addition to the selection of good-quality data and the trigger requirements described in Section 7.2, further preselection criteria are applied:

- At least one primary vertex reconstructed with at least four tracks (with $p_T > 100\,\text{MeV}$ and $|\eta| < 2.5$) is required in the event.
- Events with misreconstructed jets [82] caused by out-of-time cosmic events or known noise effects in the calorimeters are rejected.

- Events are rejected if a jet with $p_T > 20\,\text{GeV}$ is reconstructed in the pseudo-rapidity range $1.3 < |\eta| < 1.7$, corresponding to a transition region in the ATLAS calorimeter acceptance, in order to suppress fake $E_{\mathrm{T}}^{\mathrm{miss}}$ due to energy mis-measurement in the transition region in the ATLAS calorimeter acceptance. Events are also rejected if $\Delta\phi(\text{jet},E_{\mathrm{T}}^{\mathrm{miss}}) < 0.5$, for jets with $p_T > 20\,\text{GeV}$, to suppress events with misreconstructed jet energy (Figure 7.3). These requirements are referred to as "QCD jets rejection" in Table 7.1.

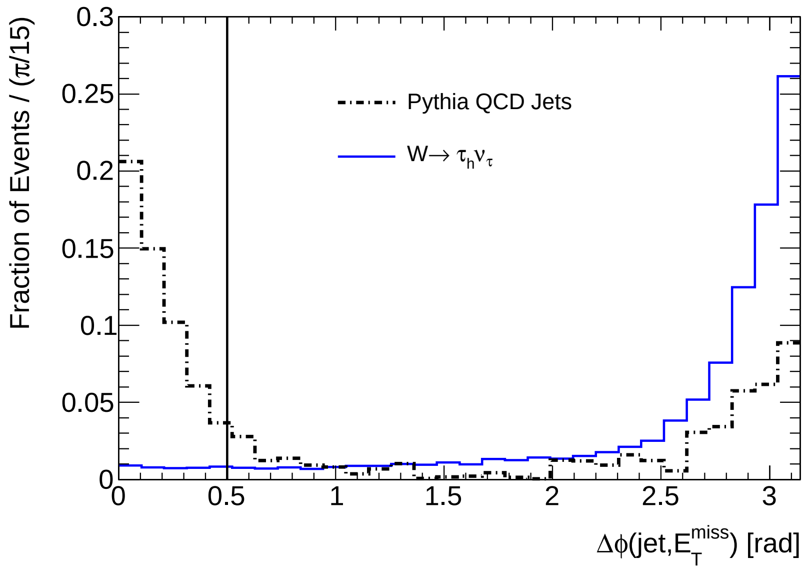

Figure 7.3: Minimum $\Delta\phi(\text{jet},E_{\mathrm{T}}^{\mathrm{miss}})$ distribution for jets with $p_T > 20\,\text{GeV}$ in MC $W \to \tau_{\mathrm{h}}\nu_\tau$ signal and QCD background events with $E_{\mathrm{T}}^{\mathrm{miss}} > 30\,\text{GeV}$. For QCD background, the kinematics of these events is characterized by the presence of fake $E_{\mathrm{T}}^{\mathrm{miss}}$ due to misreconstructed jet energy. Therefore, the p_T imbalance in these di-jet events produce fake $E_{\mathrm{T}}^{\mathrm{miss}}$ in the direction of the lower p_T jet, as illustrated above. This is in contrast to the $W \to \tau_{\mathrm{h}}\nu_\tau$ signal events that have real $E_{\mathrm{T}}^{\mathrm{miss}}$ associated with the neutrinos, in the opposite direction to the τ_{h} jet.

7.4 Missing transverse energy

Missing transverse energy is present in $W \to \tau\nu_\tau$ events because of the neutrinos associated with the W and the τ decays. Therefore, the performance of the $E_{\mathrm{T}}^{\mathrm{miss}}$ reconstruction plays an important role in this analysis. After the event preselection (trigger and event cleaning requirements), a missing transverse energy of $E_{\mathrm{T}}^{\mathrm{miss}} > 30\,\text{GeV}$ is required. Lower thresholds would be affected by the trigger turn-on curve (Figure 7.2(b)) with lower selection efficiency for $W \to \tau_{\mathrm{h}}\nu$ events and a potential source of systematic uncertainty due to eventual differences between data and MC simulation. This requirement suppresses mostly the $W \to e\nu$ and QCD background contributions.

7.5 Selection of hadronic τ decays

The τ_h candidates reconstructed by both the track-seeded and the calorimeter-seeded τ_h reconstruction algorithms and identified as tight τ_h candidates (Chapter 5) are considered. The highest-p_T candidate of these is selected and required to have a visible transverse momentum between 20 and 60 GeV, that is the kinematic range of the signal events (Figure 6.4). Not only the τ_h trigger threshold limits the lower p_T requirement but also the hadronic activity due to the underlying event and multiple proton-proton interactions, in conjunction with the significant amount of inactive material in front of the calorimeter, make it difficult to lower the p_T threshold further. The upper p_T bound for the τ_h candidate is also optimized to suppress the QCD background at higher p_T values. In addition, the event is rejected if the selected τ_h candidate is reconstructed in the pseudo-rapidity range $1.3 < |\eta| < 1.7$, to avoid eventual energy misreconstruction resulting in fake E_T^{miss}.

7.6 Electron and muon veto

Electron and muon vetoes are applied to suppress background events with a real electron or muon. Events with identified *loose* electrons or *combined* muons (described in Section 4.3) with $p_T > 5$ GeV are rejected. Additional suppression of electrons and muons that are misidentified as τ_h candidates, but are not identified by the ATLAS electron and muon identification, is provided by the τ_h-ID algorithm, as discussed in Chapter 5.3. In this analysis the tight electron veto was used to suppress background contribution dominated by $W \to e\nu$ decays.

7.7 Missing transverse energy significance

Finally, the event selection includes a requirement on the significance of the missing transverse energy, defined in Section 4.3.1. Events are rejected if $S_{E_T^{miss}}<6$. This requirement is essential for the rejection of QCD background, for which lower $S_{E_T^{miss}}$ values are expected than for $W \to \tau_h\nu_\tau$ events. This can be observed in Figure 7.4 showing the two-dimensional distribution of E_T^{miss} and $\sqrt{\sum E_T}$ for simulated signal, QCD background and data after the trigger requirement. The criterion on $S_{E_T^{miss}}$ is indicated by a solid line. For a same E_T^{miss} value, QCD events have on average higher $\sum E_T$ values than $W \to \tau_h\nu_\tau$ signal events, due to the characteristic larger hadronic activities in such events.

The discriminating power of $S_{E_T^{miss}}$ is illustrated in Figure 7.5 showing the two-dimensional distribution of $S_{E_T^{miss}}$ and the transverse mass m_T of the τ_h and E_T^{miss} system, after the full event selection. The $S_{E_T^{miss}}>6$ requirement strongly suppresses the QCD background, selecting only the tail of the $S_{E_T^{miss}}$ distribution which is dominated by $W \to \tau_h\nu_\tau$ events, according to MC simulation. The composition of this selected sample is investigated in the next chapter.

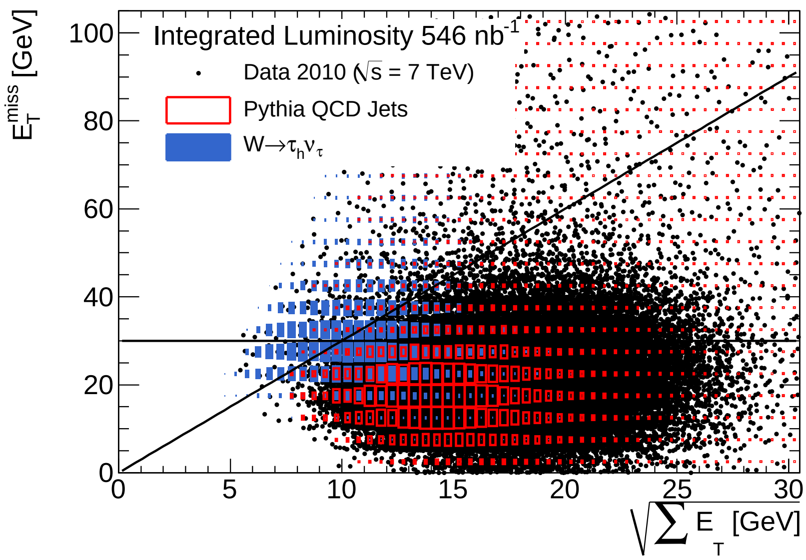

Figure 7.4: Distribution of events in the $E_{\mathrm{T}}^{\mathrm{miss}}$–$\sqrt{\sum E_T}$ plane after the trigger requirement for data, simulated signal events and QCD background. The applied $E_{\mathrm{T}}^{\mathrm{miss}}$ and $S_{E_{\mathrm{T}}^{\mathrm{miss}}}$ criteria are indicated by solid lines.

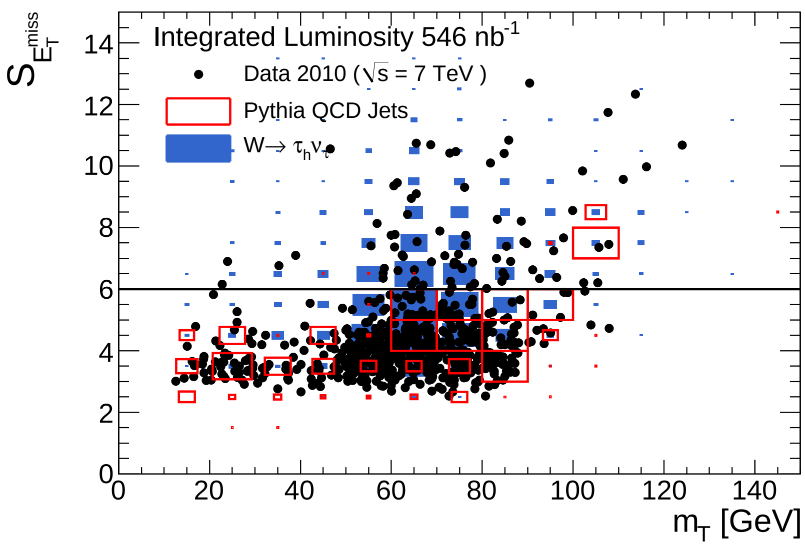

Figure 7.5: Distribution of events in the $S_{E_{\mathrm{T}}^{\mathrm{miss}}}$–$m_{\mathrm{T}}$ plane after the lepton veto requirement for data, simulated signal events and QCD background. The applied $S_{E_{\mathrm{T}}^{\mathrm{miss}}}$ criterion is indicated by a solid line.

7.8 Event selection summary

In summary, the main steps in the selection of $W \to \tau_{had}\nu_\tau$ event candidates are:

- Good-quality data.
- Trigger: a combination of τ_h and E_T^{miss} triggers with 6 GeV and 15 GeV thresholds, respectively.
- Event cleaning requirements.
- Missing transverse energy of at least 30 GeV.
- Select leading-p_T τ_h candidate reconstructed with both track-seeded and calorimeter-seeded algorithms and identified by the tight τ_h-ID algorithm.
- Require the selected τ_h candidate to satisfy $20 < p_T^\tau < 60$ GeV.
- Require the selected τ_h candidate to lie outside the pseudo-rapidity range $1.3 < |\eta| < 1.7$.
- Apply electron and muon vetoes: no electron or muon reconstructed with $p_T > 5$ GeV in the event.
- Missing transverse energy significance: $S_{E_\mathrm{T}^\mathrm{miss}} > 6$.

The selection results in 78 events in data for an integrated luminosity of 546 nb^{-1}. From MC simulation, the expected number of $W \to \tau_\mathrm{h}\nu_\tau$ signal events that pass the selection is 55.3 ± 1.4 events. The background from other W and Z decays is 11.8 ± 0.4 events. The uncertainties correspond to the MC statistical uncertainty. Table 7.1 summarizes the number of data events, simulated $W \to \tau_\mathrm{h}\nu_\tau$ signal and EW background events after each of the requirements described above. An overview of the full selection for QCD background is given in Table 7.2.

The suppression of QCD background is mostly achieved by the event cleaning requirements, that reject events with fake $E_\mathrm{T}^\mathrm{miss}$ (due to energy mismeasurement), and the $S_{E_\mathrm{T}^\mathrm{miss}}$ requirement. The EW background is strongly suppressed by the lepton vetoes. Additional selection criteria exploiting the characteristic properties of $W \to \tau_\mathrm{h}\nu_\tau$ decays further separate the $W \to \tau_\mathrm{h}\nu_\tau$ signal from the backgrounds.

Given the small number of available simulated QCD background events after the full event selection, which is due to the small size of produced MC samples in conjunction with the large rejection factors of the selection criteria and identification algorithms, it is clear that the analysis cannot rely on simulated event samples alone to accurately predict the fraction of QCD processes. Therefore, the QCD background must be estimated from data. This will be described in Chapter 8.

Event selection	Data	$W \to \tau_h \nu_\tau$	$W \to e\nu_e$	$W \to \mu\nu_\mu$	$W \to \tau_\ell \nu_\tau$	$Z \to ee$	$Z \to \mu\mu$	$Z \to \tau\tau$
Trigger	986439	954.5±5.2	3560.7±3.4	521.4±1.6	296.5±2.8	75.3±0.2	59.7±0.2	115.1±0.7
QCD jets rejection	415951	728.3±4.7	2735.3±3.5	400.7±1.5	229.4±2.6	24.5±0.1	45.1±0.1	71.4±0.6
$E_T^{miss} > 30$ GeV	29686	411.5±3.8	1828.3±3.3	317.1±1.3	121.9±1.9	1.13±0.03	34.4±0.1	35.4±0.4
τ_h selection	2408	118.0±2.1	1482.0±3.1	26.6±0.4	34.4±1.0	0.59±0.02	3.24±0.04	11.9±0.3
Lepton rejection	685	94.8±1.9	6.7±0.2	4.9±0.2	2.3±0.3	<0.005	0.11±0.01	4.2±0.2
$S_{E_T^{miss}} > 6$	78	55.3±1.4	4.2±0.2	3.7±0.1	1.8±0.2		0.08±0.01	2.0±0.1

Table 7.1: Number of events passing the selection criteria for data and expected values for MC signal and EW background, normalized to the integrated luminosity of 546 nb^{-1}. When an upper limit is stated, it correspond to 95% C.L. The quoted uncertainties refer to the finite MC statistics only; systematic uncertainties are discussed latter.

Event selection	J0	J1	J2	J3	J4	J5	J6
Trigger	16	1418	41340	273176	627235	917572	1082208
QCD jets rejection	12	937	13112	50031	96314	116397	117289
$E_{\mathrm{T}}^{\mathrm{miss}} > 30\,\mathrm{GeV}$	0	18	364	1353	3859	9246	17461
τ_{h} selection	0	0	22	57	91	184	306
Lepton rejection	0	0	13	37	57	117	167
$S_{E_{\mathrm{T}}^{\mathrm{miss}}} > 6$	0	0	1	2	1	4	3

Table 7.2: Number of MC events passing the selection criteria for simulated QCD background. The different "J" samples are explained in Table 4.1. Numbers refer to MC generated events (not scaled to 546 nb^{-1}).

8. Estimation of Sample Composition

Given the small number of available simulated QCD background events after the full event selection and the large cross section uncertainties for these processes, the analysis presented in the previous chapter could not rely on simulated event samples alone to accurately predict the fraction of QCD processes. Therefore, a method is used to estimate the QCD background contribution directly from data. The method used in this thesis is commonly used in several analyses, for example in [14,99]. To implement the method, however, several studies are needed to find the most appropriate set of independent variables and to validate it. Section 8.1 presents the results of the QCD background estimation and Section 8.2 the validation of these results.

8.1 QCD background estimation from data

The data-driven method is based on the selection of four independent data samples, three in QCD background-dominated regions (control regions) and one in a $W \to \tau_{\mathrm{h}} \nu_\tau$ signal-dominated region (signal region). The samples are selected with criteria on $S_{E_{\mathrm{T}}^{\mathrm{miss}}}$ and on τ_{h}-ID, which are assumed to be uncorrelated[1], after applying the event selection described in Chapter 7. The following four regions are used in this analysis:

- Region A: events with $S_{E_{\mathrm{T}}^{\mathrm{miss}}} > 6$ and τ_{h} candidates satisfying the tight τ_{h}-ID.
- Region B: events with $S_{E_{\mathrm{T}}^{\mathrm{miss}}} < 6$ and τ_{h} candidates satisfying the tight τ_{h}-ID.
- Region C: events with $S_{E_{\mathrm{T}}^{\mathrm{miss}}} > 6$ and τ_{h} candidates satisfying the loose τ_{h}-ID but failing the tight τ_{h}-ID.
- Region D: events with $S_{E_{\mathrm{T}}^{\mathrm{miss}}} < 6$ and τ_{h} candidates satisfying the loose τ_{h}-ID but failing the tight τ_{h}-ID.

[1] In fact, $S_{E_{\mathrm{T}}^{\mathrm{miss}}}$ depends on global event properties and the τ_{h} candidate contributes to its value only through its total p_T, while the τ_{h}-ID is based on shower shape and tracks of the τ_{h} candidate. An indirect correlation may arise due to the dependence of the τ_{h}-ID rejection on the p_T of the τ_{h} candidate [80]. This effect is investigated in Section 9.7, as a source of systematic uncertainty.

Region A is referred to as the signal region and regions B, C and D as control regions. Figure 8.1 illustrates these four regions and Figure 8.2 shows the event distribution in the four regions for data and the expected $W \to \tau_h \nu_\tau$ signal events.

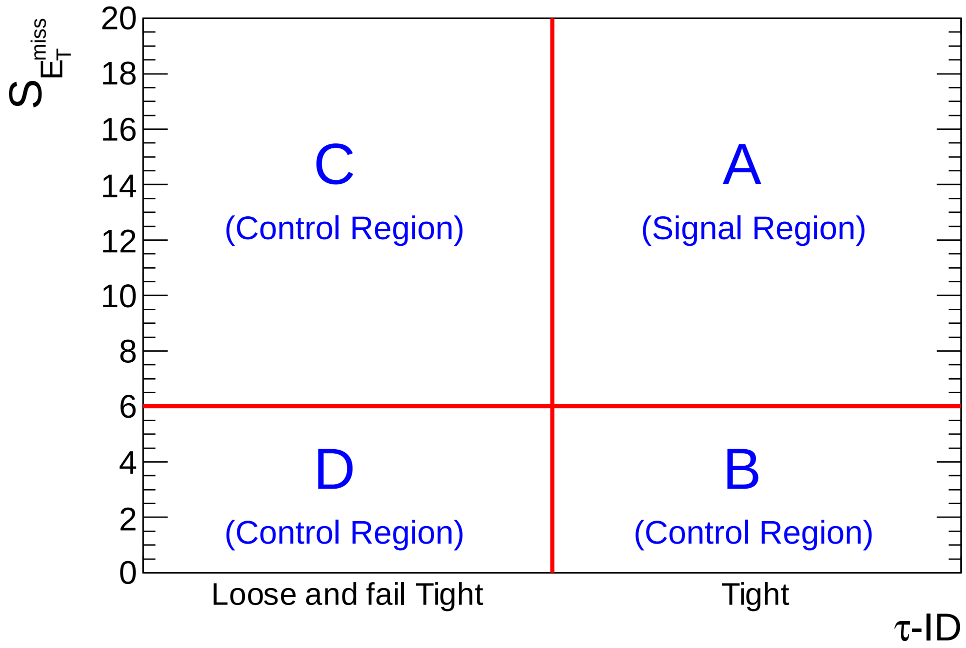

Figure 8.1: Sketch of the four independent regions, three in QCD background-dominated regions (control regions) and one in a signal-dominated region (signal region). The regions are selected with criteria on $S_{E_T^{miss}}$ and on τ_h-ID.

The $S_{E_T^{miss}}$ distribution for QCD background events in the signal region is estimated as follows:

- the shape is determined from the observed events in regions C and D.
- the distribution in region CD is then scaled by the ratio of the number of events in regions B and D.

This prediction is based on two assumptions, namely:

- that the shape of the $S_{E_T^{miss}}$ distribution for QCD background is the same in the combined regions AB and CD;
- and that the contribution of $W \to \tau_h \nu_\tau$ signal and EW background in the three control regions is negligible.

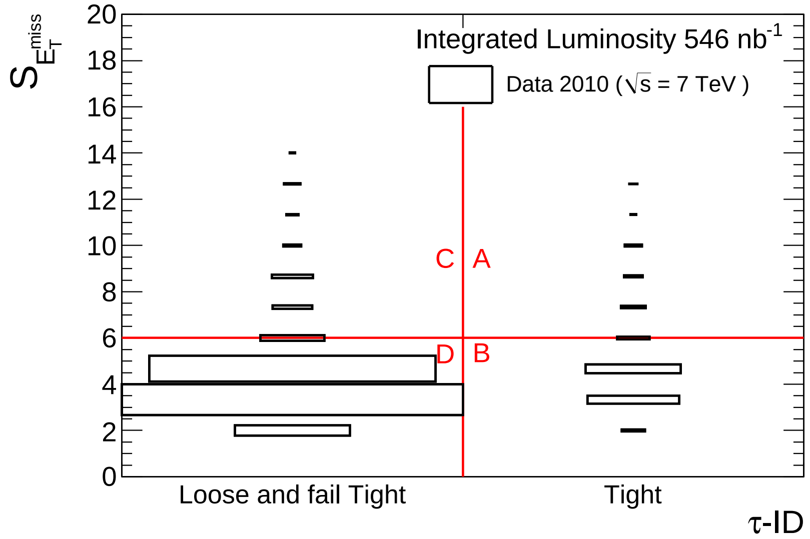

(a)

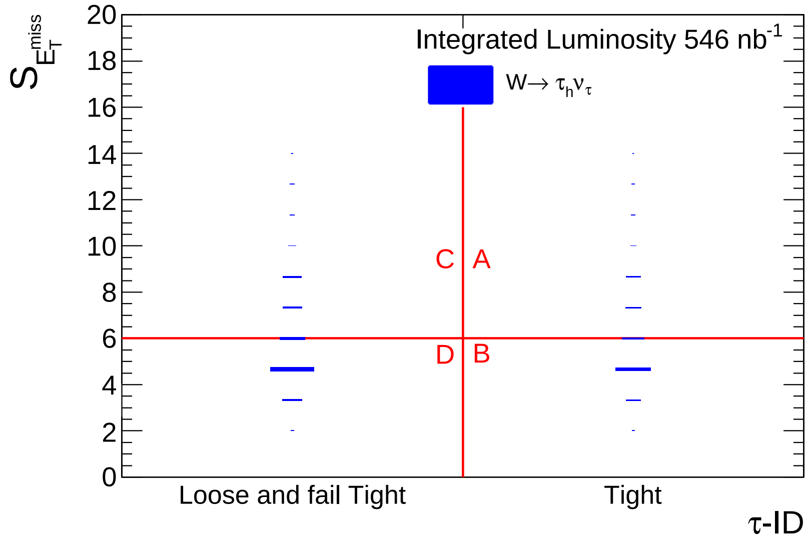

(b)

Figure 8.2: $S_{E_T^{\text{miss}}}$ distribution for events in which the selected τ_h candidate passes the loose but fails the tight τ_h-ID and for events in which the selected τ_h candidate passes the tight τ_h-ID. Distributions are shown for (a) data and (b) $W \to \tau_h \nu_\tau$ simulation after applying the event selection described in Chapter 7, except for the last requirement on $S_{E_T^{\text{miss}}}$. The area of the boxes is proportional to the event yield.

Provided that these two assumptions are satisfied, the method does not rely on any other inputs. The estimate for QCD background in the signal region A, N^A_{QCD}, is then obtained by:

$$N^A_{QCD} = N^B N^C / N^D, \tag{8.1}$$

where N^i represents the number of observed events in region i ($i = B, C, \text{or } D$).

The assumption that the shape of the $S_{E_T^{miss}}$ distribution for QCD background in regions AB and CD is the same has been verified with a data control sample produced by selecting τ_h candidates with more than three tracks ($N_{track} > 3$)[2]. Figure 8.3(a) compares the $S_{E_T^{miss}}$ distribution for events that pass the loose τ_h-ID but fail the tight τ_h-ID with events that pass the tight τ_h-ID, where for both of these samples it is required in addition that the selected τ_h candidates have $N_{track} > 3$. The two distributions agree reasonably well within the statistical uncertainties. To check if these distributions also represent events with selected τ_h candidates with less than four tracks, Figure 8.3(b) compares $S_{E_T^{miss}}$ for τ_h candidates that pass the loose but fail the tight τ_h-ID. A similar level of agreement is observed.

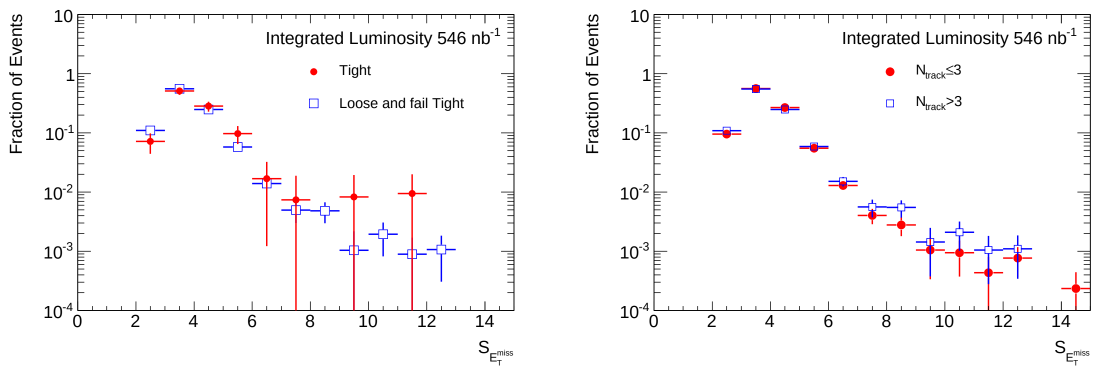

(a) (b)

Figure 8.3: $S_{E_T^{miss}}$ distributions. (a) Distribution for a data control sample of τ_h candidates with $N_{track} > 3$, for τ_h candidates that pass the loose τ_h-ID but fail the tight τ_h-ID and for τ_h candidates that pass the tight τ_h-ID. (b) Distribution for selected τ_h candidates that pass the loose τ_h-ID but fail the tight τ_h-ID for $N_{track} > 3$ and for $N_{track} \leq 3$. The distributions are normalized to unity.

The second assumption, requiring the signal contamination in the control regions to be small, is checked with $W \to \tau_h \nu_\tau$ and EW background MC samples. The fraction of $W \to \tau_h \nu_\tau$ signal events in the control regions is found to be non-negligible, in particular for control region C. This can also be seen in Figure 8.2(b). In addition, the contribution of EW background in the signal region and control regions is significant and needs to be taken into account. Table 8.1

[2] Reconstructed τ_h candidates with large track multiplicities are dominated by misidentified QCD jets.

shows the number of data events and the expected signal and EW background events (N^i_{sig} and N^i_{EW}, respectively) in regions A, B, C and D. The ratios of simulated signal and EW background events in the control regions and the signal region are denoted by the coefficients

$$c_i = \frac{N^i_{sig} + N^i_{EW}}{N^A_{sig} + N^A_{EW}}, \qquad i = B, C, D \tag{8.2}$$

and are summarized in Table 8.1.

Region	A	B	C	D
Data	78	607	254	7107
$W \to \tau_h \nu_\tau$	55.3±1.4	39.5±1.2	71.0±1.6	54.2±1.4
EW	11.8±0.4	6.5±0.2	44.5±0.7	22.1±0.5
c_i		0.69±0.02	1.72±0.05	1.14±0.03

Table 8.1: Number of observed events in the four regions for the data-driven estimation of QCD background. MC estimates of the number of $W \to \tau_h \nu_\tau$ signal and EW background events and the correction coefficients c_i are also shown. The uncertainties are statistical only.

The QCD background determination in the signal region needs to take into account the signal leakage into the background control regions as well as the EW background contamination. Defining $N^A_{non-QCD}$ as the number of non-QCD data events (signal and EW background events) in region A, the corrected number of data events from QCD background in the three control regions (N^B_{corr}, N^C_{corr} and N^D_{corr}) is obtained by subtracting the number of signal and EW background events $c_i N^A_{non-QCD}$ from the observed number of data events in each of the three control regions:

$$N^i_{corr} = N^i - c_i \cdot N^A_{non-QCD}, \qquad i = B, C, D \tag{8.3}$$

Using the relation $N^A = N^A_{non-QCD} + N^A_{QCD}$ and applying the correction above to Equation 8.1 yields

$$N^A_{QCD} = N^B_{corr} N^C_{corr} / N^D_{corr} = (N^B - c_B \cdot (N^A - N^A_{QCD})) \cdot \frac{N^C - c_C \cdot (N^A - N^A_{QCD})}{N^D - c_D \cdot (N^A - N^A_{QCD})}. \tag{8.4}$$

After solving the resulting second-order polynomial equation for N^A_{QCD}, Equation 8.4, the estimated number of QCD events and $W \to \tau_h \nu_\tau$ signal plus the EW events in region A is $N^A_{QCD} = 11.1 \pm 2.3$ and $N^A_{non-QCD} = 66.9 \pm 10.5$, respectively.

The results of the QCD background estimation can be seen in Figure 8.4 for the $S_{E_{\mathrm{T}}^{\mathrm{miss}}}$ distribution and the three variables of the τ_{h}-ID: R_{track}, $f_{\mathrm{trk,1}}$ and R_{EM}. In Figure 8.4(a), the data distribution corresponds to data events in the combined region AB and the QCD background to the combined region CD, after subtraction of EW and $W \rightarrow \tau_{\mathrm{h}}\nu_{\tau}$ signal contributions based on MC simulation. The QCD background is scaled by a factor $(\mathrm{N}^{B} - c_{\mathrm{B}}\mathrm{N}^{\mathrm{A}}_{\mathrm{non-QCD}})/(\mathrm{N}^{D} - c_{\mathrm{D}}\mathrm{N}^{\mathrm{A}}_{\mathrm{non-QCD}})$. Similarly, in Figures 8.4(b), 8.4(c) and 8.4(d), the data distribution corresponds to the combined region AC and the QCD background to the combined region BD, after subtraction of EW and $W \rightarrow \tau_{\mathrm{h}}\nu_{\tau}$ signal contributions. The QCD background is scaled by a factor $(\mathrm{N}^{C} - c_{\mathrm{C}}\mathrm{N}^{\mathrm{A}}_{\mathrm{non-QCD}})/(\mathrm{N}^{D} - c_{\mathrm{D}}\mathrm{N}^{\mathrm{A}}_{\mathrm{non-QCD}})$. In general, a good agreement is observed, with an excess of data that is compatible with the simulated distribution of $W \rightarrow \tau_{\mathrm{h}}\nu_{\tau}$ signal events.

To confirm the $W \rightarrow \tau_{\mathrm{h}}\nu_{\tau}$ signal observation, several control plots were produced comparing distributions for data with the sum of the distributions for the simulated $W \rightarrow \tau_{\mathrm{h}}\nu_{\tau}$ signal and EW background and the estimated QCD background. The distributions of $E_{\mathrm{T}}^{\mathrm{miss}}$ and $\sum E_T$ are shown in Figure 8.5. Here, the data distribution corresponds to the signal region A and the QCD background to the control region C, after subtraction of the EW and signal contributions based on MC simulation. The region C was chosen because the events in this region satisfies the same $E_{\mathrm{T}}^{\mathrm{miss}}$ and $\sum E_T$ requirements as the events in region A. The QCD background is normalized to $\mathrm{N}^{\mathrm{A}}_{\mathrm{QCD}}$.

Figure 8.6 illustrates the p_T and η distributions of the τ_{h} candidates and Figure 8.7 the track multiplicity and electric charge of the τ_{h} candidates. The data distribution corresponds to the signal region A and the QCD background to the control region B, after subtraction of the EW and $W \rightarrow \tau_{\mathrm{h}}\nu_{\tau}$ signal contributions based on MC simulation. Here, control region B was chosen because the τ_{h} candidates in this region pass the same τ_{h}-ID criteria as the τ_{h} candidates in the signal region. Nonetheless, Figures 8.6 and 8.7 show the same distributions using control region C for QCD background, to be consistent with the procedure used in Figure 8.5. In all these figures, the QCD background is normalized to $\mathrm{N}^{\mathrm{A}}_{\mathrm{QCD}}$.

A good agreement is observed between the excess of data and the expected $W \rightarrow \tau_{\mathrm{h}}\nu_{\tau}$ signal in Figures 8.5, 8.6 and 8.7. The track multiplicity distribution for the τ_{h} candidates in Figures 8.7(a) and 8.7(b) is consistent with the characteristic peaks in track multiplicity at one and three, as expected for τ_{h} decays which mostly result in one or three charged particles. The electric charge distribution for the selected τ_{h} candidates is shown in Figures 8.7(c) and 8.7(d). They show a slight, but statistically not yet significant, excess of events with a positive electric charge, as expected in proton-proton collisions and discussed in Chapter 6.

Figure 8.8 shows the distribution for variables combining τ_{h} and $E_{\mathrm{T}}^{\mathrm{miss}}$information, i.e. $\Delta\phi(\tau_{\mathrm{h}}, E_{\mathrm{T}}^{\mathrm{miss}})$ and m_T distributions for data in the signal region and in the different enriched QCD background regions.

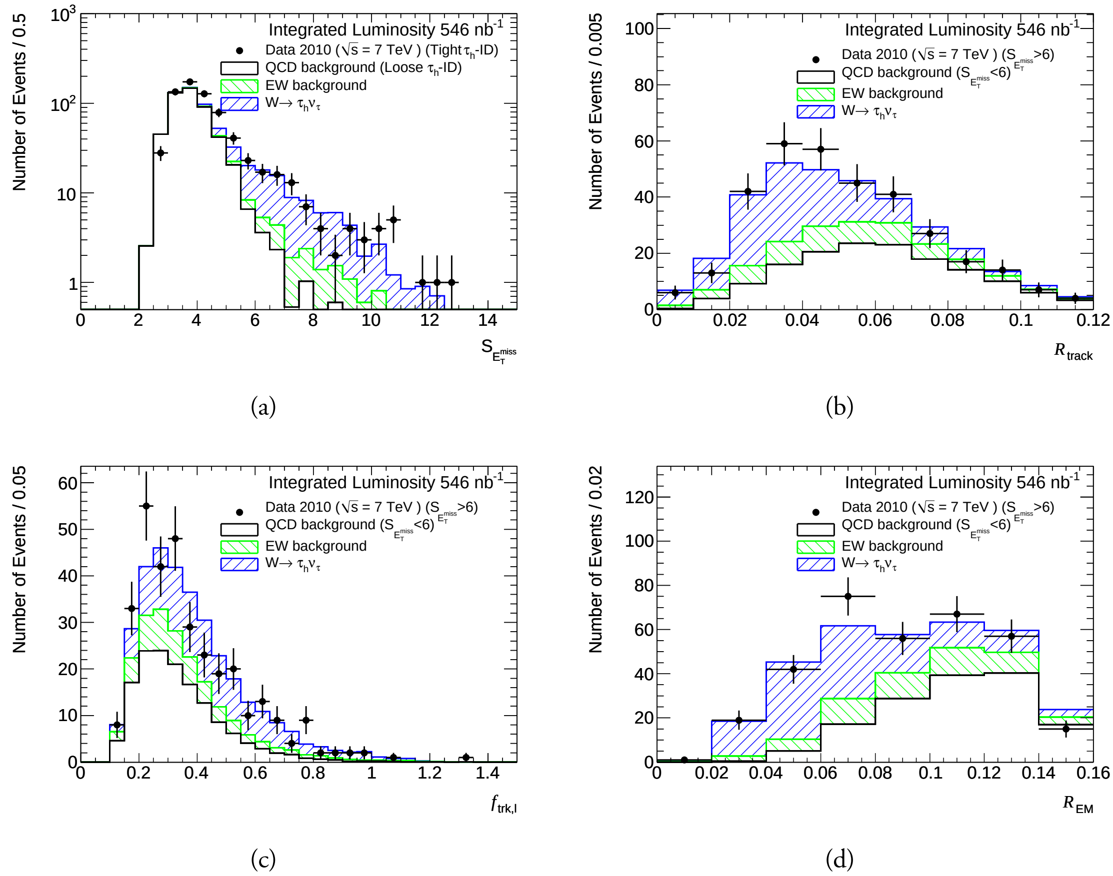

Figure 8.4: (a) Distribution of $S_{E_T^{miss}}$ for data in the combined region AB (tight τ_h-ID region) and the QCD background estimated from the combined control region CD (loose τ_h-ID region), scaled by $(N^B - c_B N^A_{non-QCD})/(N^D - c_D N^A_{non-QCD})$. Also shown are the expected $W \to \tau_h \nu_\tau$ signal and EW backgrounds in region AB from simulated samples. (b), (c) and (d) Distribution of R_{track}, $f_{trk,I}$ and R_{EM} for events in the combined region AC ($S_{E_T^{miss}} > 6$) and for the QCD background estimated from the control region BD ($S_{E_T^{miss}} < 6$) together with the expectations from MC for signal and EW background. The normalization of the QCD background distribution is explained in the text.

In Figure 8.8, clear signatures of $W \to \tau_h \nu_\tau$ decays can be observed, e.g. a large separation in ϕ between τ_h and $E_T^{miss}$and a peak between 60 and 80 GeV in the transverse mass distribution. In particular, Figures 8.8(a) and 8.8(b) present a good agreement between data and the QCD background in the background dominated region (for low $\Delta\phi(\tau_h, E_T^{miss})$ and m_T values), confirming that the control region correctly describes the QCD background contribution.

The good agreement between data in the signal region and the sum of QCD background, EW background and the expected $W \to \tau_h \nu_\tau$ signal in all those control plots presented in this chapter further supports the observation of τ_h leptons from $W \to \tau_h \nu_\tau$ decays in ATLAS.

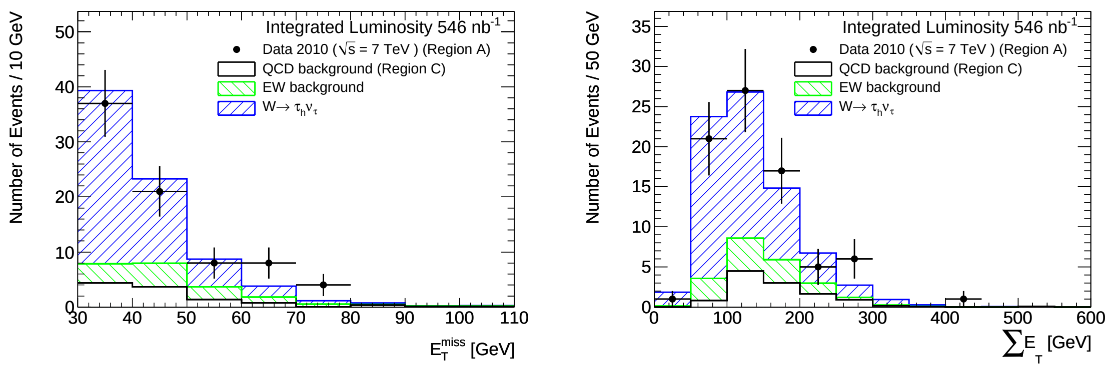

(a) (b)

Figure 8.5: Distributions of $E_{\mathrm{T}}^{\mathrm{miss}}$ and $\sum E_T$ for data in signal region A, the scaled QCD background from control region C, and the contributions from simulated $W \to \tau_{\mathrm{h}} \nu_\tau$ signal and EW background in region A. The QCD background distribution is normalized to the estimated number of QCD background events in region A ($\mathrm{N}_{\mathrm{QCD}}^{\mathrm{A}}$).

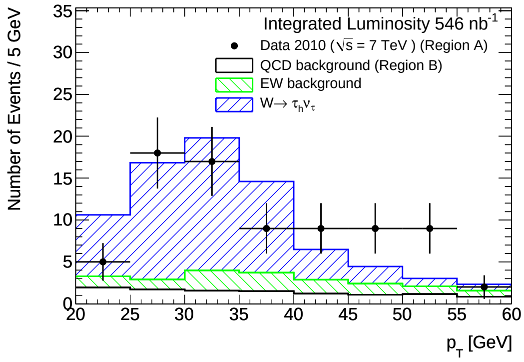

(a) QCD background: region B.

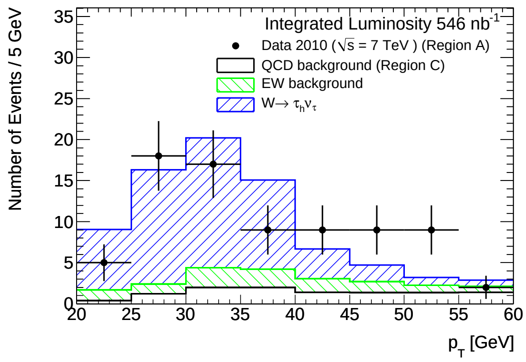

(b) QCD background: region C.

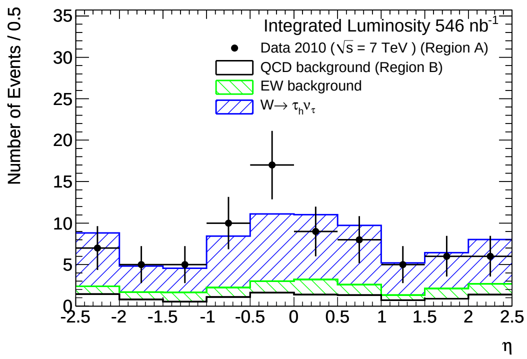

(c) QCD background: region B.

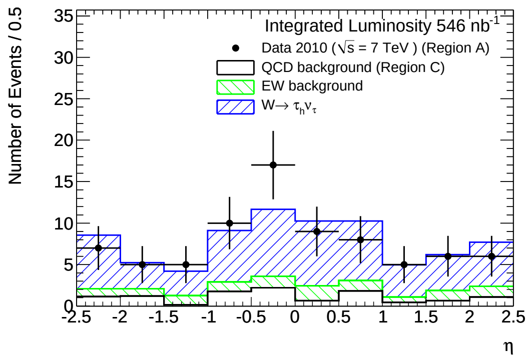

(d) QCD background: region C.

Figure 8.6: (a) and (b) p_T and (c) and (d) η distributions for τ_h candidates for data in signal region A, the scaled QCD background from control region B or C, and the contributions from $W \to \tau_\mathrm{h} \nu_\tau$ signal and EW background in region A. The QCD background distribution is normalized to the estimated number of QCD background events in region A ($\mathrm{N}^{\mathrm{A}}_{\mathrm{QCD}}$).

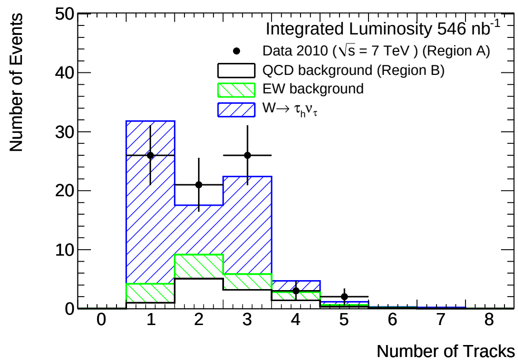

(a) QCD background: region B.

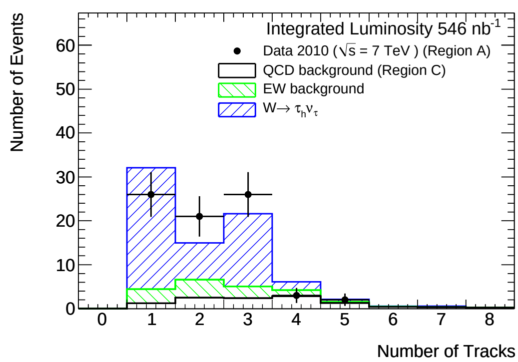

(b) QCD background: region C.

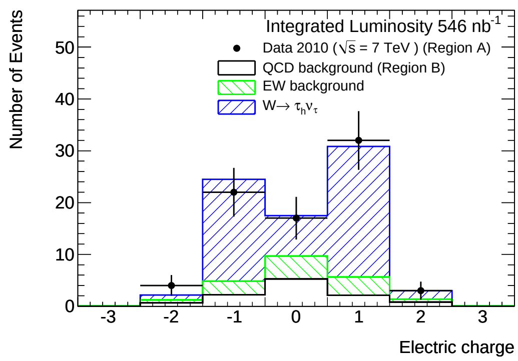

(c) QCD background: region B.

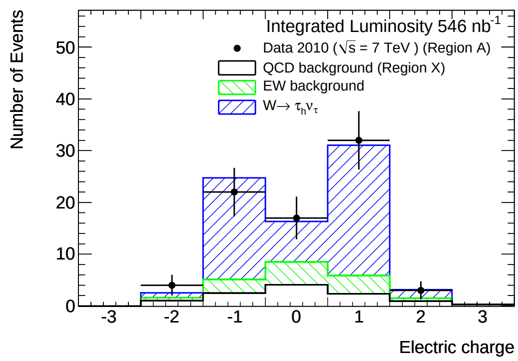

(d) QCD background: region C.

Figure 8.7: (a) and (b) track multiplicity and (c) and (d) electric charge distributions for τ_h candidates for data in signal region A, the scaled QCD background from control region B or C, and the contributions from $W \to \tau_h \nu_\tau$ signal and EW background in region A. The QCD background distribution is normalized to the estimated number of QCD background events in region A (N^A_{QCD}).

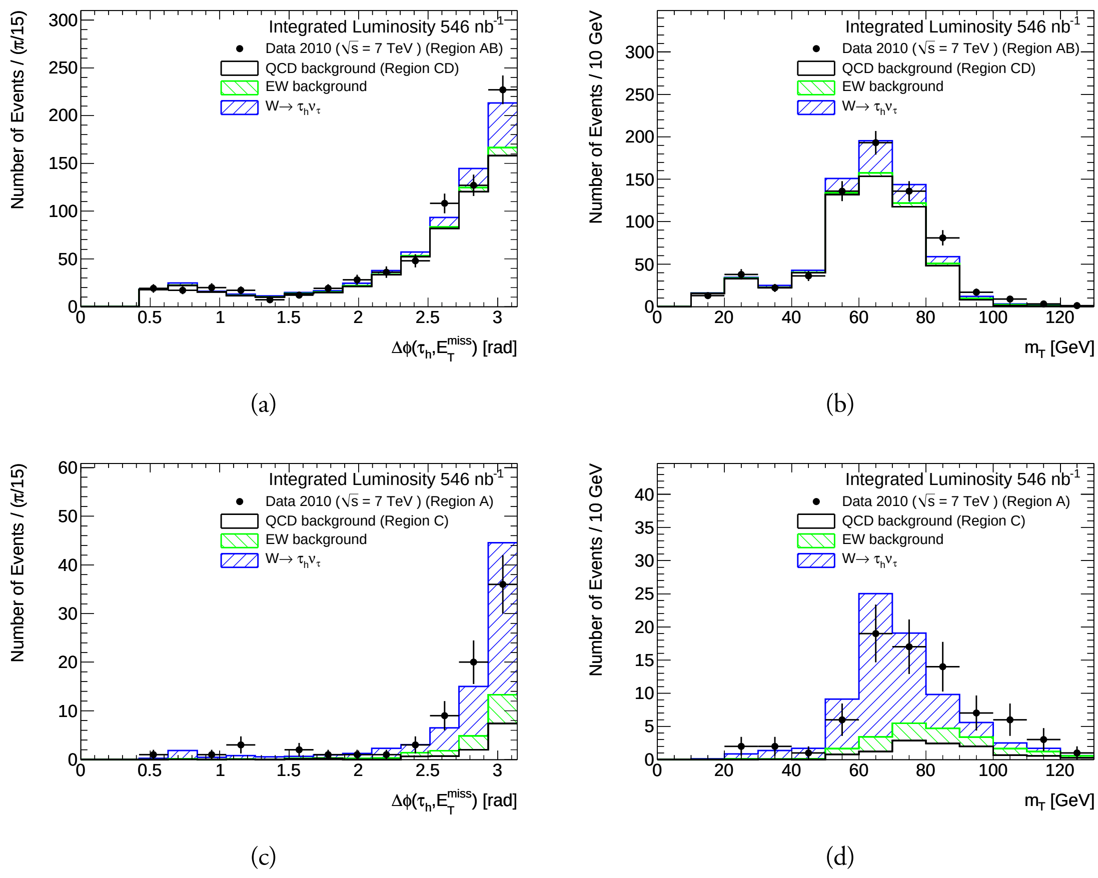

Figure 8.8: Distribution of (a) and (c) $\Delta\phi(\tau_{\mathrm{h}}, E_{\mathrm{T}}^{\mathrm{miss}})$ and (b) and (d) transverse mass m_T for data in the signal region and the QCD background control region, combined with MC $W \to \tau_{\mathrm{h}}\nu_\tau$ signal and EW background. In (a) and (b), the QCD background distribution corresponds to the combined regions CD, scaled by $(\mathrm{N}^B - c_{\mathrm{B}}\mathrm{N}^{\mathrm{A}}_{\mathrm{non-QCD}})/(\mathrm{N}^D - c_{\mathrm{D}}\mathrm{N}^{\mathrm{A}}_{\mathrm{non-QCD}})$ after $W \to \tau_{\mathrm{h}}\nu_\tau$ and EW background subtraction. And in (c) and (d) the QCD background corresponds to region C normalized to $\mathrm{N}^{\mathrm{A}}_{\mathrm{QCD}}$.

8.2 Validation of the data-driven method

The following sections describe several tests performed to confirm that the data-driven method yields consistent results and can be reliably used to estimate the QCD background contribution in the signal region.

8.2.1 Application to a QCD-enriched control sample

The data-driven method cannot be tested with MC samples of QCD background events because of the small number of simulated events passing the event selection. Therefore, the method is tested using a sample enriched by QCD background events in all four regions. The predicted number of QCD background events in the signal region is then compared with the number of events in that region. This QCD background enriched sample was produced by selecting τ_{h} candidates with more than three tracks. The number of selected events in each region is listed in Table 8.2.

	A	B	C	D
Data	5	95	92	2355
$W \to \tau_{\mathrm{h}}\nu_{\tau}$	2.7±0.3	0.7±0.2	11.5±0.7	6.9±0.5
EW	1.8±0.1	0.6±0.1	18.1±0.5	6.9±0.3
c_i		0.29±0.08	6.58±0.56	3.07±0.29

Table 8.2: Number of observed events in the four regions for the data-driven estimation of QCD background for a data control sample of τ_{h} candidates with $\mathrm{N_{track}}$ >3. The MC estimates of the number of $W \to \tau_{\mathrm{h}}\nu_{\tau}$ signal and EW background events for this sample and the correction coefficients c_i are shown.

Using Equation 8.4, the estimated number of QCD background events in signal region A is 3.2±1.1 events. As it can be observed in Table 8.2, the data samples with selected τ_{h} candidates with $\mathrm{N_{track}}$ >3 are quite small and, according to MC simulations, still contain a significant contribution of $W \to \tau_{\mathrm{h}}\nu_{\tau}$ signal and EW background events in the signal region. Nonetheless, the estimated number of QCD background events is in agreement with the observed number of data events which remain after the subtraction of the $W \to \tau_{\mathrm{h}}\nu_{\tau}$ signal and EW background expectations in signal region A. This result indicates that the data-driven method provides consistent values.

8.2.2 Application to subsamples

This validation consisted of applying the data-driven method to complementary subsamples of the selected events and compare the results with the expectations for the full sample. The subsamples were produced based on the following criteria:

- τ_h candidates with transverse momentum between $20\,\text{GeV} < p_T < 30\,\text{GeV}$ or $30\,\text{GeV} < p_T < 60\,\text{GeV}$:
  - the τ_h identification is not uniform as a function of p_T and both E_T^{miss} and $S_{E_T^{miss}}$ are correlated with the p_T of the τ_h candidate. Therefore, the analysis is repeated for two different p_T intervals to verify if the data-driven method provides sensible results in both kinematic regions. The p_T intervals are asymmetric to obtain data samples of approximately the same size for this study.
- τ_h candidates with exactly one track (1-prong) or with more than one track (multi-prong):
  - τ_h candidates with exactly one track (1-prong) or with more than one track (multi-prong) satisfy different τ_h-ID criteria and contain different amounts of QCD background.
- Events with one vertex or more than one vertex:
  - to verify if the data-driven method is sensitive to pile-up effects.

The number of data events and simulated $W \to \tau_h \nu_\tau$ signal and EW background events in signal region A is shown in Table 8.3 for each complementary subsample together with the estimated number of QCD background events in this region. The sum of N^A_{QCD} for each subsample is consistent with 11.1 ± 2.3 estimated with the full sample. Also the observed excess of data events over the total background is in agreement with the expected number of $W \to \tau_h \nu_\tau$ signal events in each subsample. Appendix A shows for each subsample the number of data events and simulated $W \to \tau_h \nu_\tau$ signal and EW background events in all four regions.

Figures 8.9, 8.10, 8.11 and 8.12 show the $S_{E_T^{miss}}$, m_T, R_{track} and the track multiplicity distributions for each subsample. In general, a good agreement is observed, with an excess of data that is compatible with the simulated distribution of $W \to \tau_h \nu_\tau$ signal events.

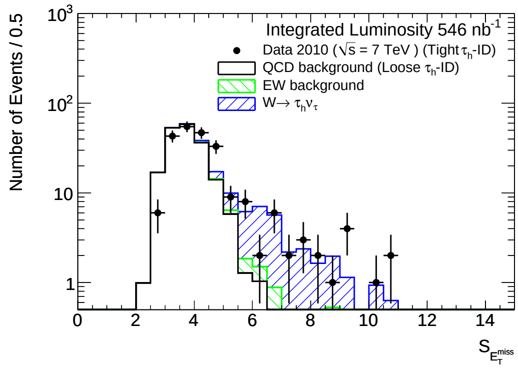

(a) 20 GeV $< p_T^{\tau_h} <$ 30 GeV.

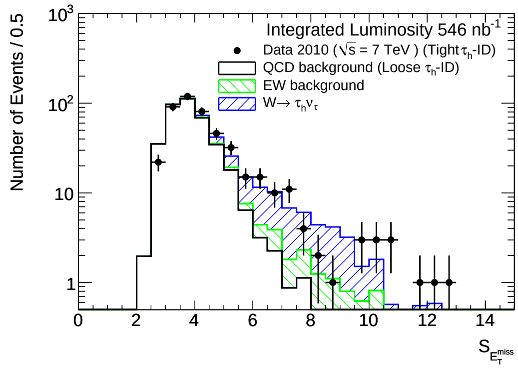

(b) 30 GeV $< p_T^{\tau_h} <$ 60 GeV.

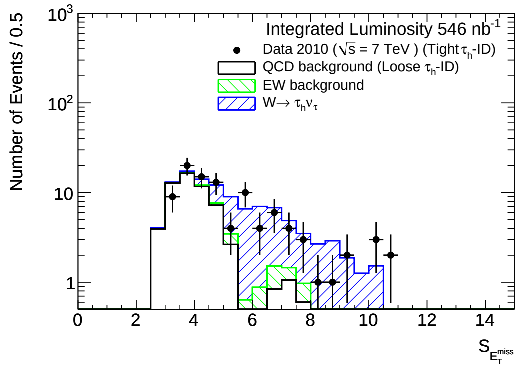

(c) 1-prong τ_h.

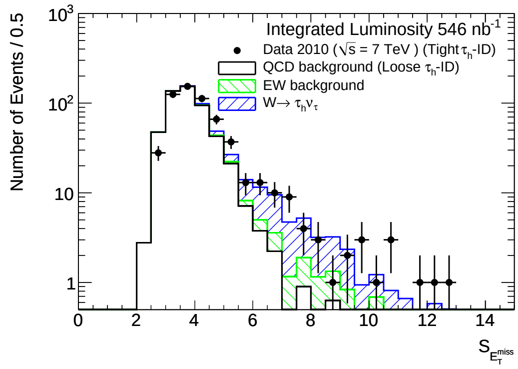

(d) multi-prong τ_h.

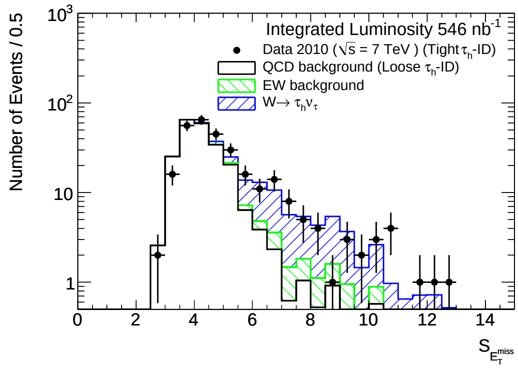

(e) Events with 1 vertex.

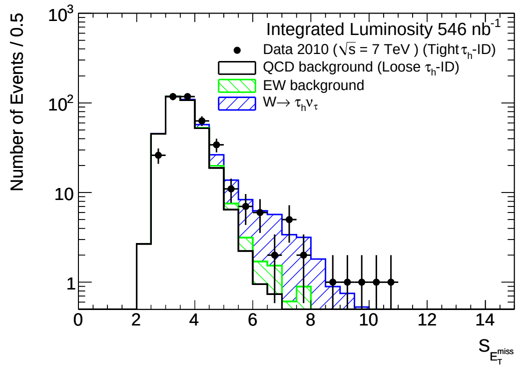

(f) Events with more than 1 vertex.

Figure 8.9: $S_{E_T^{\mathrm{miss}}}$ distribution for several subsamples.

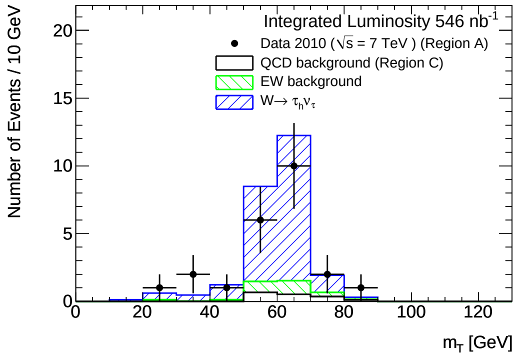

(a) 20 GeV $< p_T^{\tau_h} <$ 30 GeV.

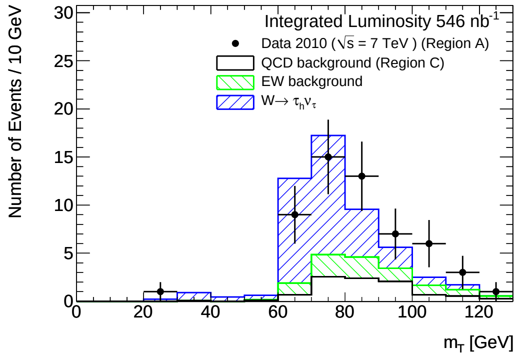

(b) 30 GeV $< p_T^{\tau_h} <$ 60 GeV.

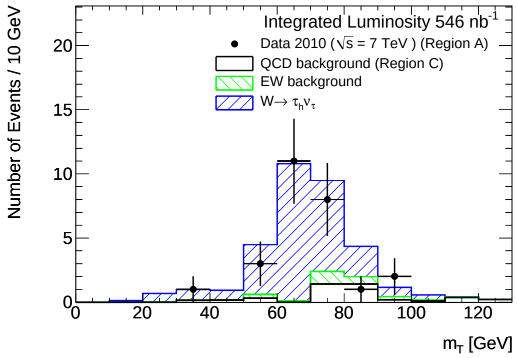

(c) 1-prong τ_h.

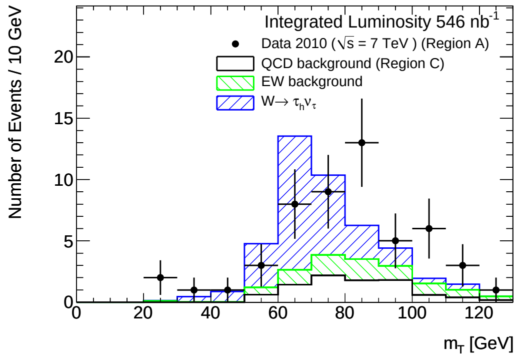

(d) multi-prong τ_h.

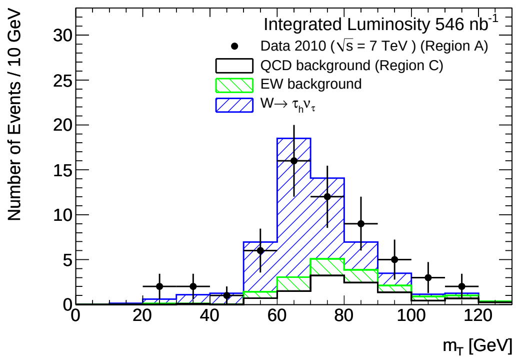

(e) Events with 1 vertex.

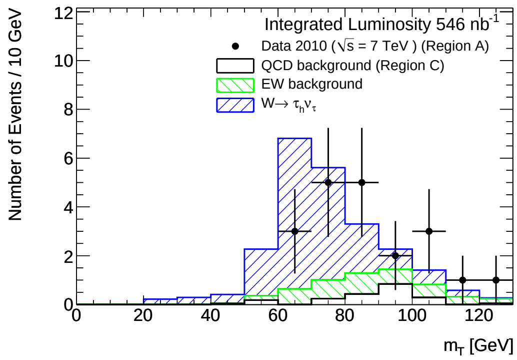

(f) Events with more than 1 vertex.

Figure 8.10: m_T distribution for several subsamples.

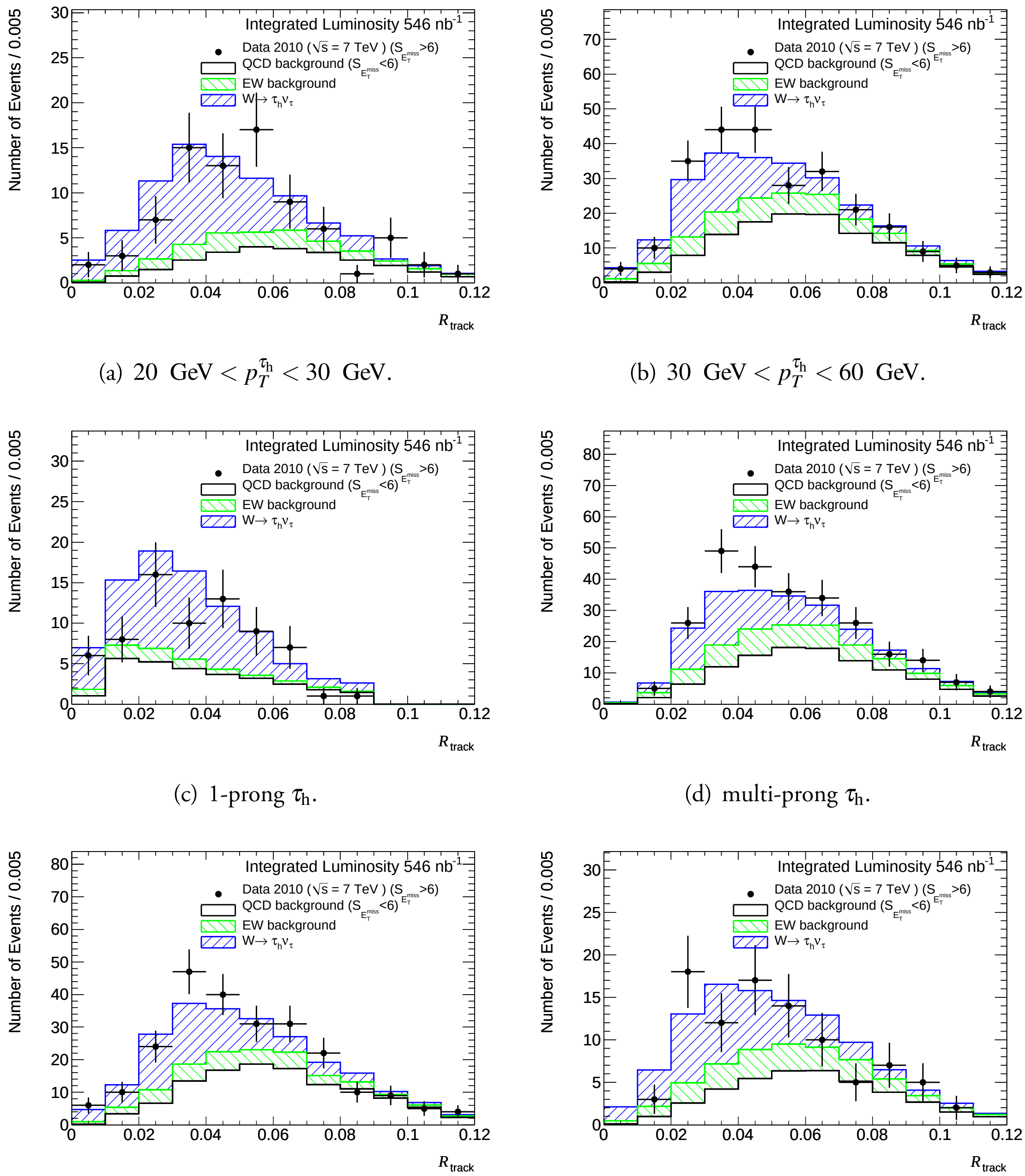

(a) 20 GeV $< p_T^{\tau_h} <$ 30 GeV.

(b) 30 GeV $< p_T^{\tau_h} <$ 60 GeV.

(c) 1-prong τ_h.

(d) multi-prong τ_h.

(e) Events with 1 vertex.

(f) Events with more than 1 vertex.

Figure 8.11: R_{track} distribution for several subsamples.

Subsample	N^A	N^A_{sig}	N^A_{EW}	N^A_{QCD}	N^A_{QCD} Total
$20\,\text{GeV} < p_T^{\tau_h} < 30\,\text{GeV}$	23	21.3±0.9	2.5±0.2	1.9±0.9	11.3±2.3
$30\,\text{GeV} < p_T^{\tau_h} < 60\,\text{GeV}$	55	34.0±1.1	9.2±0.3	9.4±2.1	
1-prong	26	27.6±1.0	3.2±0.2	5.5±2.8	13.3±3.6
multi-prong	52	27.7±1.0	8.5±0.3	7.8±2.2	
1 vertex	58	37.9±1.2	7.5±0.3	10.5 ± 2.5	13.3±2.7
> 1 vertex	20	17.4±0.8	4.2±0.2	2.8±1.1	

Table 8.3: The number of data events and simulated $W \to \tau_h \nu_\tau$ signal and EW background events in signal region A for each subsample and estimated number of QCD background events.

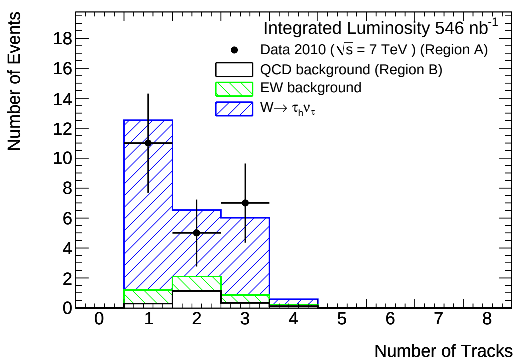

(a) 20 GeV $< p_T^{\tau_h} <$ 30 GeV.

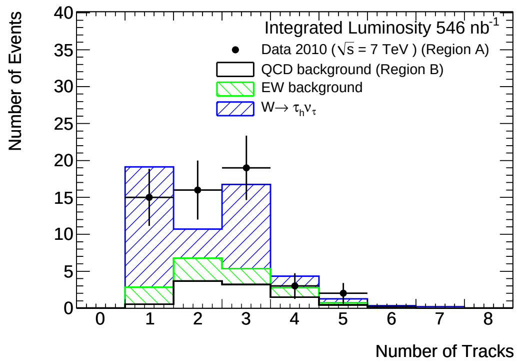

(b) 30 GeV $< p_T^{\tau_h} <$ 60 GeV.

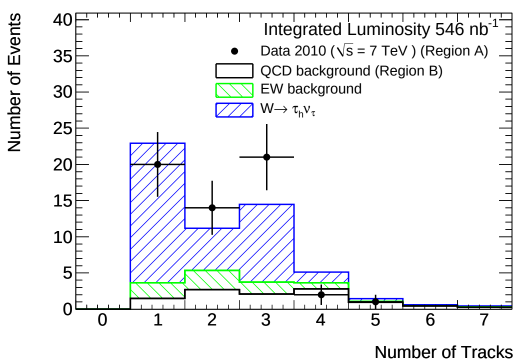

(c) Events with 1 vertex.

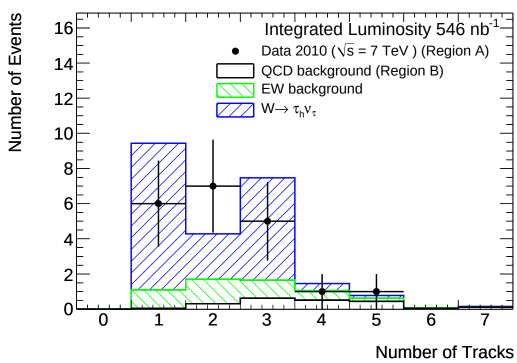

(d) Events with more than 1 vertex.

Figure 8.12: Track multiplicity distribution for τ_h candidates for several subsamples.

8.2.3 Redefining the signal and control regions

Another test consisted of redefining the signal and control regions in the following way:

- Region A: events with $S_{E_T^{miss}}$>8 and τ_h candidates satisfying the tight τ_h-ID.
- Region B: events with $S_{E_T^{miss}}$<6 and τ_h candidates satisfying the tight τ_h-ID.
- Region C: events with $S_{E_T^{miss}}$>8 and τ_h candidates satisfying the loose τ_h-ID but failing the tight τ_h-ID.
- Region D: events with $S_{E_T^{miss}}$<6 and τ_h candidates satisfying the loose τ_h-ID but failing the tight τ_h-ID.

The region 6<$S_{E_T^{miss}}$<8 is not used and the new signal region should contain less QCD background events. The number of events in the new regions are shown in Table 8.4.

	A	B	C	D
Data	25	608	80	7126
$W \to \tau_h \nu_\tau$	18.5±0.8	39.5±1.2	27.2±1.0	54.2±1.4
EW	5.3±0.2	6.5±0.2	22.7±0.5	22.1±0.5
c_i		1.93±0.09	2.10±0.09	3.21±0.13

Table 8.4: Number of observed events and MC expectations in the four regions, excluding the $6 < S_{E_T^{miss}} < 8$ region.

Based on the numbers in Table 8.4 the expected QCD background in the signal region A is 2.7 ± 1.3, in agreement with the observed number of data events which remain when the signal and EW background expectations are subtracted. This indicates again a consistency of the data-driven method.

8.2.4 Event selection with medium τ_h-ID

The number of QCD background is also estimated for a looser τ_h-ID selection, replacing the tight by the medium τ_h-ID requirement. The number of data events in the four defined regions as well as the MC expectations for signal and EW background are listed in Table 8.5. Using Equation 8.4, the number of estimated QCD background in region A is 50.4±11.9.

Also for these events several characteristic variables are investigated. Figure 8.13 shows the $S_{E_T^{miss}}$ distribution, the distribution of the R_{track} τ_h-ID variable, the track multiplicity distribution and the transverse mass for data in the signal region and the estimated QCD background combined with the expected $W \to \tau_h \nu_\tau$ signal and EW contributions, from MC simulation. Additional control plots are shown in Appendix A.4.

	A	B	C	D
Data	197	3109	134	4583
$W \to \tau_h \nu_\tau$	98.7±1.9	75.8±1.7	27.4±1.0	18.0±0.8
EW	32.4±0.6	17.5±0.4	24.2±0.5	11.1±0.4
c_i		0.712±0.018	0.394±0.011	0.222±0.009

Table 8.5: Number of observed events and MC expectations in the four regions for events satisfying the medium τ_h-ID instead of the tight τ_h-ID.

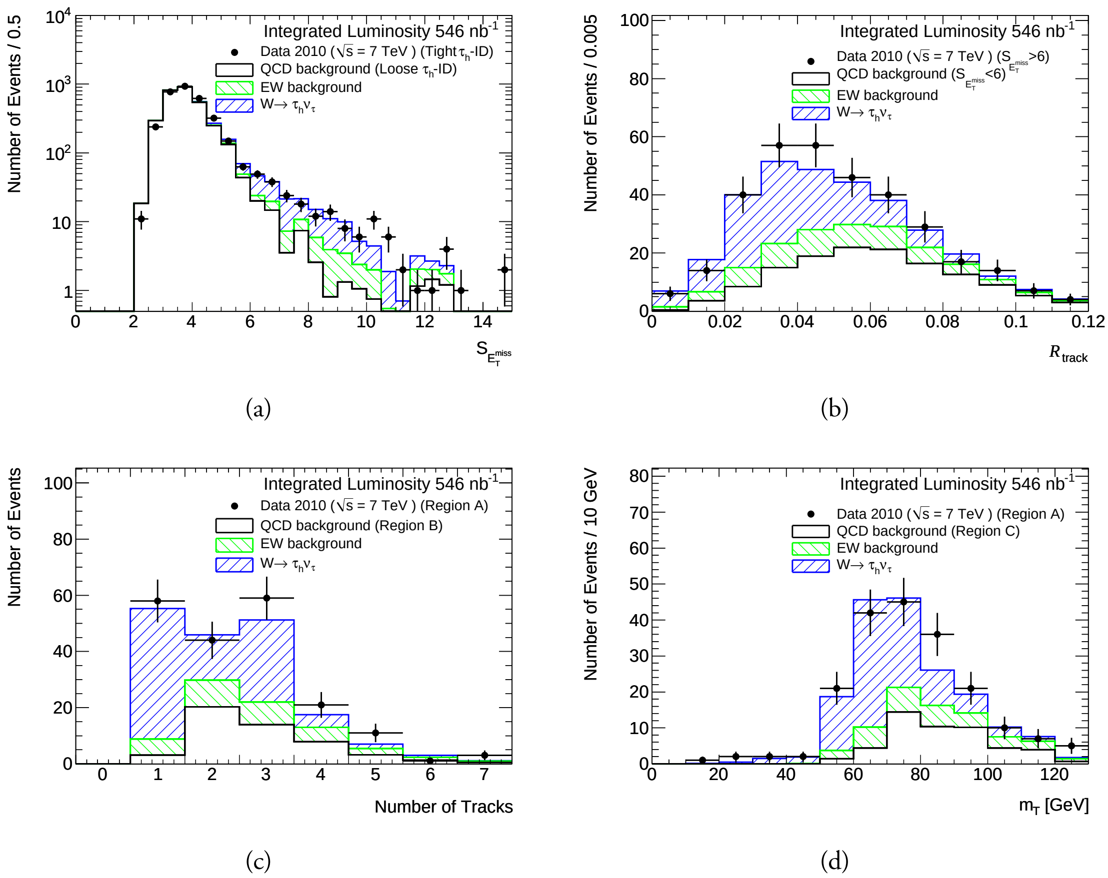

Figure 8.13: (a) $S_{E_T^{miss}}$, (b) R_{track}, (c) track multiplicity and (d) transverse mass distributions for data in the signal region A and the estimated QCD background combined with the expected signal and EW contributions, from MC simulation, for candidates passing the medium τ_h-ID.

The results show again a good agreement among the distributions, indicating a very good reliability of the data-driven method.

8.2.5 Using generic τ_h misidentification probabilities for QCD jets

As a final validation of the data-driven method, an independent method to estimate the number of QCD background events in region A is performed. For this, a data sample is selected as described in Chapter 7 without applying the τ_h-ID requirement for the τ_h candidates. The p_T spectrum of the selected τ_h candidates in this sample is shown in Figure 8.14(a). Using the measured tight τ_h-ID misidentification probability for QCD jets [80], parametrized as a function of p_T (Figure 8.14(b)), the estimated number of events with misidentified τ_h candiates can be directly extracted from Figure 8.14(a). But before, the contribution from $W \to \tau_\mathrm{h}\nu_\tau$ signal and EW background, based on simulation, is subtracted from this selected sample. The estimated number of misidentified τ_h candidates is $6.6\pm1.2_{(\mathrm{stat.})} \pm 1.1_{(\mathrm{syst.})}$ events. The systematic uncertainty includes 9.6% due to energy calibration and 14.5% due to pile-up effects [80]. This number is in fair agreement with the number of expected QCD background events in signal region A of 11.1 ± 2.3 events. This estimate, however, has some caveats, namely: it was not verified if the shape of the p_T spectrum in Figure 8.14(a) represents the correct distribution of the QCD background when the tight τ_h-ID is required; the τ_h misidentification efficiency was measured with a data sample without requiring $E_\mathrm{T}^\mathrm{miss}$ (since $E_\mathrm{T}^\mathrm{miss}$ is due to misreconstructed jets, events with fake $E_\mathrm{T}^\mathrm{miss}$ may have a different τ_h misidentification efficiency values); and the misidentification efficiency should be parametrized in both p_T and η of the τ_h candidates.

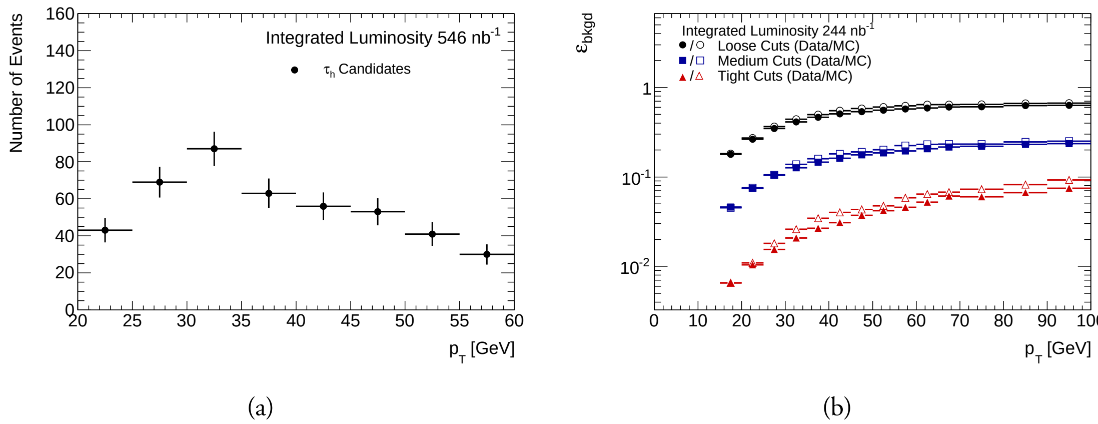

Figure 8.14: (a) Distribution of the transverse momentum of τ_h candidates, without applying the τ_h-ID requirement, for events in the signal region A. (b) τ_h misidentification efficiency for QCD background measured for data and MC samples as a function of the reconstructed p_T [80]. The number of τ_h candidates in (a) is 442 events and the expected number of signal and EW background from MC simulation in this sample are 147 ± 2 and 76 ± 1 events, respectively.

8.2.6 Summary on the validation of the data-driven method

Several independent tests to validate the method to estimate the contribution of QCD background events in the signal region were performed. In all these tests, the data-driven method provided very consistent results, giving further confidence that $W \rightarrow \tau_{\mathrm{h}} \nu_{\tau}$ events are observed in the ATLAS data.

9. Systematic Uncertainties

In Chapter 7, the estimated number of $W \to \tau_h \nu_\tau$ and EW background events in the selected data set, based on Monte Carlo simulation, included only the statistical uncertainty. Similarly, the uncertainty for the estimated number of QCD background events with the data-driven method in Chapter 8 included only the statistical component. Therefore, it is vital to evaluate the systematic uncertainties associated with these numbers for the observation of $W \to \tau_h \nu_\tau$ events in ATLAS.

This chapter presents the evaluation of the systematic uncertainties for various sources of systematic effects. For the numbers estimated with simulated data, the following sources of systematic uncertainties are considered: trigger simulation, lepton veto, energy scale, simulation of pile-up effects, the MC modeling and the cross section and luminosity values. For the estimated number of QCD background events, the systematic uncertainty associated with the data-driven method is evaluated. They are discussed in the next sections.

9.1 Trigger simulation

A suitable data sample containing τ_h candidates and E_T^{miss}, selected by an independent trigger from the one used in this analysis, is not yet available at this early stage of operation of the ATLAS experiment. Therefore, the trigger selection efficiency is evaluated based on MC simulation for events satisfying the full event selection described in Chapter 7. The trigger thresholds were conservatively, and independently, varied by $\pm 50\%$ and the number of selected $W \to \tau_h \nu_\tau$ and EW background events are compared with the number obtained using the original trigger settings. No significant differences are observed due to the fact that the trigger requirements on E_T^{miss} and on the p_T of the τ_h candidate are much softer than those applied in the event selection. Therefore, the systematic uncertainty associated with the trigger efficiency is found to be negligible and it is not considered in this analysis.

9.2 Lepton veto

- **Electron veto:** The veto on electrons is essential for background suppression, in particular for the $W \to e\nu_e$ process since the number of these events passing the τ_h identification criteria is one order of magnitude larger than for $W \to \tau_\mathrm{h}\nu_\tau$ signal, as shown in Table 7.1. The rate of electrons that are misidentified as τ_h is determined by a "tag-and-probe" method applied to $Z \to ee$ events. For this, $Z \to ee$ events are selected and the electron passing good quality criteria is used as a tag while the second electron, satisfying looser criteria, is used to determine the τ_h misidentification rate. This study is performed with data and Monte Carlo simulation and the difference in the results between the two of 30% is used as a conservative systematic uncertainty on the $W \to e\nu_e$ background rate. Taking into account the contribution of the $W \to e\nu_e$ process to the total EW background, this results in an overall uncertainty of 11% on the total number of EW background events.

- **Muon veto:** The background from the $W \to \mu\nu_\mu$ and $Z \to \mu\mu$ processes is suppressed by rejecting events if there is a combined muon reconstructed with $p_T > 5\,\mathrm{GeV}$ in the event. The efficiency of this suppression cannot be verified with the tag-and-probe method for this background, as for the electron veto, because in most cases (83%) the τ_h-candidate is a QCD jet from the underlying event and not a muon from the W or Z decay. In this case, the rate of background events passing the muon veto is proportional to the muon reconstruction inefficiency. This has been assessed for the measurement of the $W \to \ell\nu$ cross section in ATLAS with the standard "tag-and-probe" techniques on the $Z \to \mu\mu$ samples. From a review of the results from different groups [100], the MC estimation of the muon reconstruction efficiency is approximately 92%. Comparison with data shows a dependence of the efficiency on the run conditions and for the run period corresponding to the data sample used in this analysis it is 88%. While data and simulation are compatible within statistical uncertainty, their difference of $8\% \pm 4\%$ has been used as a conservative estimate of the uncertainty on the muon reconstruction inefficiency. This results in a systematic error of 1.9 events over the combined $W \to \mu\nu_\mu$ and $Z \to \mu\mu$ backgrounds and in an overall systematic uncertainty of 16% on the total EW background.

The combination of the uncertainties due to electron and muon rejection leads to a total systematic uncertainty of 19% on the EW background.

9.3 Energy scale

The signal acceptance depends on the energy scale of the topological clusters used in the computation of $E_{\mathrm{T}}^{\mathrm{miss}}$ and $S_{E_{\mathrm{T}}^{\mathrm{miss}}}$ as well as on the p_T of the τ_{h} candidates. Similarly to other studies in [101], the systematic uncertainty associated with the energy scale is obtained by varying the following input parameters in the MC samples and comparing the signal yields with the original settings:

- **Topological cluster energy scale:** The transverse energy originating in W and Z events is mainly deposited in the central region of the calorimeter ($|\eta| < 3.2$). The uncertainty on the cluster energy scale is derived from E/p studies on single hadrons [102, 103] as the difference between data and MC simulation. At the current level of detector calibration in the region $|\eta| < 3.2$, the uncertainty on the energy scale is better than 7% for energetic clusters and at most 20% for p_T of 500 MeV [104]. To evaluate the energy scale uncertainties, $E_{\mathrm{T}}^{\mathrm{miss}}$ and $\sum E_T$ have been recomputed after scaling the topological cluster energies according to a factor $1 + a\left(1 + \frac{N-1}{p_T}\right)$ for values of a and N covering conservatively the above uncertainties [101]. The p_T of the τ_{h} candidate is also scaled according to the energy variation of the topological clusters associated with the reconstructed τ_{h} candidate.

  In the forward region $|\eta| > 3.2$, the energy scale uncertainty is estimated from data to be $\pm 10\%$ [103] and therefore the clusters in the forward calorimeters have been scaled by that amount.

- **$E_{\mathrm{T}}^{\mathrm{miss}}$ resolution:** The resolution on $E_{\mathrm{T}}^{\mathrm{miss}}$ is measured to be $\sigma(E_{x,y}^{\mathrm{miss}}) = 0.49\sqrt{\sum E_T}$ [64] in minimum bias events, but it is slightly degraded when requiring the presence of high-p_T jets [101]. The sensitivity of the simulation to the $E_{\mathrm{T}}^{\mathrm{miss}}$ resolution has been checked by adding a gaussian smearing on the x and y components of $E_{\mathrm{T}}^{\mathrm{miss}}$. An $E_{\mathrm{T}}^{\mathrm{miss}}$ resolution of $\alpha\sqrt{\sum E_T}$ is considered, with $\alpha = 0.65$, which is taken conservatively to cover the uncertainty due to the presence of high-p_T jets. The yield of signal and EW background events is checked against variation of the resolution of $E_{\mathrm{T}}^{\mathrm{miss}}$.

- **Energy reconstruction in the forward calorimeter:** The energy reconstruction in the forward calorimeter (FCal) inner ring cells, $|\eta| > 4.5$, is poorly understood in MC. The impact of cutting this region when computing $E_{\mathrm{T}}^{\mathrm{miss}}$ and $\sum E_T$ is mainly a reduction of $\sum E_T$ and therefore an increase in the acceptance for the $S_{E_{\mathrm{T}}^{\mathrm{miss}}}$ selection.

The results of the energy scale systematic studies are summarized in Table 9.1 for $W \to \tau_{\mathrm{h}}\nu_\tau$ signal and the main EW background contributions. The acceptances for $W \to \tau_{\mathrm{h}}\nu_\tau$ signal and electroweak background changed by $\pm 21\%$ and $\pm 14\%$, respectively (since the upper and lower variations are very similar, it is preferred to quote symmetric uncertainties on the acceptances for $W \to \tau_h \nu_\tau$ signal and EW background).

9.4 Simulation of pile-up effects

The instantaneous luminosity at the LHC continuously decreases during the data-taking run. And each run has different instantaneous luminosity. Therefore, the variation of the beam conditions at the LHC results in different amount of pile-up effects and it needs to be taken into account in the simulation. Since the number of reconstructed primary vertex candidates per event is related to the pile-up activity, the pile-up effect has been accounted for by reweighting the simulated events so that the distribution of the number of reconstructed primary vertex candidates per event matches the one measured in the ATLAS data. The systematic uncertainty associated with this procedure is evaluated by varying the event weights within their statistical uncertainties. It is found to be 1% for MC $W \to \tau_h \nu_\tau$ signal events and 0.2% for EW background samples.

9.5 Monte Carlo model

The systematic uncertainty associated with the Monte Carlo simulation is evaluated by the difference in number of simulated events passing the full selection for the two different underlying event models, ATLAS MC09 and DW. As shown in Section 5.4, the DW tune models τ-ID variables better than the ATLAS MC09 tune [49] used in this analysis. The difference in the number of events obtained for MC09 and DW tunes amounts to 16% for the $W \to \tau_h \nu_\tau$ signal and 17% for the EW background.

9.6 Cross section and luminosity

The expected number of signal and EW background events is obtained from the number of simulated events passing the event selection, scaled according to their corresponding cross sections and the integrated luminosity of the corresponding data sample. Therefore, the uncertainties on these numbers need to be considered.

The product of the cross sections for W and Z bosons production and their leptonic-decay branching ratios used in this study are calculated to NNLO in QCD using the FEWZ program [12] with the MSTW2008 set of parton distribution functions [13]. The uncertainties on these cross sections are evaluated in [14]. They arise from the choice of PDF (3%), from factorization and renormalization scale dependence, and the size of the correction from NLO to NNLO (4%). The total uncertainty of 5% is taken as an uncertainty on any event count

			$W \to \tau_\mathrm{h}\nu_\tau$	$W \to e\nu_e$	$W \to \mu\nu_\mu$	$W \to \tau_\ell\nu_\tau$	$Z \to \tau\tau$	Total EW bkgd
Energy scale $\|\eta\| < 3.2$								
	a	$N-1$						
	0.07	0.93	+15%	+8%	-5%	+13%	+20%	
	-0.07	0.93	-18%	-1%	-4%	-7%	-12%	
Energy scale $\|\eta\| > 3.2$								
	a							
	0.10		-1%	-1%	-2%	-8%	-2%	
	-0.10		+3%	+4%	0%	0%	+3%	
$E_\mathrm{T}^\mathrm{miss}$ resolution								
$\alpha = 0.65$ GeV$^{1/2}$			+10%	+7%	0%	+7%	+26%	
Excl. FCAL inner ring			+7%	+9%	+2%	+1%	+8%	
Combined syst. uncertainties								
Relative			+19%	+14%	+3%	+19%	+34%	+15%
			-22%	-11%	-5%	-15%	-30%	-13%
Absolute			+10.6	+0.6	+0.1	+0.3	+0.7	+1.7
			-12.1	-0.5	-0.2	-0.3	-0.6	-1.5

Table 9.1: Relative and absolute variation of acceptances for the systematics tests on the topological cluster energy scale, for $W \to \tau_\mathrm{h}\nu_\tau$ signal and EW backgrounds.

prediction normalized using those cross sections. An additional uncertainty on the event rate of 11% derives from the luminosity measurement [42], as discussed in Section 3.8.

9.7 QCD background estimation

The following sources of systematic uncertainty have been considered for the estimation of QCD background from data:

- **Correction for $W \to \tau_{\mathrm{h}}\nu_\tau$ signal and EW background:** The systematic uncertainty due to the correction for the $W \to \tau_{\mathrm{h}}\nu_\tau$ signal and EW background contamination in the three control regions used for the estimation of the QCD background is evaluated by varying the fraction of EW background events within the combined statistical and systematic uncertainties of the MC prediction presented in Table 9.2. The number of estimated QCD background events varied by $\pm 6\%$ and this value is considered for this systematic uncertainty.

- **$S_{E_{\mathrm{T}}^{\mathrm{miss}}}$ and τ_{h}-ID correlation:** An assumption of the method used for the estimation of QCD background is that the $S_{E_{\mathrm{T}}^{\mathrm{miss}}}$ and the τ_{h}-ID are not correlated. As can be seen in Figures 8.3(a) and 8.4(a), the $S_{E_{\mathrm{T}}^{\mathrm{miss}}}$ distribution for region AB is slightly shifted towards higher $S_{E_{\mathrm{T}}^{\mathrm{miss}}}$ values compared with region CD. This may be due to a non-negligible correlation between these variables. As a check, regions A and C were enlarged by changing the $S_{E_{\mathrm{T}}^{\mathrm{miss}}}$ requirement from 6 to 4, in order to obtain QCD-background-dominated samples in all four regions. The observed value of N^{A}, after subtraction of EW and $W \to \tau_{\mathrm{h}}\nu_\tau$ signal contributions, based on MC simulation, has been compared with the estimate from Equation 8.1. The same verification was performed for the medium τ_{h}-ID. The largest disagreement is observed for the first cross-check and amounts to 28%.

- **Additional tests (based on the studies presented in Section 8.2):** In $W \to \tau_{\mathrm{h}}\nu_\tau$ events, the $E_{\mathrm{T}}^{\mathrm{miss}}$, and therefore also $S_{E_{\mathrm{T}}^{\mathrm{miss}}}$, is correlated with the p_T of the τ_{h} candidate. The fact that the τ_{h} identification efficiency is not uniform as a function of p_T can lead to a potential systematic uncertainty. In order to verify this, the analysis is repeated for two different p_T ranges: $20-30\,\mathrm{GeV}$ GeV and $30-60\,\mathrm{GeV}$ as discussed in Section 8.2.2. The stability of the background estimation is also checked separately for τ_{h} candidates with 1 or more tracks and for events with single or multiple reconstructed primary vertices. All variations on the expected number of QCD background events in the signal region are statistically compatible with the estimation on the full sample. Therefore, the systematic uncertainty due to p_T dependence is negligible.

The total systematic uncertainty associated with the QCD background estimation is determined to be 29%.

9.8 Systematic uncertainty summary

Table 9.2 summarizes the resulting systematic uncertainties.

	$W \to \tau_h \nu_\tau$ signal	EW background	QCD background
Central values [events]	55.3	11.8	11.1
Statistical uncertainty [events]	±1.4	±0.4	±2.3
Systematic uncertainties:			
Lepton veto	–	±19%	–
Energy scale	±21%	±14%	–
Pile-up	±1%	±0.2%	–
Monte Carlo model	±16%	±17%	–
Theoretical cross section	± 5%	±5%	–
Luminosity	± 11%	±11%	–
QCD background estimation	–	–	±29%
Total systematic uncertainty [events]	±16.1	±3.7	±3.2

Table 9.2: Summary of the systematic uncertainties for the data-driven estimation of the QCD background and for the expectations for EW background and signal based on simulation. The statistical uncertainty for EW background and signal corresponds to the MC statistical uncertainty. The individual systematic uncertainties are quoted as relative values, while the resulting total uncertainties are quoted as absolute values.

The energy scale and MC model are the dominant source of systematic uncertainties associated the estimation of $W \to \tau_h \nu_\tau$ signal and EW background events. For the EW background, also the lepton veto has an important contribution. These uncertainties, however, may decrease in future studies when the ATLAS detector will be better understood and the ATLAS MC simulation better tuned. For the QCD background estimation, the uncertainty of 29% is also very large and its evaluation was probably too conservative.

Despite the fact that these systematic uncertainties are sizeable, the results obtained are with a sufficient sensitivity for the observation of $W \to \tau_h \nu_\tau$ events in ATLAS, as discussed in the next Chapter.

10. Results and Perspectives

The first part of this chapter summarizes the results of the analyses presented in the last three chapters. This is followed by a discussion, in Section 10.2, on the perspectives for physics measurements with the $W \to \tau\nu$ process in the near future.

10.1 $\mathrm{W} \to \tau\nu_\tau$ Analysis Results

A search for $W \to \tau\nu_\tau$ decays, with the τ lepton decaying into hadrons, has been presented. The analysis described in Chapter 7 selected a total of 78 data events from a data sample that corresponds to an integrated luminosity of 546 nb^{-1}, recorded with the ATLAS detector at the LHC in proton-proton collisions at a center-of-mass energy of $\sqrt{s} = 7\,\mathrm{TeV}$ from March to mid-August 2010.

In Chapter 8, the method to extract the QCD background contribution from data was presented together with its validation and $11.1{\pm}2.3_{(\mathrm{stat.})} \pm 3.2_{(\mathrm{syst.})}$ of these 78 events are estimated to be due to QCD processes. With a remaining background from W and Z decays of $11.8{\pm}0.4_{(\mathrm{stat.})} \pm 3.7_{(\mathrm{syst.})}$ events, evaluated from MC simulation, this leaves an observed signal of $55.1{\pm}10.5_{(\mathrm{stat.})} \pm 5.2_{(\mathrm{syst.})}$ events. This number is compatible with the Standard Model expectation of $55.3{\pm}1.4_{(\mathrm{stat.})} \pm 16.1_{(\mathrm{syst.})}$ events from $W \to \tau_\mathrm{h}\nu_\tau$ decays, estimated with simulated data. The probability for the amount of selected data events to be due to background only is 8.7×10^{-10}, using a Bayesian approach, and it corresponds to 6.1σ, using a one-sided normal distribution.

Equally important to ensure the observation of $W \to \tau\nu_\tau$ decays in ATLAS are the distributions of kinematical variables and the variables used in the τ_h-ID. The shapes of all these distributions are compatible with those obtained from simulated $W \to \tau_\mathrm{h}\nu_\tau$ signal.

Therefore, these results constitute the first observation of $W \to \tau\nu_\tau$ decays and of hadronically decaying τ leptons in ATLAS.

10.2 Perspectives

Before starting the heavy ion physics program in November 2010, the total amount of data recorded by the ATLAS experiment in proton-proton collisions at a center-of-mass energy of $\sqrt{s} = 7\,\mathrm{TeV}$ corresponds to an integrated luminosity of $45\,\mathrm{pb}^{-1}$. The peak instantaneous luminosity reached $2.1 \times 10^{32}\,\mathrm{cm}^{-2}\mathrm{s}^{-1}$. This larger data set, containing an increased amount of pile-up effects, allow one to test if the study described in this thesis contains eventual limitations or problems not observed before, due to the smaller data set, as well as its robustness against the additional pile-up effects. This and the perspectives for physics measurements with the $W \to \tau_\mathrm{h}\nu_\tau$ process are discussed in the following sections.

10.2.1 W $\to \tau\nu_\tau$ analysis using a larger data set

As discussed in Chapter 7, the $W \to \tau_\mathrm{h}\nu_\tau$ analysis is sensitive to pile-up effects and the trigger rates increases rapidly with the instantaneous luminosity. To keep the trigger rates within the allowed bandwidth of the trigger system, either the trigger requirements are pre-scaled (i.e. only a small fraction of events satisfying the trigger requirements are recorded) or the trigger threshold values are increased.

The $W \to \tau_\mathrm{h}\nu_\tau$ analysis used in this thesis can, however, be successfully repeated with the first $2.46\,\mathrm{pb}^{-1}$ of data collected with fully operational detector and stable beam conditions. Figure 10.1 shows the distributions of kinematical variables and variables used for the τ_h-ID with this integrated luminosity. A very good agreement between data and the expected $W \to \tau_\mathrm{h}\nu_\tau$ signal events combined with the estimated backgrounds is observed.

For the additional amount of data available, the instantaneous luminosity is higher and, consequently, the trigger requirement used in this study needed to be prescaled. However, other combinations of τ_h and $E_\mathrm{T}^\mathrm{miss}$ triggers with higher threshold values are available without prescale. Using these different trigger settings, this analysis can successfully select about 2000 $W \to \tau_\mathrm{h}\nu_\tau$ events with the full data set collected in 2010 [105]. This result also confirms that this analysis is robust against additional pile-up effects.

For the proton-proton collisions expected for 2011, the instantaneous luminosity will be further increased and higher trigger thresholds will be needed to keep the trigger rate within the allowed bandwidth. This will clearly affect the event selection described in this thesis. However, former studies [95] performed during the preparation for the first collisions showed that the $E_\mathrm{T}^\mathrm{miss}$ threshold requirement can be increased to $40\,\mathrm{GeV}$ and $W \to \tau_\mathrm{h}\nu_\tau$ events can still be selected, but with a lower efficiency. In fact, the higher $E_\mathrm{T}^\mathrm{miss}$ threshold further suppresses the QCD background and the $S_{E_\mathrm{T}^\mathrm{miss}}$ requirement may not be needed.

Another challenge for this analysis will be the development of a reliable method to estimate the contribution of QCD background from data. As discussed in [95], there is a possibility of

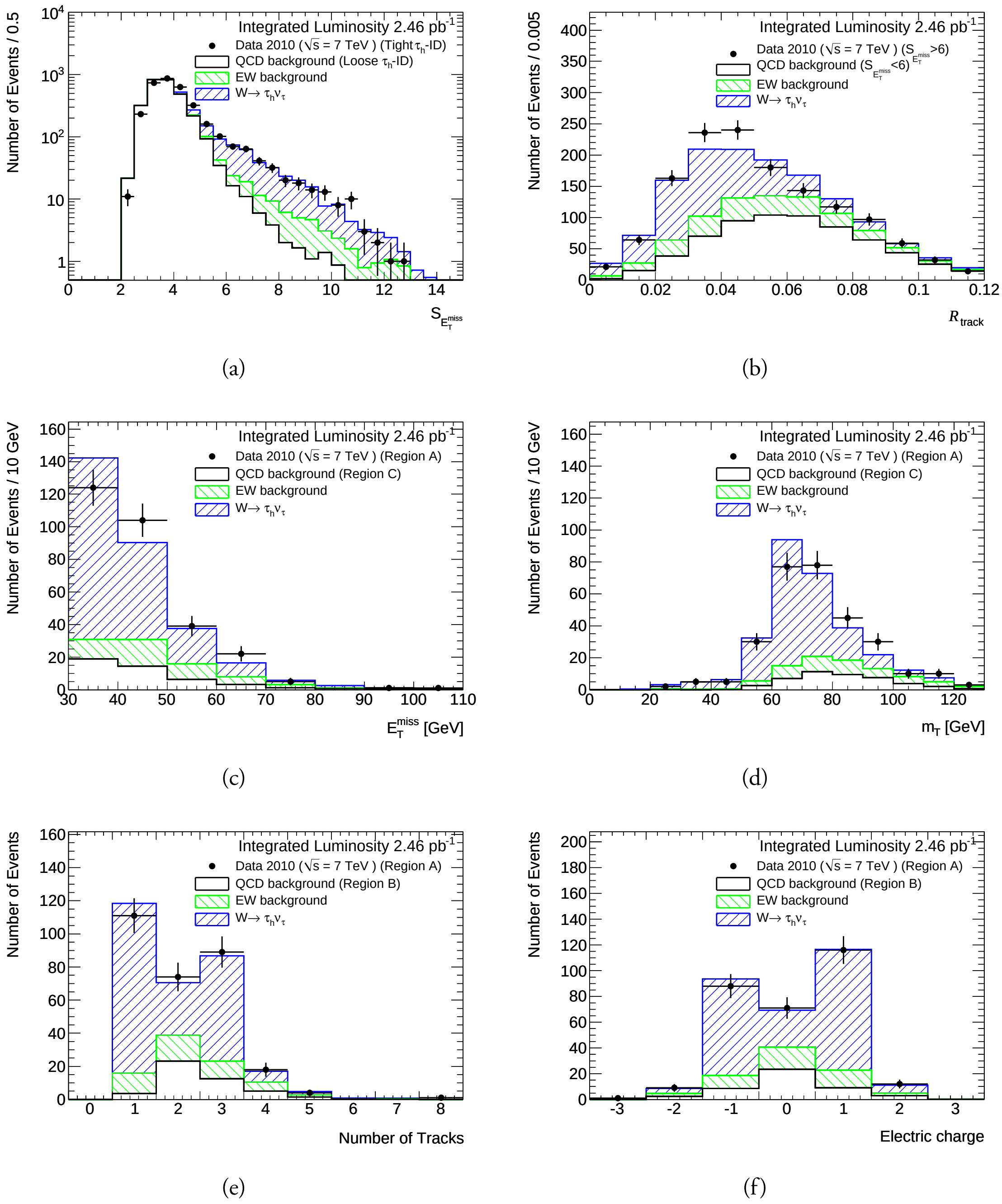

Figure 10.1: (a) $S_{E_T^{\text{miss}}}$, (b) R_{track}, (c) E_T^{miss}, (d) transverse mass m_T (e) τ_h track multiplicity and (f) electric charge distributions for $2.46\,\text{pb}^{-1}$ of data and the estimated QCD background combined with the expected signal and EW contributions, from MC simulation.

using a maximum-likelihood fit to determine the signal yield, using the m_T as discriminating variable for the fit, as shown in Figure 10.2. The shape of the m_T distribution for the QCD background is constrained by using a control sample, enriched by QCD background events, selected with a looser criterion on the τ_h candidate selection.

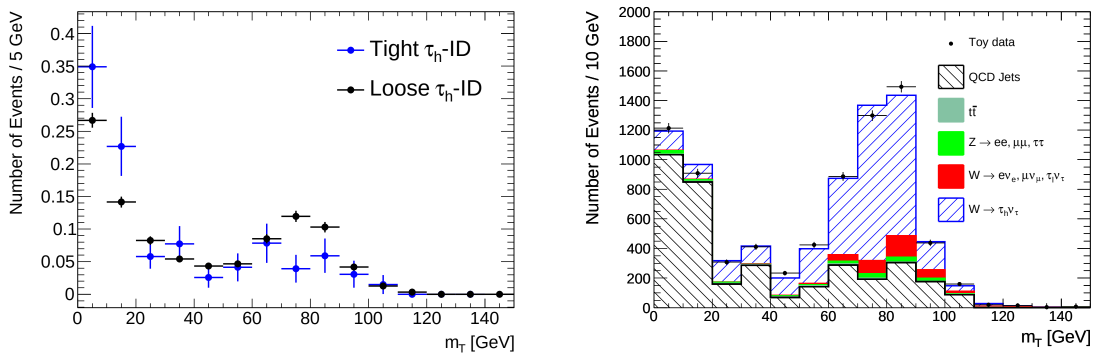

(a) (b)

Figure 10.2: (a) Transverse mass distribution after full event selection using the loose τ-ID and the tight τ-ID for QCD background (simulated sample) assuming a proton-proton center-of-mass energy of 10 TeV (the expected initial collision energy at the time) [95]. The distributions are normalized to unity. A larger data set of simulated QCD background was available in this study using a fast detector simulation software, which is based on the parametrized results of the detector performance studies carried out with the standard simulation. (b) Fit of the transverse-mass distribution to a "toy data sample", which has been produced by fluctuating the combined signal and background distributions according to a Poisson probability distribution [95]. The distribution has been normalized to $100\,\mathrm{pb}^{-1}$ of data, assuming a proton-proton center-of-mass energy of 10 TeV. The fitting technique used is an extended binned maximum-likelihood fit [95].

The $W \to \tau_h \nu_\tau$ events will continue to be relevant for the commissioning of the τ_h reconstruction and identification algorithms until the instantaneous luminosity increases to values above $10^{33}\,\mathrm{cm}^{-2}\mathrm{s}^{-1}$, when the trigger thresholds may be too high to efficiently collect $W \to \tau_h \nu_\tau$ signal events. There are, however, ongoing studies by the ATLAS Trigger Group investigating the feasibility to implement a trigger requirement based on $S_{E_T^{\mathrm{miss}}}$ requirement in the ATLAS detector. Such a trigger would allow a significant decrease in trigger rates and allow an efficient selection of $W \to \tau_h \nu_\tau$ events, extending the physics program for this channel to higher instantaneous luminosities than currently planned.

10.2.2 Physics measurements with W $\rightarrow \tau\nu_\tau$ decays

The selected sample of $W \rightarrow \tau_\mathrm{h}\nu_\tau$ events is currently being used for both τ_h identification performance studies and for physics measurements. These physics measurements are motivated by the understanding of the ATLAS detector. In particular, the $W \rightarrow \tau_\mathrm{h}\nu_\tau$ decay is an important background in new physics searches and may also be used as a control region in searches for processes with τ_h and $E_\mathrm{T}^\mathrm{miss}$ signatures, for example the charged Higgs boson discussed in Chapter 2. The following physics measurements are being investigated:

Cross section measurement

The $W \rightarrow \tau\nu_\tau$ production cross section was measured by CDF and D0 collaborations at Tevatron [106, 107] at a center-of-mass energy of $\sqrt{s} = 1.8\,\mathrm{TeV}$. CDF obtained for run II [106]:

$$\sigma(p\bar{p} \rightarrow W) \cdot BR(W \rightarrow \tau\nu_\tau) = 2.62 \pm 0.07_{(\mathrm{stat.})} \pm 0.21_{(\mathrm{syst.})} \pm 0.16_{(\mathrm{lum.})}\,\mathrm{nb},$$

and D0 for run I [108]:

$$\sigma(p\bar{p} \rightarrow W) \cdot BR(W \rightarrow \tau\nu_\tau) = 2.22 \pm 0.09_{(\mathrm{stat.})} \pm 0.10_{(\mathrm{syst.})} \pm 0.10_{(\mathrm{lum.})}\,\mathrm{nb}.$$

These values are in good agreement with the SM expectation. ATLAS is currently measuring this cross section with the total amount of data collected in 2010, at a higher center-of-mass energy of $\sqrt{s} = 7\,\mathrm{TeV}$. For this measurement, the τ identification algorithm used in this thesis may be replaced by a more sophisticated method using multivariate algorithms, increasing the purity of the $W \rightarrow \tau_\mathrm{h}\nu_\tau$ sample. Further improvement on the purity of the sample might come from:

- the selection of τ_h candidates with one or three tracks and electric charge equal to ± 1;
- exploiting the signature of the W boson decays by requiring $E_\mathrm{T}^\mathrm{miss}$ and the τ_h candidate to be opposite in the ϕ direction, i.e. $\Delta\phi(\tau, E_\mathrm{T}^\mathrm{miss}) > 2.5$.

The method to extract the QCD background contribution from data also needs to be revisited. It is likely that the same method used in this thesis will be used for the cross section measurement, but replacing the τ-ID criterion by the output score of the multivariate τ_h identification algorithm. The systematic uncertainty on the QCD background extraction, conservatively estimated as 29% in this thesis, should also be decreased. The better understanding of the data-driven method may be possible with the larger data samples available. The cross-section measurement will also establish and validate the hadronic τ identification algorithm that will be applied in Higgs boson searches as well as in new physics searches with τ leptons in the final state.

Lepton universality

The measurement of the W boson production cross section times branching ratio to τ lepton and neutrino, $\sigma(pp \to W+X)\cdot \mathrm{B}(W \to \tau\nu_\tau)$, can be used with the corresponding result from the electron channel, $\sigma(pp \to W+X)\cdot \mathrm{B}(W \to e\nu_e)$, to test one of the fundamental concepts in the SM: the universality of the leptonic couplings to the weak charged current, i.e. that the electroweak couplings to the three charged leptons, g_e, g_μ and g_τ are all equal. The lepton universality can be measured according to the relation:

$$(\frac{g_\tau}{g_e})^2 = \frac{\sigma\cdot \mathrm{B}(W \to \tau\nu_\tau)}{\sigma\cdot \mathrm{B}(W \to e\nu_e)}. \tag{10.1}$$

Both the CDF and D0 collaborations measured $\frac{g_\tau}{g_e}$ with $W \to \tau\nu_\tau$ events [106–108] and obtained values of $0.99 \pm 0.02_{\text{(stat.)}} \pm 0.04_{\text{(syst.)}}$ and $0.980 \pm 0.020_{\text{(stat.)}} \pm 0.024_{\text{(syst.)}}$, respectively, in good agreement with the SM prediction.

Charge asymmetry measurement

The measurement of the charge asymmetry of the decay leptons from W bosons produced in Drell-Yan processes at the LHC contributes to the understanding of the valence parton density functions. The difference in the production cross sections of W^+ and W^- can be quantified using the lepton asymmetry, which is defined as:

$$A_\ell = \frac{N_{\ell^+} - N_{\ell^-}}{N_{\ell^+} + N_{\ell^-}}. \tag{10.2}$$

The asymmetry also changes significantly as a function of lepton pseudorapidity, since η_ℓ is highly correlated with the kinematic phase space of the incoming partons and hence each bin probes partons with different average values of x. Inclusive measurements have been performed at the Tevatron [109, 110], for both $W \to e\nu$ and $W \to \mu\nu$ events, by the CDF and D0 collaborations and the data have been included in global fits of parton distributions [13, 111]. CDF also measured A_ℓ for $W \to \tau\nu$ events [107]. ATLAS has already measured A_ℓ for both $W \to e\nu$ and $W \to \mu\nu$ events [14] and the results are shown in Figure 10.3.

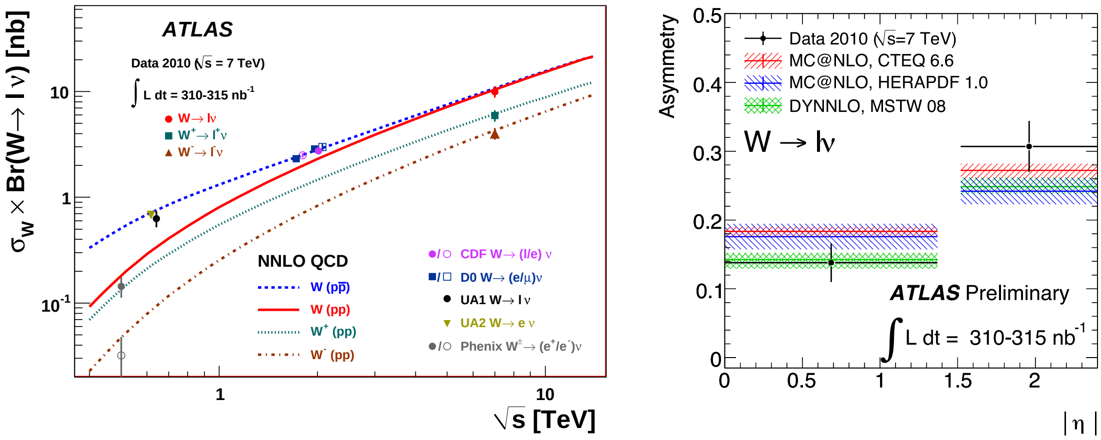

(a) (b)

Figure 10.3: (a) The measured values of $\sigma_W \times \mathrm{BR}(W \to \ell\nu)$ for W^+, W^- and for their sum compared to the theoretical predictions based on NNLO QCD calculations [14]. Results are shown for the combined electron-muon results. The predictions are shown for both proton-proton (W^+,W^- and their sum) and proton-antiproton colliders (W) as a function of $\sqrt{s}$. In addition, previous measurements at proton-antiproton and proton-proton colliders are shown. The data points at the various energies are staggered to improve readability. The CDF and D0 measurements are shown for both Tevatron collider energies, $\sqrt{s} = 1.8\,\mathrm{TeV}$ and $\sqrt{s} = 1.96\,\mathrm{TeV}$. All data points are displayed with their total uncertainty. The theoretical uncertainties are not shown. (b) Combined charge asymmetry in two eta bins (barrel $|\eta| < 1.37$ and endcap $1.52 < |\eta| < 2.4$) for an integrated luminosity of $315\,\mathrm{nb}^{-1}$ in the electron channel and $310\,\mathrm{nb}^{-1}$ in the muon channel and compared to different theoretical predictions [14]. Statistical and systematic uncertainties are included.

11. Conclusion

Physics studies of processes with τ leptons in the final state, while challenging at hadron colliders, are of great importance at the LHC, especially as probes for the Higgs boson search as well as for new physics searches with τ leptons in the final state. Decays of Standard Model particles to τ leptons, in particular $Z \to \tau\tau$ and $W \to \tau\nu_\tau$, are important background processes in those searches and, therefore, a complete understanding of these processes is vital. These signal processes are also important to study the performance of the τ-lepton reconstruction algorithms and to ensure that the identification of τ leptons is well understood.

In this thesis, studies connected to the reconstruction of τ lepton candidates using simulated data and the commissioning of the τ reconstruction and identification algorithms with the first collisions at the LHC were performed. The following results were obtained:

- Results relevant to track selection criteria used for τ-lepton reconstruction were presented. This study, carried out during the preparation for the first collisions at the LHC, lead to improvements on the τ reconstruction performance. It increased the τ selection efficiency and provided a better association of charged tracks with the τ candidates.

- With the data recorded during the first collisions at the LHC, studies related to τ reconstruction performance with hadronic jets from QCD background along with measurement of missing transverse energy were conducted. Measured distributions obtained from analysis of these first collisions agree well with the predictions of the detector simulation and event generator, demonstrating that the modeling of the detector response was in good shape prior to the first collisions from the LHC.

The remarkable performance of the ATLAS detector during the initial data-taking phase of the LHC allowed for the observation of $W \to \tau\nu_\tau$ events and of the first τ leptons decaying hadronically. The ATLAS collaboration has put a significant effort in implementing new triggers to improve the efficiency of the selection of hadronic τ decays. The material presented in this thesis summarized the work done on the analysis to efficiently select the $W \to \tau_\mathrm{h}\nu_\tau$ signal events whilst providing the required large rejection against the overwhelming backgrounds from hadronic jets. The observation of $W \to \tau_\mathrm{h}\nu_\tau$ decays could mainly be made possible by:

- the requirement of a minimum criterion on the significance of the missing transverse energy, $S_{E_{\mathrm{T}}^{\mathrm{miss}}}$, which provided a strong rejection of QCD background events;
- the development and validation of a reliable method to estimate the QCD background contribution directly from data.

Both items listed above were fundamental for this early observation of $W \to \tau_{\mathrm{h}}\nu_{\tau}$ events. The analysis resulted in the selection of 78 candidate events, in good agreement with the sum of the Monte Carlo predictions for the $W \to \tau_{\mathrm{h}}\nu_{\tau}$ signal and electroweak background of $55.3{\pm}1.4_{\mathrm{(stat.)}} \pm 16.1_{\mathrm{(syst.)}}$ and $11.8{\pm}0.4_{\mathrm{(stat.)}} \pm 3.7_{\mathrm{(syst.)}}$ events, respectively, and the QCD background estimated from data of $11.1{\pm}2.3_{\mathrm{(stat.)}} \pm 3.2_{\mathrm{(syst.)}}$ events. Up to now, the $W \to \tau\nu_{\tau}$ decay process is the only observed source of τ_{h} available in ATLAS. There are ongoing studies to observe τ leptons from Z decays that may be completed very soon [112]. Further physics measurements with τ leptons are foreseen in the near future:

- $W \to \tau\nu$ cross section,
- $Z \to \tau\tau$ observation and cross section,
- new physics searches: charged Higgs boson and other supersymmetric particles,
- SM Higgs boson decaying into a pair of τ leptons.

Thus, this first observation of $W \to \tau\nu$ decays and of hadronically decaying τ leptons in ATLAS is an important first step in the physics program of the ATLAS experiment towards the measurement of processes with τ leptons in the final state.

A. Validation of the data-driven method

The following sections show complementary information for the validation of the data-driven method discussed in Chapter 8.

A.1 Study of τ_h candidates in different $\mathbf{p_T}$ ranges

A different approach to confirm the validity of the data-driven method for a QCD background estimation is to consider τ_h candidates in different p_T regions separately. To obtain data samples of approximately the same size for this study, the following p_T regions have been defined:

- τ_h candidates with a transverse momentum between $20\,\mathrm{GeV} < p_T < 30\,\mathrm{GeV}$.
- τ_h candidates with a transverse momentum between $30\,\mathrm{GeV} < p_T < 60\,\mathrm{GeV}$.

The number of events for each subsample for data and the signal and EW Monte Carlo events in the four different regions are listed in Table A.1.

Region		A	B	C	D
$20\,\mathrm{GeV} < p_T < 30\,\mathrm{GeV}$	Data	23	201	58	2487
	$W \to \tau_\mathrm{h} \nu_\tau$	21.3±0.9	13.7±0.7	27.9±1.0	24.1±1.0
	EW	2.5±0.2	1.9±0.1	10.4±0.3	7.8±0.3
	c_i		0.66±0.04	1.61±0.08	1.34±0.07
$30\,\mathrm{GeV} < p_T < 60\,\mathrm{GeV}$	Data	55	406	196	4620
	$W \to \tau_\mathrm{h} \nu_\tau$	34.0±1.1	25.9±1.0	43.1±1.3	30.1±1.1
	EW	9.2±0.3	4.5±0.2	34.1±0.6	14.3±0.4
	c_i		0.70±0.03	1.79±0.06	1.03±0.04

Table A.1: Number of observed events and Monte Carlo expectations in the four regions for a data sample with τ_h candidates within a transverse momentum range of $20\,\mathrm{GeV} < p_T < 30\,\mathrm{GeV}$ and $30\,\mathrm{GeV} < p_T < 60\,\mathrm{GeV}$.

The number of expected QCD-background events, based on the numbers in Table A.1, are 1.9 ± 0.9 for $20\,\mathrm{GeV} < p_T < 30\,\mathrm{GeV}$ and 9.4 ± 2.1 for $30\,\mathrm{GeV} < p_T < 60\,\mathrm{GeV}$.

A.2 Separation of 1-prong and multi-prong τ_h candidates

For further confirmation of the validity of the data-driven method to extract the QCD background, the selected events have been divided into subsamples according to their number of tracks, and the performance of the method has been studied separately. The following subsamples have been defined:

- $\tau_h$candidates with exactly one track ("1-prong").
- $\tau_h$candidates with more than one track ("multi-prong").

The number of data events in the four defined regions as well as the Monte Carlo expectations for signal and EW backgrounds are listed in Table A.2 for 1-prong and multi-prong τ_h candidates.

Region		A	B	C	D
1-prong	Data	26	71	45	289
	$W \to \tau_h \nu_\tau$	27.6±1.0	19.1±0.9	25.9±1.0	23.6±1.0
	EW	3.2±0.2	2.5±0.1	3.9±0.2	2.3±0.1
	c_i		0.70±0.04	0.96±0.05	0.84±0.04
multi-prong	Data	52	536	209	6818
	$W \to \tau_h \nu_\tau$	27.7±1.0	20.4±0.9	45.1±1.3	30.6±1.1
	EW	8.5±0.3	4.0±0.2	40.6±0.7	19.7±0.5
	c_i		0.68±0.03	2.38±0.08	1.41±0.05

Table A.2: Number of observed events and Monte Carlo expectations in the four regions for a data sample with 1-prong τ_h candidates.

The number of estimated QCD background events in the signal region A is 5.5 ± 2.8 for 1-prong τ_h candidates and 7.8 ± 2.2 for multi-prong τ_h candidates.

A.3 Separation of events with one vertex and more than one vertex

The data-driven method has also been tested using subsamples of events with one vertex and with more than one vertex to validate its performance with events including pile-up effects. All vertices with more than three tracks are counted and used to classify the event. An overview of the full event selection is given in Table A.3.

	One vertex		More than one vertex	
	Data	$W \to \tau_h \nu_\tau$	Data	$W \to \tau_h \nu_\tau$
QCD jets rejection	188974	366.1±3.6	226979	362.2±3.6
$E_T^{miss} > 30$ GeV	9820	204.6±2.7	19867	206.9±2.8
τ selection	1274	64.6±1.6	1134	53.4±1.4
Lepton rejection	288	52.3±1.4	397	42.6±1.3
$S_{E_T^{miss}} > 6$	58	37.9±1.2	20	17.4±0.8

Table A.3: Number of events passing the selection criteria for data and Monte Carlo signal, normalized to the integrated luminosity of 546 nb^{-1}. The samples are separated in events with one reconstructed vertex with more than three tracks and events with more than one reconstructed vertex with more than three tracks.

The number of data events in the four defined regions as well as the Monte Carlo expectations for signal and EW backgrounds are listed in Table A.4 for events with one reconstructed vertex and for events with more than one reconstructed vertex. Based on the numbers in Table A.4 the estimated number of QCD background events in the signal region A is 10.5 ± 2.5 for events with one vertex and 2.8 ± 1.1 for events with more than one vertex.

Region		A	B	C	D
1-vertex	Data	58	230	181	2171
	$W \to \tau_h \nu_\tau$	37.9±1.2	14.3±0.7	44.7±1.3	14.4±0.7
	EW	7.5±0.3	2.3±0.1	26.9±0.6	7.0±0.3
	c_i		0.365±0.021	1.576±0.054	0.472±0.024
>1-vertex	Data	20	377	73	4936
	$W \to \tau_h \nu_\tau$	17.4±0.8	25.2±1.0	26.3±1.0	39.8±1.2
	EW	4.2±0.2	4.2±0.2	17.6±0.5	15.1±0.4
	c_i		1.36±0.07	2.03±0.10	2.54±0.12

Table A.4: Number of observed events and Monte Carlo expectations in the four regions for events with one reconstructed vertex with more than three tracks.

A.4 Event selection with medium τ_h ID

Figure A.1 shows the distributions for $S_{E_T^{miss}}$ and the τ_h-ID variables for data and the combined $W \to \tau_h \nu_\tau$ signal, EW background (based on MC) and QCD background (estimated with the data-driven method) for medium τ_h-ID candidates.

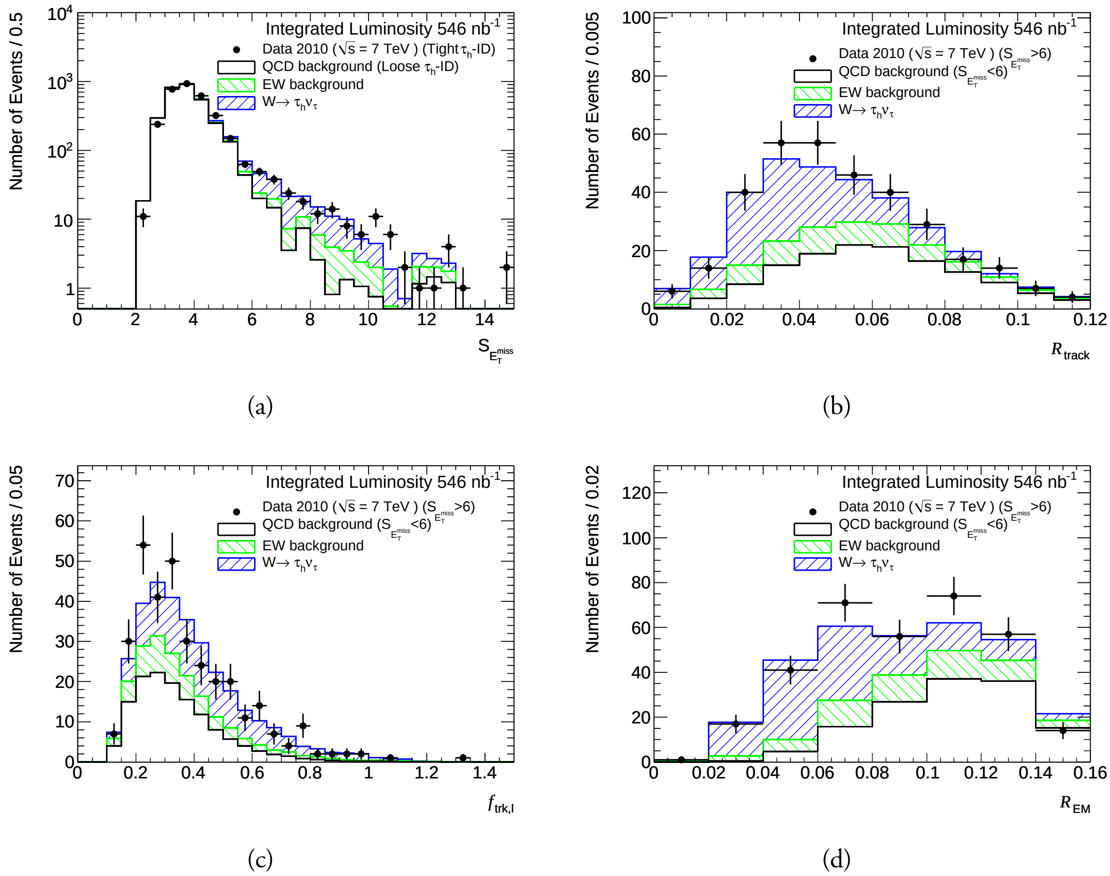

Figure A.1: (a) Distribution of $S_{E_T^{miss}}$ for data in the combined region AB (tight τ_h-ID region) and the QCD background estimated from the combined control region CD (loose τ_h-ID region) scaled by $(N^B - c_B N^A_{non-QCD})/(N^D - c_D N^A_{non-QCD})$. Also shown are the expected $W \to \tau_h \nu_\tau$ signal and EW background in region AB from simulated samples. (b), (c) and (d) Distribution of R_{track}, $f_{trk,I}$ and R_{EM} for events in the combined region AC ($S_{E_T^{miss}} > 6$) and for the QCD background estimated from the combined control region BD ($S_{E_T^{miss}} < 6$) together with the expectations from MC for $W \to \tau_h \nu_\tau$ signal and EW background. The tight τ_h-ID requirement was replaced by the medium τ_h-ID.

Figure A.2 show the p_T, η, track multiplicity and electric charge distributions for data and the combined $W \to \tau_h \nu_\tau$ signal, EW background (based on MC) and QCD background (estimated with the data-driven method) for medium τ_h-ID candidates.

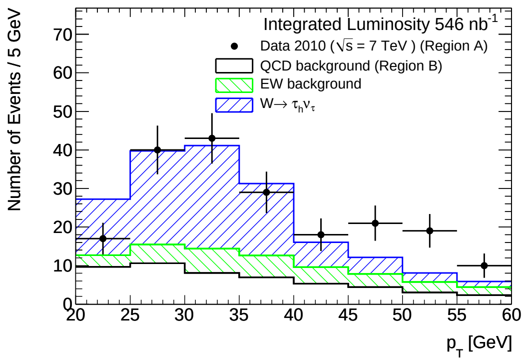

(a)

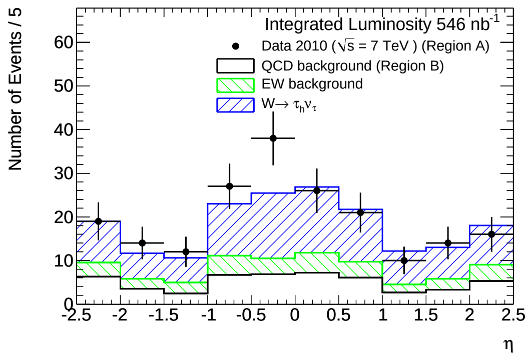

(b)

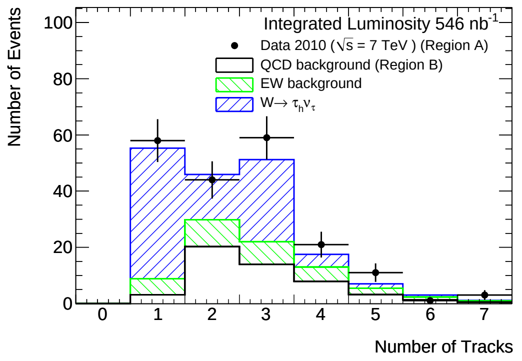

(c)

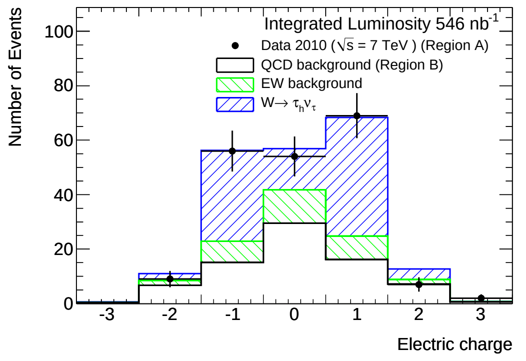

(d)

Figure A.2: Distributions of (a) p_T, (b) η, (c) track multiplicity and (d) electric charge of τ_h candidates for the data in signal region A, the scaled QCD background from control region B, and the contributions from $W \to \tau_\mathrm{h}\nu_\tau$ signal and EW background in region A. The QCD background distribution is normalized to the estimated number of QCD background events in region A ($\mathrm{N}^{\mathrm{A}}_{\mathrm{QCD}}$). The tight τ_h-ID requirement was replaced by the medium τ_h-ID.

Figure A.3 shows the $E_\mathrm{T}^{\mathrm{miss}}$ and $\sum E_T$ distributions for data in signal region A, the scaled QCD background from control region C, and the contributions from signal and EW background in region A using medium τ_h-ID candidates, instead of tight τ_h-ID.

Figure A.4 illustrates the $\Delta\phi(\tau_\mathrm{h}, E_\mathrm{T}^{\mathrm{miss}})$ and the transverse mass distributions for data in signal region A, the scaled QCD background from control region C, and the contributions from signal and EW background in region A using medium τ_h-ID candidates, instead of tight τ_h-ID.

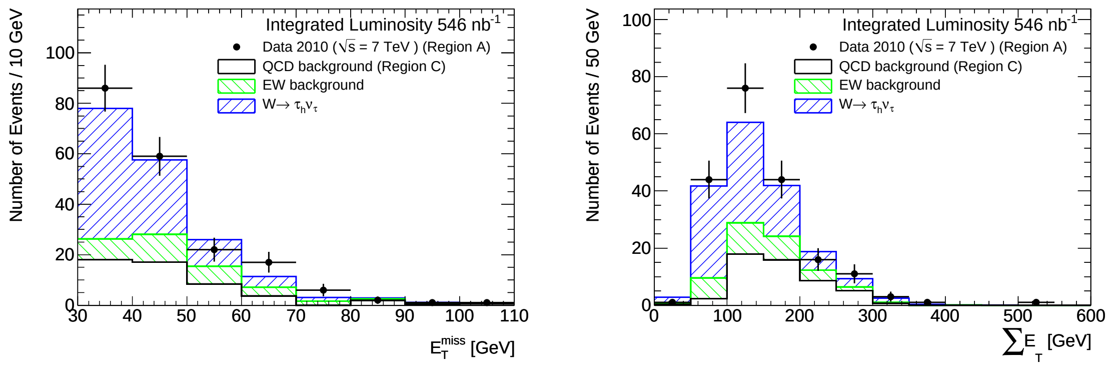

(a) (b)

Figure A.3: Distributions of $E_{\mathrm{T}}^{\mathrm{miss}}$ and $\sum E_T$ for the data in signal region A, the scaled QCD background from control region C, and the contributions from signal and EW background in region A. The QCD background distribution is normalized to the estimated number of QCD background events in region A ($\mathrm{N}_{\mathrm{QCD}}^{\mathrm{A}}$). The tight τ_{h}-ID requirement was replaced by the medium τ_{h}-ID.

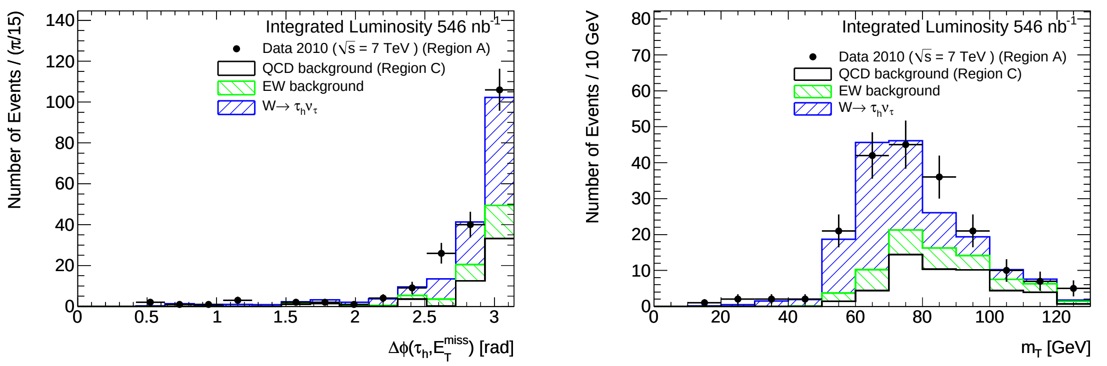

(a) (b)

Figure A.4: Distribution of (a) $\Delta\phi(\tau_{\mathrm{h}}, E_{\mathrm{T}}^{\mathrm{miss}})$ and (b) transverse mass m_T for data in the signal region and the scaled QCD background from control region C, combined with MC $W \to \tau_{\mathrm{h}}\nu_\tau$ signal and EW background. The QCD background distribution is normalized to the estimated number of QCD background events $\mathrm{N}_{\mathrm{QCD}}^{\mathrm{A}}$.

Bibliography

[1] ATLAS Collaboration, *Search for the Standard Model Higgs Boson via Vector Boson Fusion Production process in the Di-Tau Channels*, in *Expected Performance of the ATLAS Experiment, Detector, Trigger and Physics*, pp. 1271–1305. CERN-OPEN-2008-020, CERN, Geneva, 2008.

[2] ATLAS Collaboration, *Charged Higgs Boson Searches*, in *Expected Performance of the ATLAS Experiment: Detector, Trigger and Physics*, pp. 1451–1479. CERN-OPEN-2008-020, CERN, Geneva, 2008.

[3] ATLAS Collaboration, *Discovery Potential of $A/H \to \tau^+\tau^- \to \ell h$ in ATLAS*, ATL-PHYS-PUB-2010-011.

[4] ATLAS Collaboration, *Expected Sensitivity in Light Charged Higgs Boson Searches for $H^+ \to \tau^+\nu$ and $H^+ \to c\bar{s}$ with Early LHC Data at the ATLAS Experiment*, ATL-PHYS-PUB-2010-006.

[5] ALEPH Collaboration, Z. Zhang, *Tau lepton physics at LEP*, PoS **HEP2005** 290(2006) , `arXiv, hep-ex/0602044`.

[6] DELPHI Collaboration, J. Abdallah et al., *A precise measurement of the tau lifetime*, Eur. Phys. J. **C36** 283–296(2004) , `arXiv, hep-ex/0410010`.

[7] Babar Collaboration, A. Lusiani, *Measurement of the tau lepton lifetime with BaBar*, Nucl. Phys. Proc. Suppl. **144** 105–112(2005) .

[8] Belle Collaboration, H. Hayashii and M. Fujikawa, *Recent Belle results on the hadronic decays of tau lepton*, Nucl. Phys. Proc. Suppl. **198** 157–164(2010) .

[9] BES Collaboration, X. Shen, *Recent results from BESII*, Int. J. Mod. Phys. **A24** 279–286(2009) .

[10] CLEO Collaboration, A. Weinstein, *CLEO contributions to tau physics*, eConf **C0209101** TU15(2002) , `arXiv, hep-ex/0210058`.

[11] A. G. Shamov et al., *Tau mass measurement at KEDR*, Nucl. Phys. Proc. Suppl. **189** 21–23(2009) .

[12] C. Anastasiou, L. Dixon, K. Melnikov and F. Petriello, *High-precision QCD at hadron colliders: electroweak gauge boson rapidity distributions at NNLO*, Phys. Rev. **D69** 094008(2004) .

[13] A. D. Martin, W. J. Stirling, R. S. Thorne and G. Watt, *Parton distributions for the LHC*, Eur. Phys. J. **C63** 189–285(2009) , `arXiv, 0901.0002 [hep-ph]`.

[14] Atlas Collaboration, G. Aad et al., *Measurement of the $W \to \ell\nu$ and $Z/\gamma* \to \ell\ell$ production cross sections in proton-proton collisions at $\sqrt{s}$ =7 TeV with the ATLAS detector*, JHEP **1012** 060(2010) , `arXiv, 1010.2130 [hep-ex]`.

[15] ATLAS Collaboration, *Observation of $W \to \tau\nu$ Decays with the ATLAS Experiment*, ATLAS-CONF-2010-097.

[16] T. Morii et al., *The Physics of the Standard Model and Beyond*, World Scientific Publishing CO, Singapore, 2004.

[17] H. Spiesberger, M. Spira, and P. M. Zerwas, *The Standard model: Physical basis and scattering experiments*, `arXiv, hep-ph/0011255`.

[18] G. Nakamura and others (Particle Data Group), J. Phys. G **37** 075021(2010) . `http://pdg.lbl.gov`.

[19] J. Goldstone, *Field Theories with Superconductor Solutions*, Nuovo Cim. **19** 154–164(1961) .

[20] A. S. J. Goldstone and S. Weinberg, *Broken Symmetries*, Phys. Rev. **127** 965–970(1962) .

[21] M. Herrero, *The Standard model*, `arXiv, hep-ph/9812242`.

[22] B. W. Lee, Benjamin, C. Quigg and H. B. Thacker, *Weak Interactions at Very High-Energies: The Role of the Higgs Boson Mass*, Phys. Rev. **D16** 1519(1977) .

[23] J. R. Espinosa and M. Quiros, *Improved metastability bounds on the standard model Higgs mass*, Phys. Lett. **B353** 257–266(1995) , `arXiv, hep-ph/9504241`.

[24] T. Hambye and K. Riesselmann, *SM Higgs mass bounds from theory*, Phys. Rev. D **55** 7255(1997) .

[25] The LEP Working Group for Higgs Boson Searches, ALEPH Collaboration, DELPHI Collaboration, L3 Collaboration and OPAL Collaboration, R. Barate et al., *Search for the Standard Model Higgs Boson at LEP*, Phys. Lett. B **565** 61–75(2003) , `hep-ex/0306033, CERN-EP-2003-011`.

[26] J. Alcaraz, *Precision Electroweak Measurements and Constraints on the Standard Model*, `arXiv, 0911.2604 [hep-ex]`. `http://lepewwg.web.cern.ch/LEPEWWG`.

[27] LHC Higgs Cross Section Working Group Collaboration, S. Dittmaier et al., *Handbook of LHC Higgs Cross Sections: 1. Inclusive Observables*, `arXiv, 1101.0593 [hep-ph]`.

[28] ATLAS Collaboration, *Introduction on Higgs Boson Searches*, in *Expected Performance of the ATLAS Experiment, Detector, Trigger and Physics*, pp. 1198–1211. CERN-OPEN-2008-020, CERN, Geneva, 2008.

[29] D.R. Tovey on behalf of the ATLAS and CMS Collaborations, *Searches for New Physics at the LHC*, ATL-CONF-2002-005 (2002) .

[30] O. Eboli and D. Zeppenfeld, *Observing an invisible Higgs boson*, Phys. Lett. B **495** 147–154(2000) , `hep-ph/0009158, MADPH-00-1191`.

[31] C. Lefèvre. CERN-DI-0812015.

[32] ATLAS Collaboration, G. Aad et al., *The ATLAS Experiment at the CERN Large Hadron Collider*, JINST **3** S08003(2008) .

[33] ATLAS Collaboration, *ATLAS Detector and Physics Performance Technincal Design Report*, CERN/LHCC/99-14 **I** (1999) .

[34] ATLAS Collaboration, *ATLAS Inner Detector Technincal Design Report*, CERN/LHCC/97-16 **I** (1997) .

[35] ATLAS Collaboration, *ATLAS Calorimeter Performance Technincal Design Report*, CERN/LHCC/96-40 (1997) .

[36] ATLAS Collaboration, *ATLAS Muon Spectrometer Technincal Design Report*, CERN/LHCC/97-22 (1997) .

[37] ATLAS Collaboration, *Barrel Toroid Technincal Design Report*, CERN/LHCC/97-19 **2** (1997) .

[38] ATLAS Collaboration, *Charged particle multiplicities in pp interactions for track p_T >100 MeV at $\sqrt{s}$ =0.9 and 7 TeV measured with the ATLAS detector at the LHC*, ATLAS-CONF-2010-046.

[39] J. Garvey et al., *Use of an FPGA to identify electromagnetic clusters and isolated hadrons in the ATLAS level-1 calorimeter trigger*, Nucl. Inst. Meth. **A512** 506–516(2003) .

[40] ATLAS Collaboration, *The ATLAS missing E_T trigger performance with initial LHC runs at $\sqrt{s} = 7$ TeV*, ATLAS-COM-CONF-2011-015.

[41] ATLAS Collaboration, D. Casadei et al., *The implementation of the ATLAS missing E_T triggers for the initial LHC operation*, ATL-COM-DAQ-2011-010.

[42] ATLAS Collaboration, *Luminosity Determination Using the ATLAS Detector*, ATLAS-CONF-2010-060.

[43] M. A. Dobbs et al., *Les Houches guidebook to Monte Carlo generators for hadron collider physics*, `arXiv, hep-ph/0403045`.

[44] F. Siegert, *Monte-Carlo event generation for the LHC.* PhD thesis, Durham University, 2010. `http://etheses.dur.ac.uk/484/`.

[45] T. Sjoestrand, S. Mrenna and P. Skands, *PYTHIA 6.4 physics and manual*, JHEP **05** 026(2006) .

[46] G. Barrand et al., *GAUDI - A software architecture and framework for building HEP data processing applications*, Comput. Phys. Commun. **140** 45–55(2001) .

[47] G. Barrand et al., *GAUDI - The software architecture and framework for building LHCb data processing applications*, Prepared for International Conference on Computing in High-Energy Physics and Nuclear Physics (CHEP 2000), Padova, Italy, 7-11 Feb 2000.

[48] ATLAS Collaboration, G. Aad et al., *The ATLAS Simulation Infrastructure*, Eur.Phys.J. **C70** 823–874(2010) , `arXiv, 1005.4568 [physics.ins-det]`.

[49] ATLAS Collaboration, *ATLAS Monte Carlo tunes for MC09*, Atl-phys-pub-2010-002.

[50] A. Sherstnev and R. S. Thorne, *Parton Distributions for LO Generators*, Eur. Phys. J. **C55** 553–575(2008) , `arXiv, 0711.2473 [hep-ph]`.

[51] R. Field, *Min-Bias and Underlying Event at the Tevatron and the LHC*, talk presented at the Fermilab MC Tuning Workshop (Oct 2002).

[52] S. Jadach et al., *The tau decay library, TAUOLA: version 2.4*, Comp. Phys. Commun. **76** 361(1993) .

[53] S. Jadach, J. H. Kuhn and Z. Was, *TAUOLA: A library of Monte Carlo programs to simulate decays of polarized tau leptons*, Comp. Phys. Commun. **64** 275–299(1990) .

[54] T. Pierzchala, E. Richter-Was, Z. Was and M. Worek, *Spin effects in tau lepton pair production at LHC*, Acta Phys. Polon. **B 32** 1277–1296(2001) .

[55] E. Barberio, B. van Eijk, and Z. Was, *PHOTOS: A Universal Monte Carlo for QED radiative corrections in decays*, Comp. Phys. Commun. **66** 115–128(1991) .

[56] A. Agostinelli et al., *GEANT4: A simulation toolkit*, Nucl. Inst. Meth. **A506** 250–303(2003) .

[57] ATLAS Collaboration, G. Duckeck, (Ed.) et al., *ATLAS computing: Technical design report*, CERN-LHCC-2005-022 .

[58] W. Lampl et al., *Calorimeter Clustering Algorithms : Description and Performance*, ATL-LARG-PUB-2008-002.

[59] M. Aleksa et al., *ATLAS Combined Testbeam: Computation and Validation of the Electronic Calibration Constants for the Electromagnetic Calorimeter*, ATL-LARG-PUB-2006-003, 2006.

[60] ATLAS Collaboration, G. Aad et al., *Readiness of the ATLAS Liquid Argon Calorimeter for LHC Collisions*, `arXiv, 0912.2642 [physics.ins-det]`.

[61] ATLAS Collaboration, *Readiness of the ATLAS Tile Calorimeter for LHC collisions*, `arXiv, 1007.5423 [physics.ins-det]`.

[62] ATLAS Collaboration, *Properties of Jets and Inputs to Jet Reconstruction and Calibration with the ATLAS Detector Using Proton-Proton Collisions at $\sqrt{s} = 7$ TeV*, ATLAS-CONF-2010-053.

[63] T. Barillari et al., *Local Hadron Calibration*, ATL-LARG-PUB-2009-001.

[64] ATLAS Collaboration, *Performance of the missing transverse energy reconstruction and calibration in proton-proton collisions at center-of-mass energy of $\sqrt{s} = 7$ TeV with the ATLAS detector*, ATLAS-CONF-2010-057.

[65] M. Cacciari, G. P. Salam, P. Gavin and G. Soyez, *The anti-k_t jet clustering algorithm*, JHEP **04** 063(2008) , `arXiv, 0802.1189 [hep-ph]`.

[66] ATLAS Collaboration, *Jet Reconstruction Performance*, in *Expected Performance of the ATLAS Experiment: Detector, Trigger and Physics*, pp. 262–297. CERN-OPEN-2008-020, CERN, Geneva, 2008.

[67] ATLAS Collaboration, *Measurement of inclusive jet and dijet cross sections in proton-proton collisions at 7 TeV centre-of-mass energy with the ATLAS detector*, `arXiv, 1009.5908 [hep-ex]`.

[68] ATLAS Collaboration, *Measurement of dijet production with a jet veto in pp collisions at $\sqrt{s} = 7$ TeV using the ATLAS detector*, ATLAS-CONF-2010-085.

[69] ATLAS Collaboration, *Jet Energy Resolution and Selection Efficiency Relative to Track Jets from In-situ Techniques with the ATLAS Detector Using Proton-Proton Collisions at a Center of Mass Energy $\sqrt{s} = 7$ TeV*, ATLAS-CONF-2010-054.

[70] ATLAS Collaboration, *ATLAS Calorimeter Response to Single Isolated Hadrons and Estimation of the Calorimeter Jet Scale Uncertainty*, ATLAS-CONF-2010-052.

[71] ATLAS Collaboration, *Electron and photon reconstruction and identification in ATLAS: expected performance at high energy and results at $\sqrt{s} = 900$ GeV*, ATLAS-CONF-2010-005.

[72] S. Hassani et al., *A muon identification and combined reconstruction procedure for the ATLAS detector at the LHC using the (MUONBOY, STACO, MuTag) reconstruction packages*, Nucl. Instrum. Meth. **A572** 77–79(2007) .

[73] ATLAS Collaboration, *Reconstruction and Identification of Hadronic τ Decays*, in *Expected Performance of the ATLAS Experiment: Detector, Trigger and Physics*, pp. 230–260. CERN-OPEN-2008-020, CERN, Geneva, 2008.

[74] G. D. Lafferty, *Prospects for tau physics*, Nucl. Phys. Proc. Suppl. **189** 358–365(2009) .

[75] E. Richter-Was and T. Szymocha, *Hadronic tau identification with track based approach: the $Z \to \tau\tau$, $W \to \tau\nu$ and dijet events from DC1 data samples*, ATL-PHYS-PUB-2005-005.

[76] M. Cacciari, G. P. Salam and G. Soyez, *The anti-k_t jet clustering algorithm*, JHEP **04** 063(2008) .

[77] ATLAS Collaboration, *Detector Level Jet Corrections*, in *Expected Performance of the ATLAS Experiment: Detector, Trigger and Physics*, pp. 300–308. CERN-OPEN-2008-020, CERN, Geneva, 2008.

[78] ATLAS Collaboration, *Reconstruction of hadronic tau candidates in QCD events at ATLAS with 7 TeV proton-proton collisions*, ATLAS-CONF-2010-059.

[79] ATLAS Collaboration, *Cut-based Identification of Hadronic τ Decays in Early ATLAS Data*, ATLAS-PHYS-PUB-2010-001.

[80] ATLAS Collaboration, *Tau Reconstruction and Identification Performance at ATLAS*, ATLAS-CONF-2010-086.

[81] ATLAS Collaboration, *Tau Data Quality Good Run Lists for ICHEP 2010*, ATL-COM-PHYS-2010-405.

[82] ATLAS Collaboration, *Data-Quality Requirements and Event Cleaning for Jets and Missing Transverse Energy Reconstruction with the ATLAS Detector in Proton-Proton Collisions at a Center-of-Mass Energy of $\sqrt{s} = 7$ TeV*, ATLAS-CONF-2010-038.

[83] ATLAS Collaboration, *Performance of the ATLAS Jet Trigger in the Early $\sqrt{s} = 7\,\mathrm{TeV}$ Data*, ATLAS-CONF-2010-094.

[84] UA1 Collaboration, G. Arnison et al., *Experimental observation of isolated large transverse energy electrons with associated missing energy at s**(1/2) = 540-GeV*, Phys. Lett. **B122** 103–116(1983) .

[85] UA2 Collaboration, M. Banner et al., *Observation of single isolated electrons of high transverse momentum in events with missing transverse energy at the CERN anti-p p collider*, Phys. Lett. **B122** 476–485(1983) .

[86] UA1 Collaboration, G. Arnison et al., *Experimental observation of lepton pairs of invariant mass around 95-GeV/c**2 at the CERN SPS collider*, Phys. Lett. **B126** 398–410(1983) .

[87] UA2 Collaboration, P. Bagnaia et al., *Evidence for Z0 –> e+ e- at the CERN anti-p p collider*, Phys. Lett. **B129** 130–140(1983) .

[88] A. D. Martin, R. G. Roberts, W. J. Stirling and R. S. Thorne, *Parton distributions and the LHC: W and Z production*, Eur. Phys. J. **C14** 133–145(2000) , `arXiv, hep-ph/9907231`.

[89] UA1 Collaboration, C. Albajar et al., *Studies of Intermediate Vector Boson Production and Decay in UA1 at the CERN Proton - Antiproton Collider*, Z. Phys. **C44** 15–61(1989) .

[90] UA2 Collaboration, J. Alitti et al., *Measurement of the transverse momentum distributions of W and Z bosons at the CERN anti-p p collider*, Z. Phys. **C47** 523–532(1990) .

[91] CDF Collaboration, F. Abe et al., *Search for flavor changing neutral current B meson decays in $p\bar{p}$ collisions at $\sqrt{s} = 1.8$ TeV*, Phys. Rev. Lett. **76** 4675–4680(1996) .

[92] D0 Collaboration, S. Abachi et al., *Second generation leptoquark search in $p\bar{p}$ collisions at $\sqrt{s} = 1.8$ TeV*, Phys. Rev. Lett. **75** 3618–3623(1995) , `arXiv, hep-ex/9507002`.

[93] H. L. Lai et al., *Global QCD analysis and the CTEQ parton distributions*, Phys. Rev. **D51** 4763–4782(1995) , `arXiv, hep-ph/9410404`.

[94] Y. Coadou, Pa. Malecki and E. Richter-Was, *Prospects for physics measurements with the $W \to \tau\nu$ process for 100 pb^{-1} with the ATLAS detector*, ATL-PHYS-INT-2009-023.

[95] G. Nunes Hanninger et al., *Prospects for Studying $W \to \tau\nu$ Decays with ATLAS Data Corresponding to an Integrated Luminosity of 100 pb^{-1}*, ATL-PHYS-INT-2010-073.

[96] ATLAS Collaboration, *Performance of the ATLAS tau trigger in $p-p$ collisions at $\sqrt{s} = 7$ TeV*, ATLAS-CONF-2010-090.

[97] ATLAS Collaboration, *Performance of the ATLAS tau trigger in p-p collisions at $\sqrt{s}$=900 GeV*, ATLAS-CONF-2010-021.

[98] ATLAS Collaboration, *The ATLAS missing E_T trigger performance with initial LHC runs at $\sqrt{s} = 900\,\mathrm{GeV}$*, ATLAS-CONF-2010-026.

[99] ATLAS Collaboration, *Evidence for prompt photon production in $p-p$ collisions at $\sqrt{s} = 7\,\mathrm{TeV}$ with the ATLAS detector*, ATLAS-CONF-2010-077.

[100] G. Gaycken. Private communication.

[101] The W/Z signature group, *Supporting Document: Total inclusive W and Z boson cross-section measurements and cross-section ratios in the electron and muon decay channels at $\sqrt{s}$=7 TeV*, Tech. Rep. ATL-COM-PHYS-2010-703, CERN, Geneva, Sep, 2010.

[102] ATLAS Collaboration, *ATLAS Calorimeter Response to Single Isolated Hadrons and Estimation of the Calorimeter Jet Scale Uncertainty*, Tech. Rep. ATL-COM-PHYS-2010-367, CERN, Geneva, Jul, 2010.

[103] ATLAS Collaboration, *In-situ pseudo-rapidity inter-calibration to evaluate jet energy scale uncertainty and calorimeter performance in the forward region*, Tech. Rep. ATL-COM-PHYS-2010-370, CERN, Geneva, Jul, 2010.

[104] ATLAS Collaboration, *ATLAS Calorimeter Response to Single Isolated Hadrons and Estimation of the Calorimeter Jet Scale Uncertainty*, ATLAS-CONF-2010-052.

[105] J. Kraus. Private communication.

[106] CDF Collaboration, A. Safonov, *Physics with taus at CDF*, Nucl. Phys. Proc. Suppl. **144** 323–332(2005) .

[107] CDF and D0 Collaboration, S. Protopopescu, *$W \to \nu_\tau$ at the Tevatron*, Nucl. Phys. Proc. Suppl. **76** 91–97(1999) .

[108] D0 Collaboration, B. Abbott et al., *A Measurement of the $W \to \tau\nu$ production cross-section in p anti-p collisions at S**(1/2) = 1.8-TeV*, Phys.Rev.Lett. **84** 5710–5715(2000) , `arXiv, hep-ex/9912065 [hep-ex]`.

[109] CDF Collaboration, F. Abe et al., *Measurement of the Lepton Charge Asymmetry in W-Boson Decays Produced in $p\bar{p}$ Collisions*, Phys. Rev. Lett. **81** 5754–5759(1998) no. 26, .

[110] H.-L. Lai et al., *New parton distributions for collider physics*, Phys. Rev. **D82** 074024(2010) , `arXiv, 1007.2241 [hep-ph]`.

[111] J. Pumplin et al., *New generation of parton distributions with uncertainties from global QCD analysis*, JHEP **07** 012(2002) , `arXiv, hep-ph/0201195`.

[112] G. Cavalli et al., *First observation of $Z \to \tau_h \tau_\ell$ Decays with the ATLAS detector*, ATLAS-COM-CONF-2010-114.

Acknowledgements

It is a pleasure for me to acknowledge the contributions of so many people to this thesis. From my family and from my teachers at the many schools I've studied in Brazil, where I learned to pursue interests along many lines simultaneously, to my professors and supervisors.

First of all, I would like to thank my supervisor Prof. Dr. Norbert Wermes, who followed me during my M.Sc. studies and now during my Ph.D. studies. I thank him for guiding me through my studies and for the encouragement and advices he has provided me throughout this time as his student.

I also owe much gratitude to Jürgen Kroseberg, my second supervisor, for being able to work alongside him in the last three years and benefiting from his precise comments and for his infinite patience with me. I would like to thank him for his great support during all these studies. Finally, but not least, also for his proof-reading and corrections to the many drafts of this thesis, in particular for reading the early chapters, noting stylistic infelicities and spotting the big and still only partly developed themes.

I owe an equal debt to many scientists friends and colleagues, who patiently explained me the subtleties of their subjects or collaborated with my work. Earlier versions of most of the chapters appeared as internal or public ATLAS documents.

During the preparation for the first collisions at the LHC, several colleagues helped me preparing the studies needed for the observation of $W \to \tau\nu$ decays. Starting with Pawel Malecki, I profited a lot from his coding used in even former $W \to \tau\nu$ studies. Also thanks to Yann Coadou and Jochen Dingfelder for the great discussions and recommendations to improve the analysis and the quality of our internal note.

When the LHC started colliding protons, the work to analyze them was very intensive for several months. With the great help of Lidia Dell'Asta, Attilio Andreazza and Zofia Czyczula, we spent the summer holed up in our offices on the search for the first τ leptons in ATLAS. We were spread around the world, but faithful virtual companions and in constant contact all day (and some nights!) cross-checking numbers and keeping up with each others' progress. Also the contribution from Yann, Jochen, Jürgen and Jana Kraus were vital for those studies. With these friends and colleagues, I shared the pleasure and excitement of exploring the ideas presented here and to observe the first τ leptons from W decays in ATLAS. Indeed, CERN, in

Geneva–Switzerland, is a unique institution where the term “collaboration work” has genuine meaning in both theory and practice.

All the other members of the Bonn ATLAS group deserve recognition. During the last four years, many members have left while others joined in. I am tremendously grateful to all of them. In particular, special thanks go to Martin Schmitz, my generous friend and colleague, for the inspiring conversations, the great deal of help, advice, and support. To Duc Bao Ta for his enthusiasm and endless patience on helping me with coding or computer problems. I also warmly thank Dennis Hellmich, Götz Gaycken, Klemens Müller, Serena Psoroulas, Tan Wang and Tatevik Poghosyan for making the office (that we shared at different times) an interesting, lively and enjoyable place to work. To Agnieszka Leyko, Eckhard von Törne, Gia Khoriauli, Jan Schumacher, Jan Therhaag, Jörn Grosse-Knetter, Marc-André Pleier, Marc Lehmacher, Markus Cristinziani, Nicolas Möser, Thomas Schwindt for sharing their considerable experience in many useful discussions over the past years. I will miss our good wines in our *Sonderseminar* and our evening meetings organized by the Bonn-Wine-Tasting-Graduate-School committee. Also would like to thank Christoph Geich-Gimbel for his help many times I needed.

This thesis is the outgrowth of much study, travel and reflection over the last few years, but it is also the product of perseverance and hard work. It was written wherever I could find quietude, including even long transcontinental flights. I am specially indebted to those who took the time to read drafts, saving me from errors and steering me in new directions. I asked a few friends – Agnieszka Leyko, Martin Schmitz and Jana Kraus – to read parts of the manuscript and am greatly indebted to them for their extremely useful comments. When the text was almost complete, I asked Jochen for a critical reading on the introduction and conclusion chapters. His always generous support and incisive comments have been invaluable.

I acknowledge with gratitude the big debts that I owe to many friends who have helped make the last four years in Bonn so enjoyable and rewarding. In particular, special thanks go to Jana Jazic, Jaqueline Meireles, Julia Esswein, Martin Paus, Merlin Otte, Sandra Lerchen, Sylvie Dugay, and Thomas Egnal. Friends were indispensable. My debt to them is enormous.

To my family – all of my family, near and far – I thank you for tolerating me and my writing when I should have been relaxing with you, enjoying the summer in Brazil. Tio Edu e tia Teca, muito obrigado por tudo! Isso aqui é resultado do apoio de vocês! Oma, a senhora também tem sua participação aqui e eu agradeço de todo o meu coração!

This thesis is dedicated to my parents and siblings: their love and support have been an inestimable gift. I am forever grateful to them. Pai, Mãe, Gustavo e Bárbara, muito obrigado!